Study of Laminar Electrohydrodynamic Flows

Yifei Guan

A dissertation

submitted in partial fulfillment of the

requirements for the degree of

Doctor of Philosophy

University of Washington

2019

Reading Committee:

Igor Novosselov, Chair

Alberto Aliseda

James Riley

Program Authorized to Offer Degree:

Mechanical Engineering

University of Washington

Abstract

Study of Laminar Electrohydrodynamic Flows

Yifei Guan

Chair of the Supervisory Committee:
Research Assistant Professor Igor Novosselov
Department of Mechanical Engineering

From a physical perspective, electrohydrodynamic (EHD) flow is driven by collisions of neutral molecules with charged species accelerated by an electric field. In modeling, however, this effect can be simplified as a three-way coupling between the Navier-Stokes equations, the charge transport advection-diffusion equation, and Maxwell's equations. In the context of an electrohydrodynamic flow, this flow acceleration can be used for propulsion, species transport, and shear flow modification. Here, these applications are investigated numerically using several modeling approaches, including the finite volume method, Lattice Boltzmann method, and finite difference method, respectively. Finite volume method is used to model corona discharge phenomenon enabling a direct simulation corona-driven flow. Lattice Boltzmann method is used to model 2D and 3D electroconvection; the numerical code is parallelized and used for GPU computing. Finite difference method adapts a direct Poisson solver, which accelerates the convergence, it is used to model EHD flow in the laminar boundary layer.

TABLE OF CONTENTS

LIST OF FIGURES

LIST OF TABLES

ACKNOWLEDGEMENTS

Firstly, I would like to express my sincere gratitude to my advisor Prof. Igor Novosselov, for the continuous support of my Ph.D. research, for his patience, motivation, and immense knowledge. His guidance helped me in all aspects of research and writings. This dissertation would not be possible without his help.

Besides my advisor, I would like to thank Prof. Alberto Aliseda, Prof. James Riley, and Prof. Steve Brunton for their insightful comments and encouragement. I would also like to thank Prof. Christopher Bretherton for his time and support as my graduate school representative.

I appreciate the help from my fellow lab mates, especially Mr. Ravi Vaddi, who was in charge of most of the experimental work. Additionally, I thank Prof. Jian Wu from Harbin Institute of Technology for the informative discussions.

I appreciate the support by the DHS Science and Technology Directorate, the UK Home Office, Paul Allen Foundation, and the National Institutes of Health.

Last but not least, I would like to thank my parents, my grandparents, and my parents-in-law. I could not imagine how much they miss me back in China. I owe the accomplishment to my beloved wife, Ms. Yujie Xiong, who suffered but maintained a long-distance relationship with me. Without her encouragement and accompany, my life will never be the same.

Chapter 1. INTRODUCTION

Electrohydrodynamic (EHD) flow is an interdisciplinary science describing the interaction of fluids with electric fields. Positive ions are injected into a dielectric fluid in a strong electric field between two electrodes; the high-velocity ions transfer their kinetic energy to the neutral molecules by collisions that accelerate the flow in the direction of ion drift. This EHD flow propulsion phenomenon is used in many practical applications, such as convective cooling [1-6], electrostatic precipitators (ESP) [7-10], plasma assisted combustion [11], airflow control [12,13], and as a turbulent boundary layer actuators [14]. In this work, we study the EHD flow in the context of atmospheric positive corona discharge, laminar boundary layer, and the hydrodynamic instability of EHD convection (EC). In Chapter 2, we developed an analytical model for the EHD using a point-to-ring corona discharge, which is followed by Chapter 3, a numerical model based on a finite volume method investigating the same phenomenon. In Chapter 4, we derive a non-dimensional parameter *X,* which is defined as the ratio of electric force to viscous force. In Chapter 5, we study the energy transfer efficiency in an EHD propulsion device. Chapter 6 shows the EHD effects on laminar boundary layer with the numerical result from a finite difference model. Then we switch gear in Chapter 7 to study the laminar EC with and without a cross-flow. The conclusions are presented in 1.1, which is followed by Appendices.

1.1 EHD FLOW INDUCED BY ATMOSPHERIC CORONA DISCHARGE

Atmospheric corona discharge generates a flow of ions due of a strong electric field between an anode and a cathode; the high-velocity ions collide to the neutral air molecules and transfer their kinetic energy that accelerates the air in the direction of the ionic drift. When a high voltage is applied, the neutral air molecules are broken down by the strong electric field near the corona electrode. In a positive corona, the electrons are attracted to the anode; positive ions, such as O_2^+ and O^+ [15-17], drift to the cathode, which generates ionic wind. A quadratic voltage-current $(\varphi - I)$ relation was described by Townsend and validated for a coaxial corona discharge configuration [18,19]. Other corona discharge configurations also follow a quadratic relation with modifications due to specific parameters in the configuration, e.g., point-to-pot [15], point-to-plate [20], point-to-grid [21], sphere-to-plane [22], coaxial cylinders [23,24], wire-cylinder-plate [25], point-to-ring

[26-28], parallel electrodes [29], multi-electrodes [30], and nonuniform electric fields [31]. Guan et al. [32] developed an analytical model generalizing the $(\varphi - I)$ relationship independent of the corona configuration, which parameterizes one-dimensional flow in the direction of the electric field gradient. The ions' acceleration in the electric field and their interaction with the neutral molecules in the ion drift region can be modeled as an external force term (Coulomb force) in the Navier-Stokes equations (NSE). A two-part model is required: (i) the description of the ion motion in the electric field, and (ii) the effect of the ion drift on the neutral gas in the flow acceleration region.

1.1.1 *Analytical model*

The voltage-current $(\varphi - I)$ relation during the corona discharge characterizes the ion motion between the electrodes globally. This phenomenon has been studied since the early 20th century. The classic $(\varphi - I)$ relationship was derived by Townsend [18] in 1914 and validated for a coaxial corona configuration. The quadratic relationship has been validated for various corona geometries, such as point-to-pot [33], point-to-plate [20], and point-to-ring [26]. In a point-to ring corona, Giubbilini also demonstrated that the ion current is inversely proportional to the point-to-ring distance [26].

Some recent studies modify Townsend's quadratic relationship to better describe the $(\varphi - I)$ relationship for different electrode configurations, e.g., point-to-plate [34,35], point-to-grid [21], point-to-cylinder[36], sphere-to-plane [22], coaxial cylinders [23,24], wire-cylinder-plate [25,37,38], point-to-ring [26-28], parallel electrodes [29], multi-electrodes [30], and non-uniform electric fields [31]. In propulsion studies, the electrostatic force has been modeled using various hydrodynamic terms, such as body forces [39] or pressure (drag) [7]. Typically, the ionic wind velocity is experimentally described as a function of the corona anode voltage [28,40-42]. Previous experimental study of point-to-ring geometry investigated external EHD flow [28]; the internal EHD flow can provide more consistent measurement and achieve higher velocities due to more efficient axial flow acceleration.

In Chapter 2, we develop an analytical model for corona-driven EHD flow in an axisymmetric geometry and validate the model against the experimental measurements in atmospheric conditions. The conceptual representation of the EHD system includes (i) gas ionization region, (ii) flow acceleration region where unipolar ion motion in the gas medium acts as a body force accelerating the flow, and (iii) momentum conservation region dominated by the inertial and

viscous terms of the NSE. These regions do not necessarily have clear boundaries; however, they can be characterized based on the flow non-dimensional parameters dominant in each of them. The model presented in this chapter addresses the flow acceleration behavior resulting from ion collisions with neutral air molecules in the ion drift region. During the development, we first obtain the relationship between the electric properties of the EHD flow, such as corona voltage φ, electric field $\mathbf{E}$, and charge density ρ_c for planar, cylindrical, and spherical coordinates. Then, the EHD velocity profiles are solved numerically using a Chebyshev spectral method. Finally, the analytical model is compared with the experimental data for a point-to-ring corona in an internal pipe flow configuration. The model results are compared with the experimental data in the acceleration region but overpredict the velocity in the regions away from the axis of the domain. In the inertial flow region (away from the centerline), the flow develops under the balance between the EHD force, convective flow acceleration, and viscous shear stresses.

1.1.2 *Numerical model*

A better understanding of the multiphysics nature of the EHD flow requires the insight of the phenomenon. To correctly predict the flow established by the electric force, the following elements need to be considered: (1) the electric field resulting from the potential difference between the corona and ground electrodes, as well as its modifications due to the space charge in the high ion concentration in the region; (2) the ion motion in the resulting electric field; (3) the interaction between the ion drift and the neutral gas in the flow acceleration region; (4) the viscous and turbulent stresses; and (5) the effects of developing complex flow patterns as a result of the accelerating flow and device geometry. The results of the analytical model can be improved in the numerical simulation to describe all EHD flow regions: (1) the application of the EHD force in the axial direction neglects the effect of the three-dimensional nature of the electric field (the formation of complex flow patterns can be described by the numerical model); and (2) in order to capture the pipe flow, an inertial flow region needs to be modeled.

To gain insight into the developing EHD flow, an approach is formulated and implemented in a computational fluid dynamics (CFD) simulation that solves for the coupled flow and electric fields in the presence of corona discharge. State-of-the-art literature evaluates several corona configurations [43-45]. Numerical modeling has been applied to the design and analysis of

electrostatic precipitators (ESP) [46-49] and heat transfer enhancement [2,4,5,50,51]. Previous EHD flow models use an iterative approach to (1) calculate the electric field and electric force under Kaptzov's hypothesis [52] or Peek's law [53], and (2) set a constant space charge on the anode so that the solution matches the cathode current from the experimental data. This method requires multiple iterations and is therefore inefficient.

In contrast, our modeling approach solves for charge density by introducing a volumetric charge flux derived from the anode current directly, as shown in Chapter 3. The charge flux is imposed on a "numerical ionization region" determined by the electric field and the thresholds for the onset of ionization. The ionization (charge flux) and spatial charge density are two-way coupled to the NSE solver, avoiding the iterative procedure for solving the electric field. The electric force acts on a volume of fluid, inducing the EHD flow; this ion - bulk flow coupling is similar to previous work [2,4,5,43-51].

Chapter 3 is followed by two short chapters in which we performed dimensional analysis and energy transfer analysis. In Chapter 4, we proposed a non-dimensional parameter *X,* which denotes the ratio of electric force to viscous force. It may replace the electric-inertia number N_{EI} in non-equilibrium EHD where charge density is non-uniform in the flow. Later in Chapter 5, we formulate the propulsion energy conversion efficiency as a ratio of fluids kinetic power versus electric input power. By integrating the outlet velocity profile obtained from CFD and experiments, we show that the energy transfer efficiency is a nonlinear function of corona voltage, and for the specific point-to-ring corona setup, the transfer efficiency is generally lower than 1%.

1.2 EHD BOUNDARY LAYER FLOW

Plasma actuators have been used in boundary layer control [14,54-61]. A corona discharge near the wall can be used to modify the airflow in the boundary layer, to reduce drag, and to control separation on airfoils at higher angles of attack. Velkoff et al. [62] have studied the effect of corona discharge on the laminar to turbulent transition point on a flat plate. The transition point shifted by 43 mm for an external free stream velocity of 53 m/s. Several researchers studied drag reduction using corona discharge on a flat plate [63,64]. Roth et al.[65] used smoke wire flow visualization to show that the primary cause of the EHD effect is a combination of mass transport and vortex structures

induced by strong paraelectric electric forces on the flow. Moreau and Léger [66,67] studied corona discharge on an inclined flat plate at low velocity and have observed a reduction in drag. A maximum velocity of 2.75 m/s for 500 μA current and the effect of an external free stream on boundary layer profile and pressure distribution has been studied experimentally [66]. Moreau et al.[68] further investigated the effect of EHD on a turbulent boundary layer over a flat plate for velocity up to 25m/s.

In Chapter 6, we investigate the EHD effect on a laminar boundary layer using a finite difference method based on the pressure projection method. First, the numerical approach is validated against the analytical solution (Blasius profile [69-71]) without charge injection. Then the simulations are performed with added EHD flow, the introduction of an electric field and charge injection results in a ~10% increase of velocity within the viscous boundary layer.

1.3 HYDRODYNAMIC INSTABILITY OF ELECTROCONVECTION

As a subset of EHD, electroconvection (EC) is a phenomenon where convective transport is induced by unipolar discharge into a dielectric fluid [43,72-90]. Both 2D and 3D vortex structures have been observed in fluid systems. In considering convection, flow patterns result from a body force acting on the fluid, e.g., Rayleigh-Benard convection (RBC) [90-96], Marangoni effects [97-101], magneto-convection [102-110], and magnetohydrodynamics convection [111-118]. The transition from 3D to 2D structures under the influence of shear stress has been observed in the formation of atmospheric cloud streets in planetary boundary layers [119-121], and in laboratory RBC studies [122-126]. In electro-convection (EC) phenomena, the convective transport is induced by unipolar discharge in a dielectric fluid [43,72-90], and though the forcing term is different from the other systems, both 3D and 2D patterns can exist; these are determined by the balance of forces acting on the fluid.

The EC stability problem was first analyzed by a reduced non-linear hydraulic model [127,128], and by a linear stability analysis without the charge diffusion term [129,130]. Atten & Moreau [131] showed that, in the weak-injection limit, C<<1, the flow stability is determined by the parameter $T_c C^2$, where C is the charge injection level and T_c is the linear stability threshold for the electric

Rayleigh number T, a ratio between electric force to the viscous force (Eq. (86)). In the space-charge-limited (SCL) injection ($C \to \infty$), the flow stability depends on T_c alone [132-134]. The effect of charge diffusion was investigated by Zhang et al. by employing linear stability analysis on the EC problem with a Poiseuille flow [81], and by non-linear analysis using a multiscale method [86]. The authors found that the charge diffusion has a non-negligible effect on T_c, and the transient behavior depends on the Reynolds number (Re) [81,86]. Li et al. performed linear analysis to study convective instabilities in Electro-hydrodynamical-Poiseuille flow and found that the ratio of the Coulomb force to the viscous force has an impact on the transition of transverse rolls from convective to absolute instability [135].

Though the 3D EC stability problem in the presence of shear is complicated, it is somewhat analogous to Rayleigh-Bernard convection (RBC) [122-126,136-139]. For example, in cross-flow, the suppression of the transverse cells, and the evolution of the longitudinal cells has been reported. And in the meteorological application, the addition of cross-flow leads to the formation of cloud streets [119]. Mohamad et al. used a non-dimensional group Gr / Re^2, the ratio of buoyancy to the inertia force, to parametrize the effect of applied shear, where Gr is the Grashof number [126]. For $Gr / Re^2 > 10$, the impact of the cross-flow is insignificant, while for $Gr / Re^2 < 0.1$, the effect of the buoyancy can be neglected. Reduced nonlinear models such as Ginzburg-Landau equations are used to study the transitional behavior of RBC cells [122-125].

Numerical modeling can be used to g insight into the behavior of EC vortices. Early work has shown that infinite difference modeling, strong numerical diffusivity can lead to an incorrect prediction of stability criteria [73]. Several other numerical approaches have been developed, including the particle-in-cell method [140], the finite-volume method with flux-corrected transport [141] or the total variation diminishing scheme [74,77,83-85], and the method of characteristics [43]. Luo et al. showed that a unified Lattice Boltzmann model (LBM) predicts the linear and finite amplitude stability criteria of the subcritical bifurcation in the EC flow for both 2D and 3D flow scenarios [87-90]. This unified LBM transforms the elliptic Poisson equation into a parabolic reaction-diffusion equation and introduces artificial coefficients to control the evolution of the electric potential. A segregated solver was proposed that combines a two-relaxation time (TRT) LBM modeling of the

fluid and charge transport, and a Fast Fourier Transform Poisson solver for the electric field [142]. Related to vortex structure transition with the addition of cross-flow, 2D finite-volume simulations of Poiseuille flow have demonstrated that the value of T_c is a function of Re and the ion mobility parameter, M [82]. More recently, 2D numerical simulations have been used to parameterize the flow transition from stable EC vortex pairs to the base cross-flow scenario [143].

In the context of EC, for a large electric Rayleigh number (T) the system can transform from a steady EC convection into a chaotic state before the flow develops into turbulence. The chaotic theory was first introduced by Lorenz [144] with a reduced model by retaining the first few Fourier modes of the convection model proposed by Saltzman [145,146]. The chaotic EC sees applications in enhancing heat and mass transfer [83,147-153], mixing in microfluidics [154-157], pattern selection in spatially extended systems [158], and random number generator [159]. The chaotic EC phenomenon was first observed and analyzed by Atten and colleagues [72,160]. They characterized two types of behaviors of the power spectra of the intensity fluctuations accounting for two scenarios: dominating viscous force or inertia. Later Perez and Castellanos discovered that chaotic mixing of charges occurs even with low Reynolds number and therefore the laminar chaotic mixing is the origin of EC chaos and hydrodynamic turbulence [161]. Since then, many researchers have investigated the chaotic EC experimentally in nematic liquid crystal [162-168]. To quantify the chaotic EC, Castellanos and Perez showed that the maximal Lyapunov exponents are linearly dependent on the average velocity amplitude [169]. Tsai and colleagues proposed a local-power-law scaling theory of electric Nusselt number (*Ne*) with respect to electric Rayleigh number T [164,165]. More recently, researchers showed that the electro-osmosis effect in micro-devices also contributes to the EC chaos [78,170-172]. In 1.1, we show the transition of EC vortices from a steady state to the aperiodic chaotic state. The threshold value of T is obtained by numerical simulation. The onset of chaos is marked by an irregular and aperiodic fluctuation of the electric Nusselt number *Ne*.

Chapter 2. ANALYTICAL MODELS FOR EHD FLOW

In this chapter, we develop an analytical model for corona-driven EHD flow and validate the model against the experimental measurements in air. The conceptual representation of the EHD system includes (i) gas ionization region, (ii) flow acceleration region where unipolar ion motion in the

gas medium acts as a body force accelerating the flow, and (iii) momentum conservation region dominated by the inertial and viscous terms of the NSE. These regions do not necessarily have clear boundaries; however, they can be characterized based on the flow non-dimensional parameters dominant in each of them. The model presented in this chapter addresses the flow acceleration behavior resulting from ion collisions with neutral air molecules in the ion drift region. During the development, we first obtain the relationship between the electric properties of the EHD flow, such as corona voltage φ, electric field $\mathbf{E}$, and charge density ρ_c for planar, cylindrical, and spherical coordinates. Then, the EHD velocity profiles are solved numerically using a Chebyshev spectral method. Finally, the analytical model is compared with the experimental data for a point-to-ring corona in an internal pipe flow configuration.

2.1 MODEL DEVELOPMENT

The analytical expression for $(\varphi - I)$ and $(\varphi - u)$ relationships are derived for the steady-state conditions in the planar, cylindrical, and spherical coordinates.

2.1.1 *Voltage-Current relationship*

The density ρ_k of the charged species k follows the conservation equation[36-38,173]

$$\frac{\partial \rho_k}{\partial t} + \nabla \bullet \left[\left(\mathbf{u} + \mu_{bk} \mathbf{E} \right) \rho_k - D_k \nabla \rho_k \right] = \omega_k , \tag{1}$$

where $\mathbf{u}$ is the velocity vector of the bulk flow, $\mathbf{E}$ is the electric field vector, μ_{bk} and D_k are mobility and diffusivity of each charged species k, ω_k is the production rate of species k. The ionization is often conceptualized as two processes: (i) ionization process where ion species are generated and (ii) reattachment processes where charges recombine. Multiple analytical and numerical models for production rate ω_k have been presented in the literature; the rate is often modeled as a function of species density, mobility with derived ionization and recombination coefficients [35,36,38,173].

In the context of the EHD flow model development, two observations on the ionization region are important. First, the ionization process is assumed to occur only in the region where the electric

field strength is greater than a threshold value $E_i \approx 3\times10^6\, V/m$ [20,174]. Thus the ionization is limited to a small region near the anode. The ionization region length scale - b can be approximated by $\frac{\varphi_0}{E_i}$, where φ_0 is the anode voltage [173,175]. Second, the positive and negative species within the ionization zone travel in opposite directions: positive ions move towards cathode; negative ions and electrons -- towards the anode. The total momentum exerted on the gas neutral molecules within the ionization region is negligible compared to that in the unipolar drift region; thus the detailed description of the ionization region is not necessary for this model to work, as long as bulk properties related to energy transfer can be obtained. To relate the electric power to the kinetic energy in the flow, the source term needs to be evaluated. In this work, we estimate the energy input based on the experimental measurements of the corona current. We assume that flow acceleration takes place in the acceleration region only within the ion drift region where the net charge density $\rho_c = \sum_k \rho_k$ participates in electric to kinetic energy conversion through ion/neutral molecule collisions.

The continuity equation for the charge density in the drift region is

$$\frac{\partial \rho_c}{\partial t} + \nabla\bullet\left[\left(\mathbf{u} + \mu_b \mathbf{E}\right)\rho_c - D_c \nabla \rho_c\right] = 0\,, \tag{2}$$

where ρ_c is the charge density, $\mathbf{u}$ is the velocity vector of the bulk flow, $\mathbf{E}$ is the electric field vector, μ_b is the ion mobility, which is approximated as a constant ($2.0e-4 m^2/V-s$) at atmospheric pressure and room temperature (300K) [5,9,32,50,176], (this constant is likely to have different values for negative corona or corona in other gases) and D_c is the ion diffusivity, described by the electric mobility equation

$$D_c = \frac{\mu_b k_B T}{q}\,, \tag{3}$$

where k_B is Boltzmann's constant, T is the absolute temperature, and q is the electric charge of an ion, which is equal to the elementary charge in this case.

The electric field satisfies Maxwell's equation

$$\nabla \bullet \mathbf{E} = \frac{\rho_c}{\varepsilon}, \tag{4}$$

where ε is the air permittivity close to the permittivity of free space.

Since the ion drift velocity is considerably greater than the velocity of the resulting EHD flow, the ion motion equation can be assumed to be quasi-steady

$$\nabla \bullet \left[\left(\mathbf{u} + \mu_b \mathbf{E} \right) \rho_c - D_c \nabla \rho_c \right] = 0 . \tag{5}$$

To estimate the effect of the charge diffusion, consider the Sherwood number for ionic transport in the presence of strong external electric field:

$$Sh = \frac{\mathbf{u} + \mu_b \mathbf{E}}{\left(\frac{D_e}{L_\mathrm{d}} \right)} \approx \frac{|\mathbf{E}| Lq}{k_B T} \sim O\left(10^4\right), \tag{6}$$

where L_d is the diffusion length scale. The diffusion term can be neglected, further reducing the charge continuity equation to

$$\nabla \bullet \left[\left(\mathbf{u} + \mu_b \mathbf{E} \right) \rho_c \right] = 0, \tag{7}$$

and since $\frac{|\mathbf{u}|}{|\mu_b \mathbf{E}|} = \frac{O(1)}{O(100)} = O\left(10^{-2}\right)$ in air discharge [2,5,9,174], the continuity equation for ions is reduced to

$$\nabla \bullet \left[\mu_b \rho_c \mathbf{E} \right] = 0, \tag{8}$$

where $\mu_b \rho_c \mathbf{E} = \mathbf{J}$; $\mathbf{J}$ is the current flux $\left[Amperes / m^2 \right]$. Combining with Eq. (4), the ion transport equation can be written as

$$\frac{\mu_b}{\varepsilon} \rho_c^2 - \mu_b \nabla \varphi \nabla \rho_c = 0 . \tag{9}$$

Note that Eq. (9) is the same as Eq. (5) in Sigmond [20] if ρ_c is substituted by $-\varepsilon \nabla^2 \varphi$.

Eq. (9) can be solved in Cartesian coordinates:

Dividing μ_b into both sides and rearranging gives

$$\nabla \varphi = \frac{\rho_c^2}{\varepsilon \nabla \rho_c} \tag{10}$$

In one dimension, we have

$$\frac{d}{dr}\varphi = \frac{\rho_c^2}{\varepsilon \frac{d\rho_c}{dr}} \quad . \tag{11}$$

Take the r-derivative on both sides and apply Maxwell's equation

$$\frac{d^2\varphi}{dr^2} = -\frac{\rho_c}{\varepsilon} = \frac{2\rho_c \frac{d\rho_c}{dr}\left(\varepsilon \frac{d\rho_c}{dr}\right) - \rho_c^2\left(\varepsilon \frac{d^2\rho_c}{dr^2}\right)}{\left(\varepsilon \frac{d\rho_c}{dr}\right)^2} \quad , \tag{12}$$

Rearranging the terms, we have

$$3\left(\frac{d\rho_c}{dr}\right)^2 = \rho_c\left(\frac{d^2\rho_c}{dr^2}\right) \quad . \tag{13}$$

One possible solution has the form

$$\rho_c = \rho_0 r^n \quad , \tag{14}$$

substituting into Eq. (13)

$$3n^2 r^{2(n-1)} = n\left(n-1\right) r^{2n-2} . \tag{15}$$

Therefore, $n = -1/2$ and $\rho_c = \rho_0 r^{-1/2}$.

Substituting to Eq. (4)

$$E = -\frac{d}{dr}\varphi = -\frac{\rho_c^2}{\left(\varepsilon \frac{d\rho_c}{dr}\right)} = \frac{2\rho_0}{\varepsilon} r^{1/2} , \tag{16}$$

$$d\varphi = -\frac{2\rho_0}{\varepsilon} r^{1/2} dr . \tag{17}$$

Integrating both sides gives

$$\varphi - \varphi_0 = -\frac{4\rho_0}{3\varepsilon} r^{3/2} . \tag{18}$$

Eq. (9) can also be solved in cylindrical coordinates:

Rewriting Eq. (10), we have

$$\nabla\varphi = \frac{\rho_c^2}{\varepsilon \nabla\rho_c} . \tag{19}$$

Taking the divergence of both sides and applying Maxwell's equation gives

$$\nabla^2\varphi = -\frac{\rho_c}{\varepsilon} = \nabla\bullet\left(\frac{\rho_c^2}{\varepsilon\nabla\rho_c}\right) = \frac{1}{r}\frac{d}{dr}\left(\frac{r\rho_c^2}{\varepsilon\frac{d\rho_c}{dr}}\right) = \frac{1}{r}\frac{\left(2r\rho_c\frac{d\rho_c}{dr} + \rho_c^2\right)\left(\varepsilon\frac{d\rho_c}{dr}\right) - r\rho_c^2\left(\varepsilon\frac{d^2\rho_c}{dr^2}\right)}{\left(\varepsilon\frac{d\rho_c}{dr}\right)^2} \tag{20}$$

By rearranging the terms, we have

$$r\rho_c\left(\frac{d^2\rho_c}{dr^2}\right) = r\left(\frac{d\rho_c}{dr}\right)^2 + \left(2r\frac{d\rho_c}{dr} + \rho_c\right)\left(\frac{d\rho_c}{dr}\right) . \tag{21}$$

Assume solution in the form

$$\rho_c = \rho_0 r^n \tag{22}$$

and substituting it into Eq. (21) provides

$$n(n-1)r^{2n-1} = n^2 r^{2n-1} + \left(2nr^n + r^n\right) nr^{n-1} \tag{23}$$

$$n(n-1) = n^2 + (2n+1)n\,. \tag{24}$$

Therefore, $n = -1$, and from Eq. (22), $\rho_c = \rho_0 r^{-1}$. From Eq. (4)

$$E = -\frac{d}{dr}\varphi = -\frac{\rho_c^2}{\left(\varepsilon \dfrac{d\rho_c}{dr}\right)} = \frac{\rho_0}{\varepsilon} \tag{25}$$

$$d\varphi = -\frac{\rho_0}{\varepsilon} dr\,. \tag{26}$$

Integrating on both sides gives

$$\varphi - \varphi_0 = -\frac{\rho_0}{\varepsilon} r\,. \tag{27}$$

Eq. (9) can also be solved in spherical coordinates:

Rewriting Eq. (10), we have

$$\nabla\varphi = \frac{\rho_c^2}{\varepsilon \nabla \rho_c} \tag{28}$$

Taking the divergence on both sides and applying Maxwell's equation (Eq. (4)) provides

$$\nabla^2\varphi = -\frac{\rho_c}{\varepsilon} = \nabla\bullet\left(\frac{\rho_c^2}{\varepsilon\nabla\rho_c}\right) = \frac{1}{r^2}\frac{d}{dr}\left(\frac{r^2\rho_c^2}{\varepsilon\dfrac{d\rho_c}{dr}}\right) = \frac{1}{r^2}\frac{\left(2r^2\rho_c\dfrac{d\rho_c}{dr}+2r\rho_c^2\right)\left(\varepsilon\dfrac{d\rho_c}{dr}\right)-r^2\rho_c^2\left(\varepsilon\dfrac{d^2\rho_c}{dr^2}\right)}{\left(\varepsilon\dfrac{d\rho_c}{dr}\right)^2} \quad . \tag{29}$$

Rearranging, we have

$$r\rho_c\left(\frac{d^2\rho_c}{dr^2}\right) = r\left(\frac{d\rho_c}{dr}\right)^2 + \left(2r\frac{d\rho_c}{dr}+2\rho_c\right)\left(\frac{d\rho_c}{dr}\right) \tag{30}$$

One possible solution has the form

$$\rho_c = \rho_0 r^n \tag{31}$$

And substituting it into Eq. (30) gives

$$n(n-1)r^{2n-1} = n^2r^{2n-1} + \left(2nr^n+2r^n\right)nr^{n-1} \tag{32}$$

$$n(n-1) = n^2 + (2n+2)n\,, \tag{33}$$

therefore, $n = -3/2$ and $\rho_c = \rho_0 r^{-3/2}$, the substitution into Eq. (4) gives

$$E = -\frac{d}{dr}\varphi = -\frac{\rho_c^2}{\left(\varepsilon\dfrac{d\rho_c}{dr}\right)} = \frac{2\rho_0}{3\varepsilon}r^{-1/2}\,, \tag{34}$$

$$d\varphi = -\frac{2\rho_0}{3\varepsilon}r^{-1/2}dr\,, \tag{35}$$

integrating both sides

$$\varphi - \varphi_0 = -\frac{4\rho_0}{3\varepsilon}r^{1/2}\,. \tag{36}$$

Table I shows the solutions for this nonlinear differential equation in different coordinates systems; r is the distance from the anode [mm].

Table I. Solutions for ion transport equation in one dimensional Cartesian, cylindrical coordinates, and spherical coordinates.

Variables	Planar coordinates	Cylindrical coordinates	Spherical coordinates
ρ_c	$\rho_c = \rho_0 r^{-1/2}$	$\rho_c = \rho_0 r^{-1}$	$\rho_c = \rho_0 r^{-3/2}$
$E = \lvert\mathbf{E}\rvert$	$E = \frac{2\rho_0}{\varepsilon} r^{1/2}$	$E = \frac{\rho_0}{\varepsilon}$	$E = \frac{2\rho_0}{3\varepsilon} r^{-1/2}$
φ	$\varphi_0 - \frac{4\rho_0}{3\varepsilon} r^{3/2}$	$\varphi_0 - \frac{\rho_0}{\varepsilon} r$	$\varphi_0 - \frac{4\rho_0}{3\varepsilon} r^{1/2}$
ρ_0	$\frac{C}{m^3}(mm^{1/2})$	$\frac{C}{m^3} mm$	$\frac{C}{m^3} mm^{3/2}$

Here, φ_0 is the anode voltage and ρ_0 is a dimensional parameter (which is not necessarily a constant and for the fixed ionization volume may vary with corona voltage see Eq. (42)); the units depend on the coordinate system. The integration constant only appears in the voltage φ since the Eq. (9) only depends on the gradient of φ. For a point-to-ring geometry, the ionization and drift regions are best approximated as spherical sectors with a radius r and angle β determined by the position of the corona needle, as shown in FIG. 1.

$$\cos\beta = \frac{L}{\sqrt{L^2 + R^2}}, \tag{37}$$

where L is the distance between the needle tip to the center of the cathode, and R is the radius of the cathode ring.

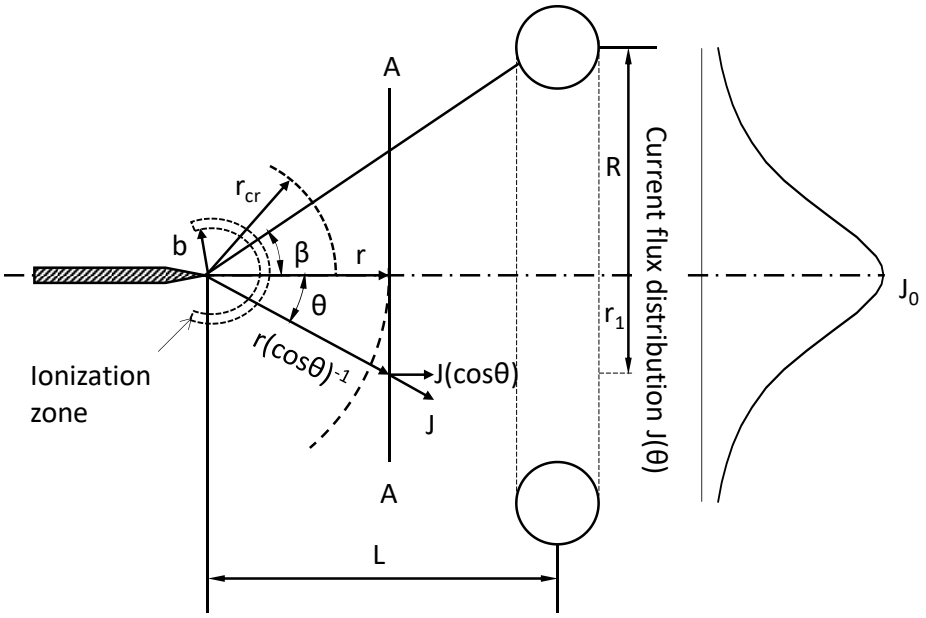

FIG. 1. Diagram of the point-to-ring corona system with current flux distribution.

The ion current flux magnitude between the needle and the ring is

$$J = |\mathbf{J}| = \mu_b \rho_c E = \frac{2\mu_b \rho_0^2}{3\varepsilon r^2} \ . \tag{38}$$

Eq. (38) shows that $J \propto r^{-2}$. The current flux distribution is given as

$$\frac{J}{J_o} = \left(\frac{r(\cos\theta)^{-1}}{r} \right)^{-2} = \cos^2\theta \,, \tag{39}$$

where J_o is the maximum current flux distribution, and θ is the solid angle of the discharge, $\theta \in [0, \beta]$. Considering the axial component of current flux, $\theta = 0$

$$J_a = J\cos\theta = J_o \cos^3\theta \,, \tag{40}$$

where J_a is the current flux in the axial direction.

To define the conditions in the acceleration region, consider r_{cr} as the characteristic length scale of the flow acceleration region, as the radius of a spherical surface with the electric potential equal to φ_{cr} (defined as the onset voltage of the corona, similar to the definition by Townsend [18]). The current flux on the critical surface is:

$$J_{cr} = \frac{2\mu_b \rho_0^2}{3\varepsilon r_{cr}^2} \quad . \tag{41}$$

In spherical coordinates for the point-to-ring geometry

$$\rho_0 = \frac{3\varepsilon}{4r_{cr}^{1/2}}\left(\varphi_0 - \varphi_{cr}\right). \tag{42}$$

Therefore,

$$J_{cr} = \frac{3\mu_b \varepsilon}{8r_{cr}^3}\left(\varphi_0 - \varphi_{cr}\right)^2. \tag{43}$$

Due to the conservation of current flux, the corona current can be found by integrating the current flux over the spherical dome

$$I = \int_{cr} J_{cr} dA = J_{cr} A_{cr} = \frac{3\pi\mu_b \varepsilon}{4r_{cr}}\left(1 - \frac{L}{\sqrt{L^2 + R^2}}\right)\left(\varphi_0 - \varphi_{cr}\right)^2. \tag{44}$$

Eq. (44) is similar to Townsend's quadratic relationship for the coaxial-cylinder electrode configuration $I = C_{cyl}\varphi_0\left(\varphi_0 - \varphi_c\right)$, where $C_{cyl} = \frac{8\pi\mu_b\varepsilon}{R^2 \ln\left(R/r\right)}$ is a geometrically dependent constant [18]. For cylindrical coordinates, replacing $E = \frac{\rho_0}{\varepsilon}$ by $E = \frac{\varphi_0}{R \ln R/r}$ and for $r_{cr} = R/4$, the $\varphi - I$ relation is identical to that of Townsend. The Eq. (44) is also similar to the one derived by Sigmond for a space-charge saturated point-to-plate corona discharge using time-dependent analysis [20], where $I = 2\mu_b \varepsilon \varphi^2 / L$. The $\varphi - I$ relationship derived in this work is more general than particular formulations presented in [18] and [20]. However, for a specific geometry, the values of φ_{cr} and the corresponding length scale, r_{cr}, need to be determined experimentally or additional assumptions need to be made. Once the $\varphi - I$ relationship is defined, the EHD velocity can be computed.

2.1.2 *Voltage-Velocity relationship*

The EHD flow induced by point-to-ring discharge can be divided into three regions: ionization zone, acceleration region, and momentum conservation region. The ionization region does not participate in the momentum exchange between the ions and neutral molecule significantly as the population of negative and positive species is balanced. The non-dimensional analysis shows that

the acceleration region can be defined by the high ion concentration and high electric field strength [174]. The momentum conservation region is the part of the domain where electric force is balanced or overcome by viscous forces near the walls. **FIG.** 2 illustrates the relative positions of the ionization zone, EHD acceleration region, and EHD momentum dissipation region.

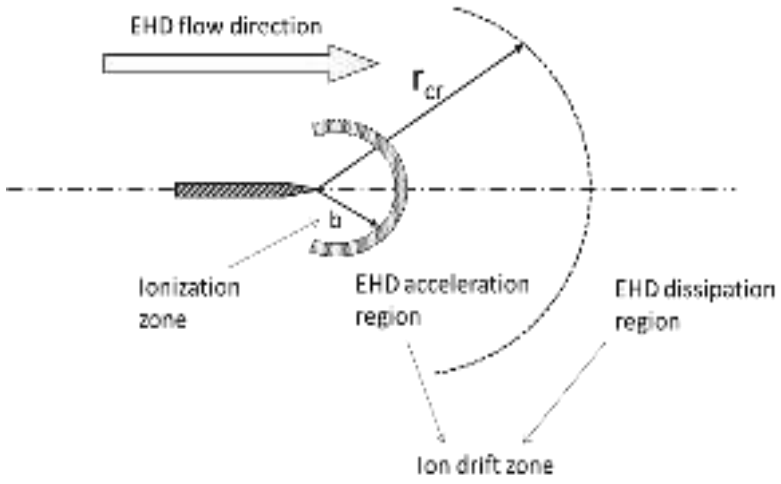

FIG. 2. Diagram of the relations among ionization zone, EHD acceleration region, and EHD dissipation region of a point-to-ring corona system.

The steady-state energy equation for a constant area pipe can be written as

$$SE_{inlet} = SE_{out} + SE_e \,, \tag{45}$$

where SE_e is the energy gained from the electric force, which can be written as

$$SE_e = \frac{\int \rho_c E dr}{\rho} = \frac{\int J dr}{\rho \mu_b} = \frac{3\varepsilon}{8\rho r_{cr}} \left(\varphi_0 - \varphi_{cr}\right)^2 \int_0^{r_c} r^{-2} dr \,, \tag{46}$$

where ρ is the mean density of the flow. Since both the inlet and outlet are at atmospheric pressure and the flow is in the direction of the electric field line, the velocity on the axis of the cylindrical pipe is

$$u_{\max} = \sqrt{2SE_e} = \left[\frac{3\varepsilon}{4\rho r_{cr}} \int_0^{r_{cr}} r^{-2} dr \right]^{1/2} \left(\varphi_0 - \varphi_{cr}\right) \,. \tag{47}$$

The force is acting only on the gas downstream of the ionization region; thus, the lower integration limit is set to the ionization zone boundary, *b*.

$$u_{\max} = \left[\frac{3\varepsilon}{4\rho r_{cr}} \int_{b}^{r_{cr}} r^{-2} dr \right]^{1/2} \left(\varphi_0 - \varphi_{cr} \right) \tag{48}$$

2.1.3 *Velocity profile*

The velocity profile in a cylindrical pipe for the point-to-ring configuration is obtained under the assumption that the electric force results only in axial flow acceleration. Viscous drag is balanced by the electric force on the ions. In cylindrical coordinates:

$$\mu \left(\frac{\partial^2 u_a}{\partial r^2} + \frac{1}{r} \frac{\partial u_a}{\partial r} \right) = -\rho_c E_a = -\frac{J_a}{\mu_b} \ , \tag{49}$$

$$\cos\theta = \frac{L}{\sqrt{L^2 + r^2}} \, , \tag{50}$$

where subscript a denotes the axial component of the vectors. Substituting Eq. (40) and Eq. (50) in Eq. (49) and rearranging the terms results in the following ODE

$$r \frac{\partial^2 u_a}{\partial r^2} + \frac{\partial u_a}{\partial r} = -\frac{J_0 L^3}{\mu \mu_b} \left[\frac{r}{\left(r^2 + L^2 \right)^{3/2}} \right]. \tag{51}$$

The ODE is solved numerically using Chebyshev polynomial approximation with the MATLAB package *chebfun* [177-180]. Neumann boundary condition (zero-flux) are used at the axis and the non-slip boundary condition (zero-velocity) at the wall. The Chebyshev differential matrices for first and second derivatives are constructed to satisfy the boundary conditions[179].

2.2 RESULT AND DISCUSSION

2.2.1 *Model Validation - Experimental setup*

The EHD flow is studied in a point-to-ring internal pipe geometry. shows the experimental setup. The apparatus consists of a high-voltage corona needle and a grounded ring electrode. The anode needle is a 0.5-mm-thick tungsten needle with a radius of curvature of 1 μm at the tip (measured using optical microscopy). The sharpness of the needle is important because it affects the corona discharge at lower voltages [181]. The tip of the needle is checked regularly for visible defects to ensure that it does not degrade over time. The ground electrode is a 1.58-mm-thick solid solder

with an inner radius of 10 mm. The enclosure is fabricated using 3D printing in the polylactic acid polymer. The distance between the anode and cathode (L) is set in the range of 3 to 7 mm using spacers. A variable high-voltage power supply (Bertan 205B-20R) is used to set the electric potential between the electrodes. The cathode current is measured on the cathode based on a voltage drop across a 1 MΩ resistor.

The EHD experiment is operated in the positive corona mode in a temperature range of 22-25 ^{0}C, relative humidity of 23-25%, and ambient pressure. For each anode-cathode distance, the voltage is increased from 4 kV (when the outlet velocity is measurable) to ~10 kV (when the arc discharge occurs). Constant current hot-wire anemometry is used to measure the flow velocity profile. A TSI 1213-20 probe connected to the anemometer (AA-1005) is positioned at the outlet of the device. The anemometer is calibrated for a range of velocities from 0.2 to 8 m/s [182]. The entire experimental setup is mounted on an optical table; the anemometer probe is attached to a 3D translation stage to obtain space-resolved measurements. The anemometer data are collected at a frequency of 10 kHz using data acquisition hardware (myRIO-1900) over a sampling time of 30 s. The ion concentration at the exit of the device is measured at a distance of 25.4 mm from the outlet using an air ion counter (Alpha Lab). The ion concentration measurements are not used in the analysis; rather, they provide an order of magnitude comparison between the experiments and simulations. Each experimental condition is tested at least five times to obtain independent statistical samples.

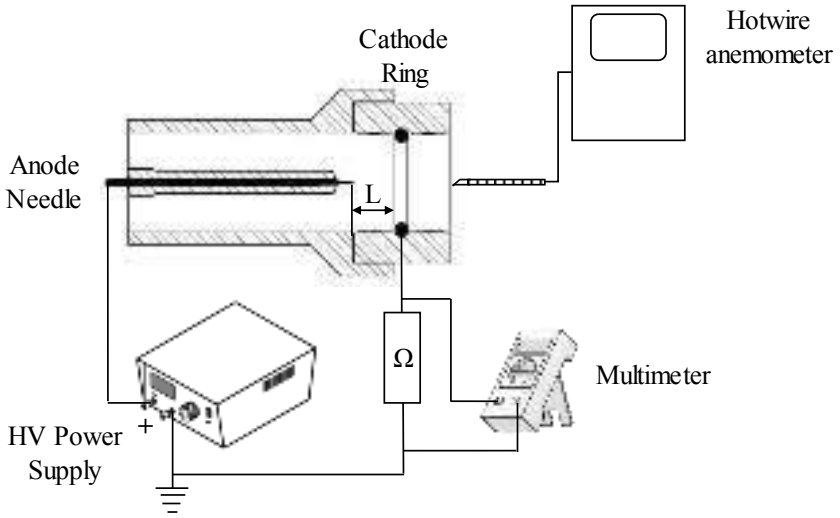

FIG. 3. Schematic of the experimental setup – a high voltage is applied between the corona anode needle and the ion collecting cathode ring. The distance and voltage are varied.

The experimental data are compared with the model in FIG. **4**(a), which shows the comparison of the corona current-voltage relationship. The I/φ vs. φ trends are different from the previously reported linear trends [26,28] for the external flow in point-to-ring corona configuration. The nonlinearity in the analytical model comes from the $\varphi_{\text{cr}}/\varphi_0$ term, as seen in Eq. (44). However, for the high values of φ_0 where most previously reported data was collected, the linear curve fit may have been adequate. These trends can be used to evaluate boundary conditions for modeling of the acceleration region. One approach is to evaluate the critical properties of the acceleration zone at the onset of corona discharge, as the anode voltage approaches the critical voltage, i.e., $\varphi_0 \to \varphi_{cr}$, the $\varphi_{cr} = 2kV$ based on the x-axis. At this condition $r_{cr} \to b$ and EHD flow velocity is negligible. As the corona voltage increases, the size of the acceleration zone r_{cr} and the field intensity increase non-linearly. The current and velocity data in this non-linear region fluctuate, resulting in r_{cr} variations. In the linear region, observed at the higher corona voltages and in previous reports [26,28], both the current values and the EHD velocities were stable indicating well-established ionization and acceleration regions. As in previous work [20,26,28], the acceleration region dimensions are considered constant for a given electrode configuration, i.e., linearly dependent on L. The best fit for the data in the presented point-to-ring internal EHD flow is obtained when $r_{cr} = 3 + 0.5(L-3)$. This relationship is likely to change for a different electrode configuration. The dimensions of the ionization boundary can be approximated as $\frac{\varphi_0}{E_i}$ [173,175]. In the linear regime, we assume $E_i = \alpha E_{cr}$, where E_{cr} is the critical electric field strength at r_{cr}, and α is a scaling factor. Since for $\varphi_0 \to \varphi_{cr}$ (no ionization occurs) $b \to 0$, we consider the following relationship

$$b = \frac{\varphi_0 - \varphi_{cr}}{\alpha E_{cr}} = \frac{\frac{4\rho_0}{3\varepsilon} r_{cr}^{1/2}}{\frac{2\alpha\rho_0}{3\varepsilon} r_{cr}^{-1/2}} = \frac{2}{\alpha} r_{cr}. \tag{52}$$

In this work, the evaluation of α is based on experimental data, the best agreement with data is observed for $\alpha = 8$.

FIG. **4**(b) shows the comparison of the voltage-velocity $(\varphi - u)$ data against the analytical solution for a range of L=3-7 mm and φ=4-10 kV. The trends agree with the previously reported linear

dependence between the maximum velocity and corona voltage observed for the point-to-ring corona configurations [28] and planar electric field ion generator [183]. The analytical solution uses $b = r_{cr} / 4$ as the ionization zone boundary for the integration of Eq. (48). Analytical solutions for corona current and maximum velocity are in very good agreement with the experimental data over the entire range of geometrical and operational parameters of the EHD source.

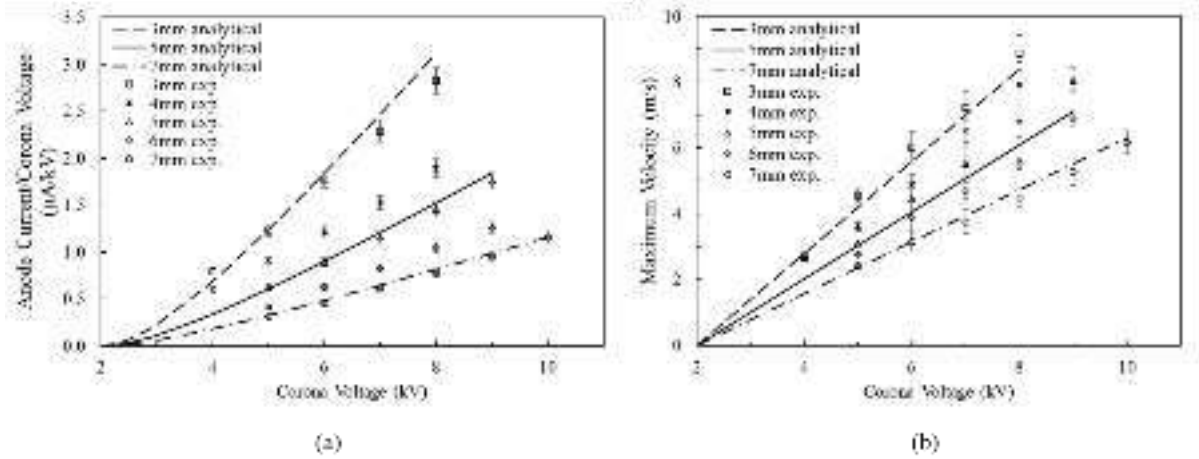

FIG. 4. Current-Voltage $(\varphi - I)$ and Voltage-Velocity $(\varphi - u)$ for the experimental data and the analytical solution.

FIG. 5 shows the velocity profiles at the exit of the point-to-ring EHD flow generator. The velocity profile has some similarities with a momentum point-source jet, with a maximum at the centerline and a steep decrease towards the domain boundaries. Figure 5(a) shows the velocity profile plotted for two voltage values, keeping L constant; the velocity increases with the increase of the corona voltage. Figure 5(b) shows the velocity increase for lower values of L at a fixed corona voltage. Both trends can be explained by the increase in the EHD force driving the flow based on the higher electric field intensity ($E = \phi / L$).

Both the analytical solution and the experimental results show velocity profiles with a very distinct peak at the axis of the coaxial configuration, consistent with the localized electro-hydrodynamic force at the tip of the needle electrode. The velocity profiles then decay quickly over a short radial distance (of the order of the ionization zone width, $r_{cr}/4$) with asymptotic decay towards the edge of the domain, consistent with entrainment in a confined flow environment. The comparison between the analytical solution and the data is excellent at the centerline; the velocity decays approaching the wall is not captured well by the model due to the fully developed assumption

implicit in the model. The balance of the viscous stress term by the EHD forcing at the center of the analytical simplification means that the model assumes the convective term to be negligible. This is not valid in the region where the pipe flow, upstream of the corona discharge, must adapt to the new conditions presented by the EHD forcing near the axis. Additionally, the one-dimensional flow assumption cannot describe the formation of more complex flow patterns in the EHD device, which can form due to adverse pressure and electric field gradients. Here, the EHD force is applied only in the axial direction where it captures well the flow acceleration region near the center line but neglects the effect of the three-dimensional nature of the electric field downstream of the cathode.

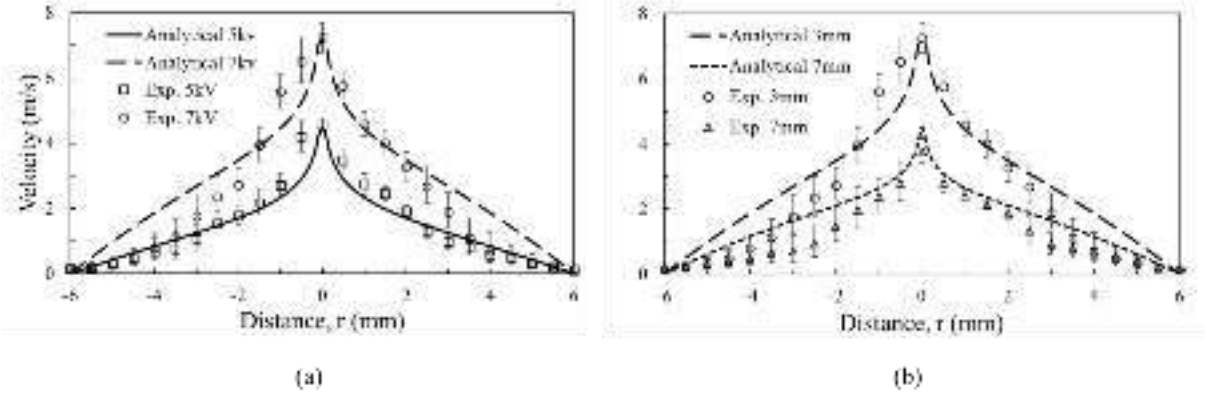

FIG. 5. Comparison between the analytical and the experimental velocity profiles at the outlet of the EHD generator; (a) corona voltages are 5kV and 7 kV, fixed L=3 mm; (b) electrode gaps are 3mm and 7mm, corona voltage is constant (7 kV).

Chapter 3. A FINITE VOLUME MODEL FOR EHD FLOW WITH POSITIVE CORONA DISCHARGE

In this chapter, we demonstrate a numerical approach for EHD modeling flow in a finite volume solver for axisymmetric point-to-ring corona configurations. CFD simulations are used to resolve the spatiotemporal characteristics of the flow, electric fields, and charge density. The nondimensional analysis provides insight into the dominant terms in the different EHD flow regions. The electric to kinetic energy transfer efficiency is evaluated for both the model and the experiments.

3.1 MODEL DEVELOPMENT

3.1.1 *Governing equations*

The effect of the ion motion interaction on the bulk flow is modeled by adding a body force (electric force) $\mathbf{F_e} = -\rho_c \nabla\varphi$ to the momentum equations. The governing equations used to model the flow are:

$$\nabla \bullet \mathbf{u} = 0 \tag{53}$$

$$\rho \frac{D\mathbf{u}}{Dt} = -\nabla P + \mu \nabla^2 \mathbf{u} - \rho_c \nabla\varphi \ , \tag{54}$$

where ρ, the air density ($1.205\ \text{kg/m}^3$), and μ, the air dynamic viscosity [1.846×10^{-5} kg/(ms)], are constant for incompressible isothermal flow, $\mathbf{u} = \left(u_{\text{axial}}, u_{\text{radial}}\right)$ is the velocity vector in the two-dimensional axisymmetric model, and P is the static pressure. The charge density equation describes the ion transport:

$$\frac{\partial \rho_c}{\partial t} + \nabla \bullet \left[\left(\mathbf{u} - \mu_b \nabla\varphi \right) \rho_c - D_c \nabla \rho_c \right] = S_e \, , \tag{55}$$

Note that the $-\nabla\varphi = \mathbf{E}$. The electric potential is solved using Gauss's law:

$$\nabla^2 \varphi = -\frac{\rho_c}{\varepsilon_0} \, , \tag{56}$$

where μ_b is the ion mobility, which is approximated as a constant [2.0×10^{-4} $\text{m}^2/(\text{Vs})$] at standard pressure and temperature [20,176], and ε_0 [$\sim 8.854\times10^{-12}$ C/(Vm)] is the electric permittivity of free space. Since the relative permittivity of air is close to unity (~1.00059) [184], vacuum permittivity is used in all simulations. D_c is the ion diffusivity described by the electric mobility equation (Einstein's relation) [174]:

$$D_c = \frac{\mu_b k_B T}{q} \, , \tag{57}$$

where k_B is Boltzmann's constant ($\sim 1.381\times10^{-23}$ J/K), T is the absolute temperature, and q is the electric charge of an ion, which is equal to the elementary charge (1.602×10^{-19} C).

Ionization is modeled by a volumetric charge flux applied to the fluid within a numerical ionization zone. Instead of defining a surface within the computational domain to model the ionization zone

boundary, the volume of the ionization zone is calculated based on the electric field strength computed in the simulation. In Eq. (55), S_e is the volumetric flux term for charge density with units of C/(m^{3}s) :

$$S_e = \begin{cases} I / \Psi, \text{for } |\mathbf{E}| \in [E_0, E_1] \,\&\, \mathrm{x_{tip}} - \mathrm{x} < 1\,\mathrm{mm} \\ 0, \text{otherwise} \end{cases}, \tag{58}$$

where Ψ is the volume of the numerical ionization zone, calculated in the simulation, it satisfies $|\mathbf{E}| \in [E_0, E_1] \,\&\, \mathrm{x_{tip}} - \mathrm{x} < 1\,\mathrm{mm}$; I is the anode current, measured experimentally and used as a boundary condition in the numerical simulation. The condition $\mathrm{x_{tip}} - \mathrm{x}$ term limits ion production along the needle. It is based on the experimental electrode setup – the tip extends 1 mm from the needle holder. $E_0 = 2.8 \times 10^6$ V/m is the critical field strength below which the number of ion recombination events is greater than the production per drift length for air [15]. $E_1 = 3.23 \times 10^6$ V/m is the breakdown electric field strength for air [2,10]. Since the charge density is balanced in the ionization region, the anode current equals the charge density flux at the ionization boundary.

3.1.2 *Computational domain and conditions*

The numerical model is implemented in a 2D axisymmetric simulation using a general-purpose finite volume solver (ANSYS Fluent). A body force is added to the momentum equation; the ion motion is accounted for by the transport of charge density ρ_c , which is modeled as a user-defined scalar. The corona electrode is located on the axis of the domain, and the cathode ring is modeled as a semi-circle at the wall. Figure 6 shows the schematic diagram of the geometry. The computational domain represents the geometry of the experimental apparatus. The inlet is located 10 mm upstream of the corona needle. The distance between the needle tip and the cathode ring is varied based on the experimental conditions. In the experiment, the needle tip has 1 μm radius of curvature as measured using optical microscopy; it is modeled as a point where the outer wall of the needle body intersects with the axis; these lines intersect at the angle of 1°. The geometry is gridded using ANSYS ICEM software.

The mesh comprises hexagonal cells; after conducting a mesh independence study, the number of cells was ~ 445,000. To balance mesh independence and convergence time, the average mesh size

in the ionization and acceleration regions was $\sim 266\,\mu$m/cell . Due to high drift velocities $\left|\mathbf{u}_{\text{charge}}\right| \sim O(100 m/s)$, the resolution of charge transport requires a time step $\Delta t = 10^{-7}$s to satisfy the Courant-Friedrichs-Lewy condition [185]:

$$\frac{\left|\mathbf{u}_{\text{charge}}\right|\Delta t}{\Delta x} \approx \frac{10^2 \times 10^{-7}}{10^{-5}} \le O(1), \tag{59}$$

where $\mathbf{u}_{\text{charge}} = \mathbf{u} - \mu_b \nabla\varphi$ is the drift velocity of the ions. The simulations are initialized with zero values of pressure, velocity, and charge density. The air flow field and electric field develop spatiotemporally for the set boundary conditions. The steady-state flow is achieved when the outlet velocity profile is independent of the flow time; for most simulations, it is ~1 s (10^7 time steps after initialization). Results are analyzed when steady-state conditions are reached.

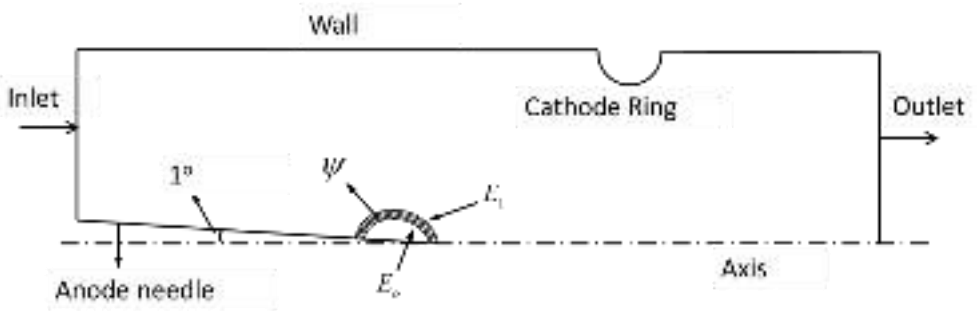

FIG. 6. The computational domain used for the numerical simulation; the model includes the ion generation region Ψ , defined by the thresholds of electric field values: E_0 and E_1 .

Table II summarizes the boundary conditions used in the numerical simulation. The air flow velocity is set to zero at the electrode surfaces and the tube wall due to the no-slip boundary condition. The inlet and outlet are set as atmospheric pressure boundaries. High voltage (4-10 kV) is applied to the anode needle, and zero voltage (grounded) is applied to the cathode ring. Zero electric potential gradient is applied to the other boundaries without solving Eq. (56) within the isolated solid walls. The charge density is set to zero diffusive flux on wall boundaries, similarly to previous modeling work [2,50,87,186]. In this Neumann boundary condition, the charge density at the boundary is extrapolated from the nearest cell.

The simulation resolves the convective flux of charge density, and the ion drift velocity in an electric field is based on Eq. (55)-(56). The current flux at the cathode and the outlet (surface integral of the charge density flux) matches the input anode current, satisfying the conservation of

current density (Kirchhoff's circuit law). The hyperbolic equations of NSE and charge density are resolved using the transient Semi-Implicit Method for Pressure-Linked Equations algorithm [187] with second-order discretization for both space and time. The electric field is resolved by the second order steady-state Poisson equation solver for every time step.

Table II. Boundary conditions for the numerical simulations.

Boundary	Conditions
Inlet pressure	Atmospheric pressure
Outlet pressure	Atmospheric pressure
Anode corona needle	4~11kV & Zero diffusive flux for the charge density
Cathode ring	0kV & Zero diffusive flux for charge
Wall boundaries	Zero gradients for electric potential & Zero diffusive or convection flux for the charge density
Anode current	Based on the experimental measurement

3.2 RESULT AND DISCUSSION

3.2.1 *Numerical simulations*

The numerical model represents the process by which the ion-molecule collisions accelerate the bulk air flow. FIG. 7 (left) shows the electric field lines between the corona electrode and the ground electrode. The greatest field strength is near the tip of the corona electrode with a small radius of curvature where the field intensity reaches the threshold for ion generation. The effect of the space charge on the electric field is apparent near the ionization region where the ion concentration is highest. This field line divergence is greater for higher voltages. The electric field distortion is less significant farther away from the electrode tip since the charge density decays proportionally to $r^{3/2}$ [174,188]. In the $L = 7$ mm case, the field lines are better aligned with the direction of the bulk flow leading to higher energy conversion efficiency, as discussed later in the chapter. FIG. 7 (middle) shows the ion concentration contours. The ions are generated at the needle tip, and their motion is dominated by the electric field due to their very high electric mobility, as the ion drift velocity at about two orders of magnitude greater than the average velocity of the bulk flow. The ions do not drift upstream significantly; some negative axial drift at the needle tip is

observed due to the space charge effect for higher voltage cases, resulting in ions' negative work and reduction in the energy conversion. An annular recirculation flow pattern is formed upstream of the cathode ring near the wall, which is due to the adverse pressure gradient in the near wall acceleration region driven by the high electric field values at the ring electrode, as seen in FIG. 7 (left).

In the region downstream of the ground electrode, the electric field is weak, and some ions exit the domain due to the relatively high flow velocities and the space charge effect (both are the highest at the centerline). The average values of the ion concentration at the device outlet are in the range of 1.7×10^{8} ions/cm^{3} (7 mm, 7 kV) to 3.1×10^{8} ions/cm^{3} (3 mm, 8 kV). These values are of the same order of magnitude as the experimental measurement $\sim 0.6\times10^{8}$ ions/cm^{3} (3 mm, 7 kV), measured 25 mm downstream of the exit. The discrepancy is likely due to the ion dispersion after the flow exits the EHD flow chamber. The ion concentration at the outlet is highest at the axis because: (1) the centerline has the highest velocity, convecting ions from the domain, and (2) the electric field lines near the wall downstream of the ground electrode are pointing in the reverse direction of the bulk flow, resulting in reverse ion drift. The maximum value of the electric field strength is 1.6×10^{8} V/m , and the ion concentration is 1.0×10^{12} ions/cm^{3} , both near the needle tip region of the 3 mm 7 kV case. For better visualization, the values for the electric field and ion concentration contours in FIG. 7 are limited in range.

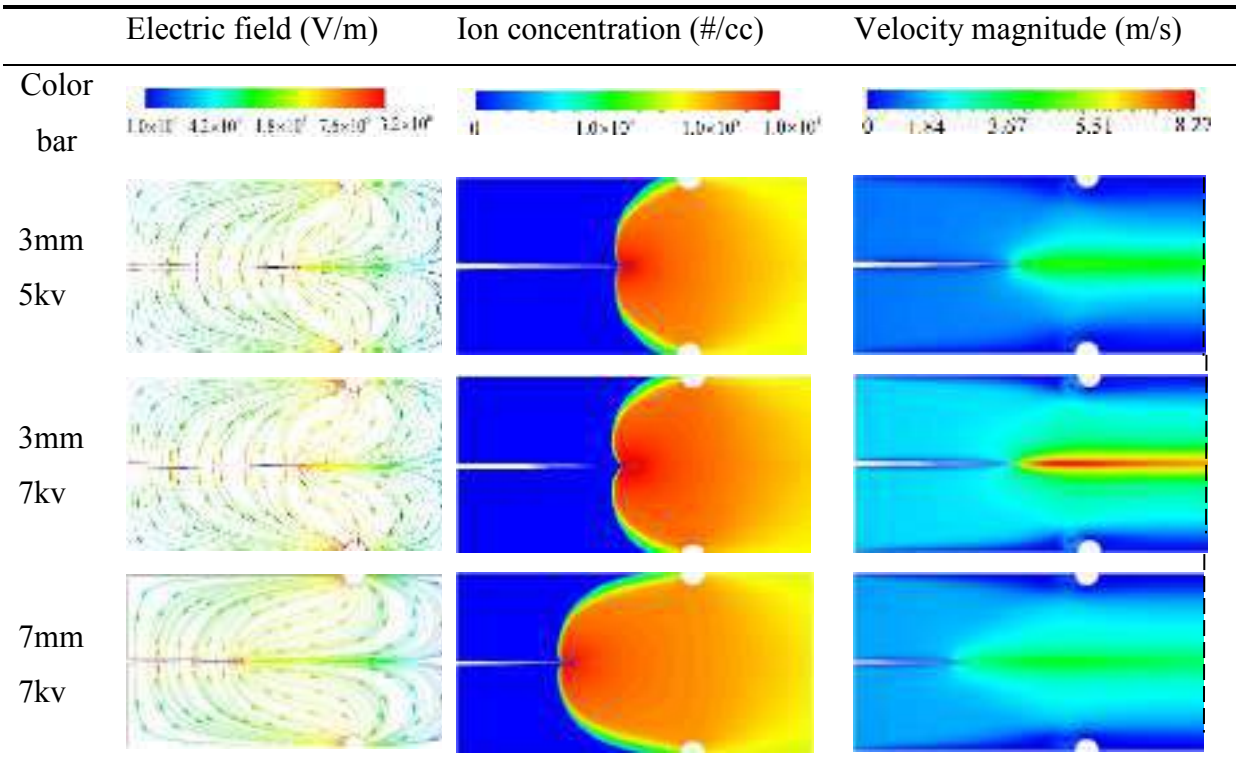

FIG. 7. Plots of the electric field, ion concentration, and velocity for different conditions in the point-to-ring corona generator ($I = 6.15\,\mu\text{A}, 16.04\,\mu\text{A}, 4.28\,\mu\text{A}$, respectively). The dash lines on the velocity contours indicate the location at which the velocity of the EHD flow is compared with the experiments.

3.2.2 *Corona currents*

In previous work, the charge density input in the simulation is "tuned" to match the cathode current measured experimentally using an iterative approach [2,4,5,43-51]. In this work, we directly compute the cathode current based on the boundary conditions; the numerical model uses corona voltage and anode current as input parameters. The comparison of cathode current from the simulation and the experimental values is used for model validation. The cathode current is calculated by integrating the charge density flux on the ground electrode surface:

$$I_{\text{cathode}} = \int_{\substack{\text{cathode}\\ \text{surface}}} -\mu_b \rho_c \nabla\varphi d\mathbf{A}_{\text{cathode}}\,, \tag{60}$$

where $\mathbf{A}_{\text{cathode}}$ is the area vector of the cathode. Table III shows the comparison between the experimentally measured and computed anode and cathode current. The cathode current in the simulation agrees within 5% with the experimental measurements. The cathode recovers 85%~90% of the ion current generated by the corona electrode. The 10%~15% current reduction is associated with ions exiting the domain.

Table III. Comparison of cathode current between the experiments and CFD.

	Experimental Cathode		
	Anode Current (μA)	Current (μA)	CFD Cathode Current (μA)
3mm, 5kV	6.15	5.23	4.99
3mm, 7kV	16.04	14.42	14.21
7mm, 7kV	4.28	3.82	3.64

3.2.3 *Maximum velocity and velocity radial distribution*

To further validate the numerical model, we compare the exit velocities from the experimental data, the analytical solution by Guan et al. [174,188], and the numerical result (FIG. 8) for the $L = 3\,\text{mm} \sim 7\,\text{mm}$ cases and corona voltages of $\varphi = 4 \sim 10\,\text{kV}$. The experiments and simulations show the maximum velocities are on the centerline at the outlet. FIG. 8 shows the comparison. The numerical model agrees within 5% error with the experimental data and the analytical predictions. The analytical predictions are generally higher than the numerical results since it does not account for viscous drag or the nonunidirectional flow. For a given point-to-ring distance, the maximum outlet velocity increases linearly with corona voltage. Zhang *et al.* also observed the linear trend of maximum velocity. in the external flow with point-to-ring corona configurations [28] and by Kim *et al.* for the planar electric field ion generator [183]. For a given corona voltage, the maximum velocity increases as *L* decreases, due to a stronger electric field. The maximum corona voltage, however, is limited by the device glow-to-arc transition limit [15]. When arc discharge happens (in our case 9 kV for L = 3 mm, 10 kV for L = 5 mm, 11 kV for L = 7 mm), the flow velocity reduces to zero. The maximum EHD induced air flow was 9.0 m/s (3 mm 8 kV) from both the experiments and simulations.

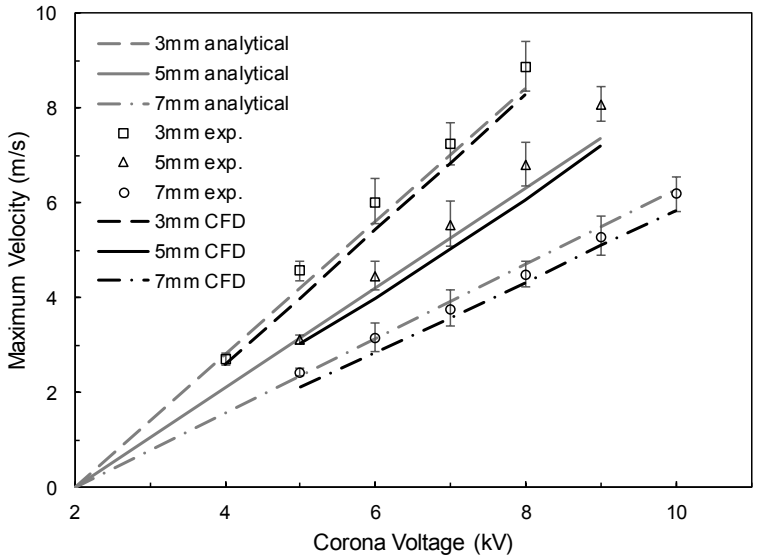

FIG. 8. Maximum velocity as a function of corona voltage and electrode geometry for the experimental data, analytical [174,188], and CFD results.

3.2.4 *Velocity profiles*

To study the spatial distribution of velocity, we compare the numerical and experimental velocity profiles at the outlet of the point-to-ring EHD flow generator. In Fig. 5 (a), the velocity profiles are plotted for two voltage values at a fixed electrode spacing (L = 3 mm). The higher voltage case produces higher velocities with very similar velocity profiles. Figure 5 (b) shows that, at a fixed voltage, the velocity increases when L decreases. Both numerical and experimental results show a distinct peak at the axis, consistent with the results in FIG. 7. The velocity profiles then decay rapidly with radial distance. Numerical and experimental results agree within 5% error at the centerline, but the model is less accurate at the edges of the domain. The discrepancy in this region may be due to flow instability in the shear flow region that modifies the radial location of the inflection points in the velocity profile.

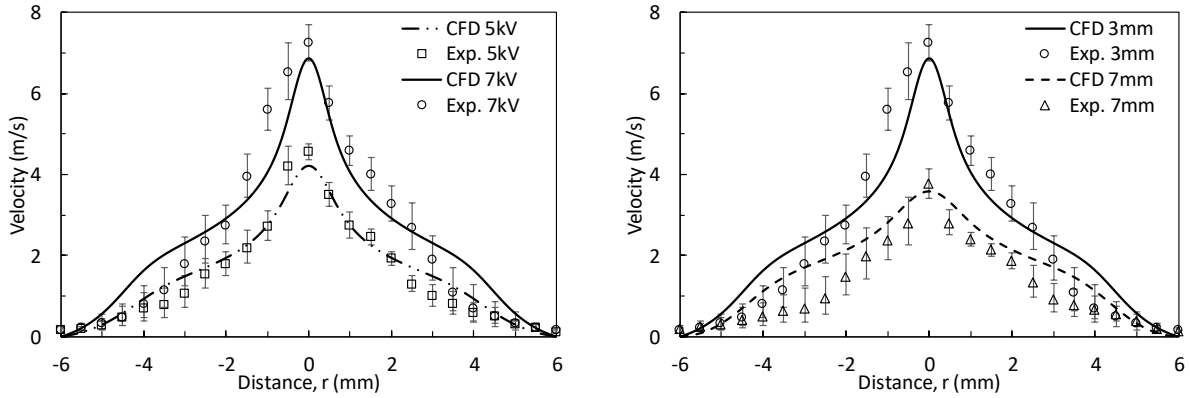

(a) (b)

FIG. 9. Comparison between simulations and experiments for the velocity profiles at the outlet of the EHD generator; (a) varying corona voltages at a fixed distance, and (b) varying anode-cathode distance (L) at a fixed corona voltage.

The velocity profile shows that the EHD-induced airflow in a point-to-ring corona discharge has parallels to a submerged jet [189]. For submerged jets, the Reynolds number is determined based on the nozzle diameter and the mean velocity at the exit [190]. In the case of corona discharge flow, the nozzle is replaced by the EHD jet located at the centerline, immediately downstream of the corona electrode tip. The Reynolds number (Re) in the EHD flow is ~ 700-900, based on the diameter of the jet, for L = 3 mm, 7 kV, d_{jet} ~ 2-3 mm, and mean velocity u ~ 4-5.5 m/s. Other cases have smaller Re due to lower jet velocities, except for the 3 mm, 8 kV case, where Re is still < 1000 ($\sim 6.5\,\text{m/s}$ in mean velocity and d_{jet} ~ 2-3 mm). Therefore, the EHD flow can be represented by a fully laminar jet ($300 < \text{Re} < 1000$) [190].

Chapter 4. NON-DIMENSIONAL ANALYSIS FOR EHD FLOW WITH POSITIVE CORONA DISCHARGE

In this chapter, we proposed a new nondimensional parameter *X*, which represents the ratio of electric force to inertia. We further showed that *X* could be used as an indicator of the flow region where the electric force dominates the flow.

The simulation shows that the EHD force drives local flow accelerations. The global parameters used in the analytical model and ones reported in the literature for a description of the EHD flow

do not account for spatial distributions in ρ_e and φ. Further insight into the development of EHD flow in different regions of the geometry can be gained by nondimensional analysis. The nondimensional EHD equation can be written as:

$$St\frac{\partial \mathbf{u}^*}{\partial t^*}+\left(\mathbf{u}^*\bullet\nabla^*\right)\mathbf{u}^*=-\nabla^*P^*+\frac{1}{Fr^2}\mathbf{g}^*+\frac{1}{Re}\nabla^{*2}\mathbf{u}^*-\underbrace{\left[\frac{\rho_c\varphi}{\rho\mathbf{u}^2}\right]}_{X}\rho_c^*\nabla^*\varphi^*, \tag{61}$$

where *St* is the Strouhal number, *Fr* is the Froude number, the asterisk superscript denotes nondimensional variables [191]. A proposed nondimensional parameter, $X=\rho_c\varphi/\rho\mathbf{u}^2$, is defined as the ratio of electrostatic to inertial terms. In global terms, the parameter X is related to the electro-inertial number $N_{\mathrm{EI}}=\varepsilon\left|\vec{E}\right|^2/\rho\mathbf{u}^2$ [192], described in the literature as Md/Re^2, where $|\mathbf{E}|$ is the magnitude of the electric field vector, and Md is the Masuda number [193]. The parallels come from the electric description based on Gauss's law. Gauss's law can be written in a nondimensional form as

$$\frac{\varphi}{L^2}\nabla^{*2}\varphi^*=-\frac{\rho_c}{\varepsilon}, \tag{62}$$

$$\frac{\varphi}{L}\nabla^*\varphi^*=-|\mathbf{E}|. \tag{63}$$

Since $\nabla^{*2}\varphi^*$ and $\nabla^*\varphi^*$ are nondimensional parameters, re-arranging the Eq. (62) and Eq. (63) gives:

$$\varepsilon|\mathbf{E}|^2=\rho_c\varphi, \tag{64}$$

where the dimension of both terms in Eq. (64) is the same. The main difference is that the parameter X can be resolved spatially. Nondimensional analysis of the EHD system that does not include the spatial inhomogeneity of ρ_c and φ fails to describe the local effects of the electrostatic force on the flow because Md and N_{EI} can be used only as global parameters. To gain insight into corona-driven EHD flow, the electric force and flow inertial and viscous terms have to be resolved spatially. The nondimensional parameter, *X*, can be computed directly from the governing equations for each region of the flow, providing the relative contribution of the terms locally. Cotton et al. suggests that, when the electro-inertial number is greater than unity, the flow is dominated by the EHD force [194]. Though the analysis is valid as an order of magnitude estimation of the system, in our modeling, the use of the conventional N_{EI} formulation led to over-estimating the effect of EHD in regions with low charge density and strong electric field, such as the region

upstream of the corona electrode tip (shown in the appendix). In this region, the ion-molecule collision cannot drive the flow since their concentration of ions is too low. FIG. 10 shows electric field lines colored by the values of *X*, indicating the regions where the electric force is higher than the inertial force. The EHD-dominated flow (red) is located between the corona and ground electrode where both the ion concentration and the electric field strength are high (see FIG. 7). In the 7 mm case, the red vectors are well aligned with the flow direction, which results in a higher energy transfer efficiency than in the 3 mm cases (FIG. 11). There exists another EHD-dominated region located at the edge of the domain where the electric lines are pointing in the opposite direction of the main flow; the inertial flow component in this region is very small. The small denominator in the calculation of parameter *X* results in its high values (up to 400). The negative electric force, combined with the high viscous stress, explain the low-velocity region at the edge of the domain (see FIG. 9).

To evaluate the non-dimensional parameters in the EHD domain, electric field lines are plotted colored by parameter *X* and by the local electro-inertia number N_{EI}. The local values of N_{EI} overpredict the effect of the electric force in the region where the charge density is low. This N_{EI} parameter was originally developed to represent global properties of the EHD system and does take into account the effects of the local electric field and charge density variations. Thus, it is erroneous to use N_{EI} for this purpose. From the first principles considerations, the region with near zero charge density will not experience body force as the ions are not present. Charge density, however, is explicitly related to the proposed parameter *X*, which serves as a better indicator for the region dominated by the EHD force.

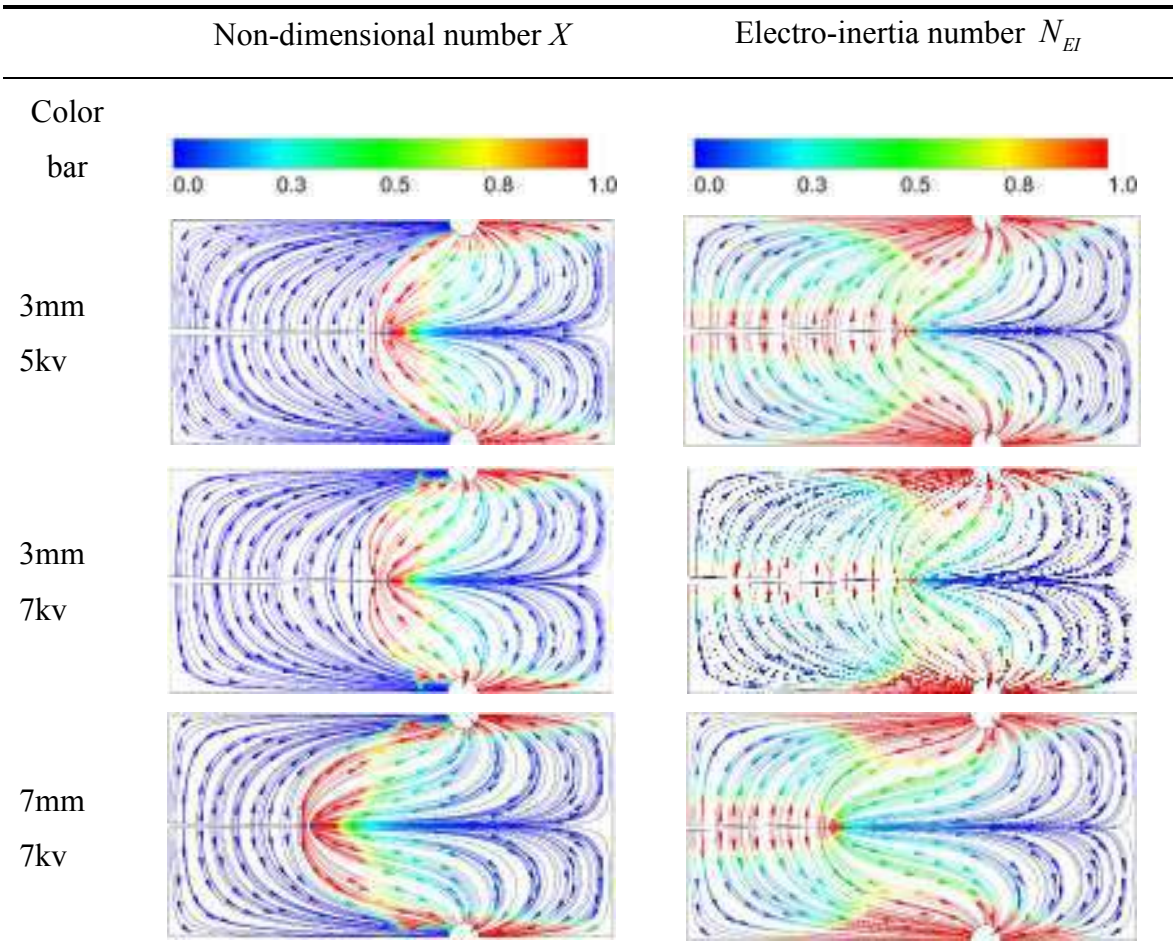

FIG. 10. Electric field lines colored by non-dimensional parameter X (left) and electro-inertia number (right) of three cases. The red zone, $X \geq 1$, indicates the regions of EHD-dominated flow. The color map is limited to X=1; the value X is as high as 400 in the regions near the ionization zone and the low-velocity region near the wall.

Chapter 5. ENERGY TRANSFER IN CORONA DISCHARGE-DRIVEN FLOW

In this chapter, we study the energy conversion efficiency in the point-to-ring corona discharge EHD propulsion device. We proposed an energy conversion ratio to measure efficiency. The anode input power is calculated from the anode voltage and current, and the kinetic power of the airflow is calculated from the velocity profile at the outlet of the device.

The energy conversion efficiency can be calculated from the ratio of the kinetic energy flux in the flow at the exit of the EHD device to the electric power produced by the corona discharge:

$$\eta = \frac{\frac{1}{2}\rho\int u^3 dA}{\varphi I} \quad . \tag{65}$$

The corona voltage and anode current are obtained from the experiments. The kinetic energy flux in the flow is calculated from both the experimental and numerical velocity profiles.

Table IV shows the values used in the calculation of energy transfer efficiency.

Table IV. Comparison of electric and fluid power between the experiments and the CFD.

	3 mm, 5 kV	3 mm, 7 kV	7 mm, 7 kV
$W_{K,Exp}(mW)$	$0.196 \pm 16\%$	$0.882 \pm 19\%$	$0.264 \pm 23\%$
$W_{K,CFD}(mW)$	0.184	0.86	0.293
$I(\mu A)$	6.15	16.04	4.28
$W_E(mW)$	30.8	112.28	29.96

Energy transfer efficiency is shown in FIG. 11. The numerical results agree well with the efficiency computed using the experimental data. Efficiency is higher in the 7 mm cases than in the 3 mm cases due to the smaller angle between the axial velocity and the electric field vectors, as is shown in FIG. 11. Energy transfer efficiency peaks at a certain corona voltage (7 kV for 3 mm, and 8 kV for 7 mm) after which the efficiency decreases. This nonlinear effect is likely due to the quadratic relationship between the corona voltage and anode current. The increase in corona voltage results in a quadratic increase in the anode current and a cubic increase in electric power $\varphi I \propto \varphi^3$. Maximum velocity at the centerline is linearly proportional to the corona voltage based on the analytical solution and previously reported experimental observations, but the kinetic power $\frac{1}{2}\rho\int u^3 dA$ is not proportional to φ^3 because u is not proportional to φ anywhere but on the centerline. At the high values of the corona voltage, the field lines also diverge due to the high space at the corona needle (see FIG. 7 and FIG. 10) resulting in a negative work of the electric field.

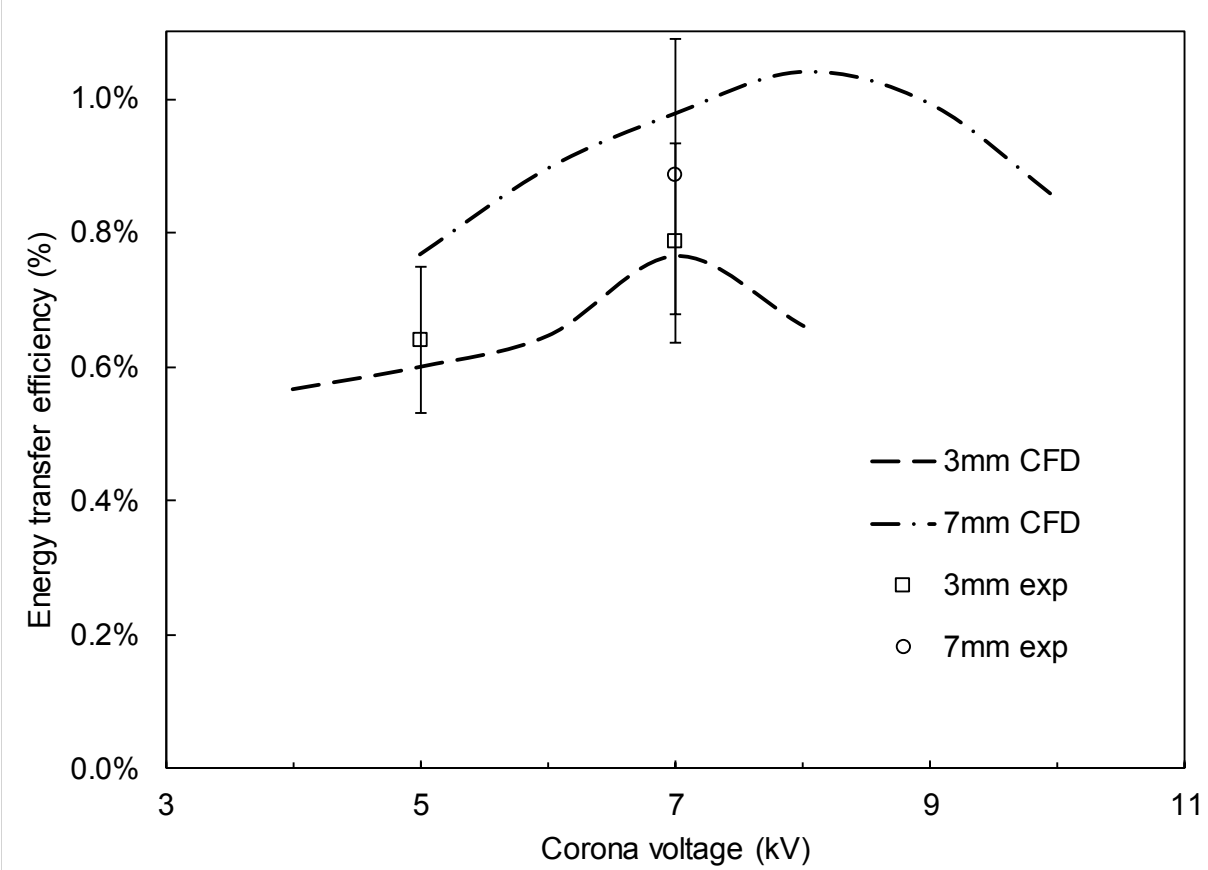

FIG. 11. Energy transfer efficiency from the experiments (symbols) and simulations (dashed and dash-dotted lines).

Chapter 6. LAMINAR EHD BOUNDARY LAYER FLOW

In this chapter, we study the EHD flow in the boundary layer. Modification of the boundary layer using EHD is beneficial to the aeronautic industry because no mechanical moving part are required to influence the flow. The EHD can be used to modify the laminar-turbulent transition at high Reynolds number. It can also be implemented to reduce the drag on the moving body or to stabilize the flow to avoid flow separations, unwanted vibrations, and noise[68].

Here we develop a finite difference code to solve the governing equations. The pressure projection method is an efficient method to solve the incompressible Navier-Stokes Equations (NSE)[195-197]. The numerical method includes a 4-step Runge-Kutta method in temporal discretization and center difference method in spatial discretization [198-201]. The Poisson equations for pressure correction

and electric potential are solved directly based on a sparse multifrontal variant of Gaussian elimination [202].

6.1 COMPUTATIONAL DOMAIN

FIG. 12 shows the schematic of the flow over a flat plane with an ionization source located in the boundary layer. Uniform flow profile is imposed at the inlet. The flow encounters a rough wall (modeled as a no-slip boundary) and the electrodes. Laminar boundary layer develops, which is affected by the EHD.

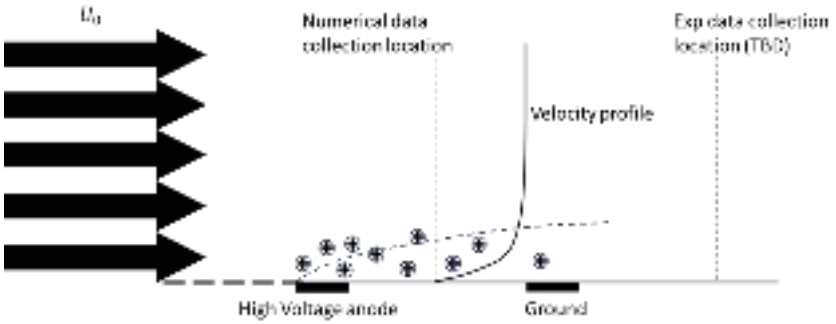

FIG. 12. Schematic of the laminar boundary layer with EHD flow near the wall

6.2 GRID GENERATION

FIG. 13 shows the staggered grid used in the numerical simulation. Pressure and electric field values are collocated while other variables, i.e., 2-dimensional velocities and charge density values are located in different grid points. This treatment is used to prevent odd-even decoupling instability (checkerboard instability) introduced by the central differencing schemes[199,203, 204].

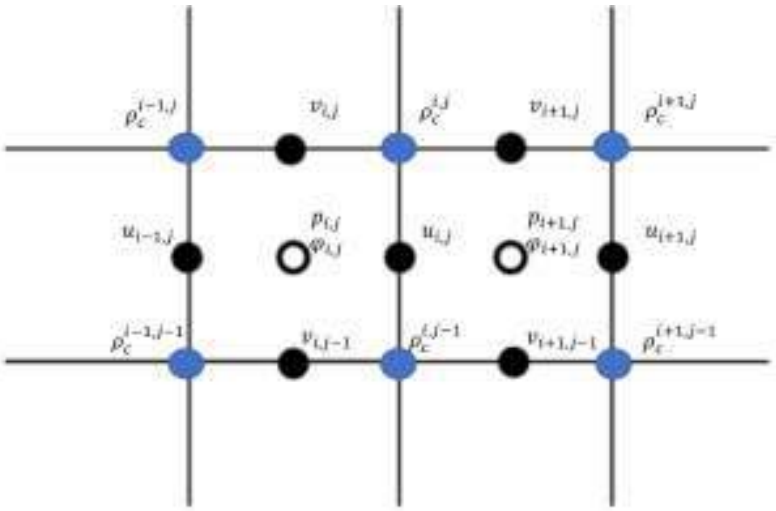

FIG. 13. The staggered grid method is used to prevent decoupling instability

To fully resolve the laminar boundary layer, the height of the computational domain is about 20 times the boundary layer thickness; boundary layer is resolved by ~30 grid points. Such requirements result in a large computational cost if the grid points are evenly distributed. Therefore, grid stretching is applied to reduce the computational cost. Two monotonic stretching functions are as follows [205,206]:

Two-way grid stretching function is given by:

$$y = \frac{H}{2}\left[1 + \frac{\tanh\left(\gamma_y\left(\frac{\eta}{H} - \frac{1}{2}\right)\right)}{\tanh\gamma_y / 2}\right]. \tag{66}$$

And the one-way grid stretching function is given by:

$$y = H\left[1 - \frac{\tanh\left(\gamma_y\left(H - \eta\right)\right)}{\tanh\gamma_y H}\right]. \tag{67}$$

where γ_y is the control parameter, H is the height of the computational domain and η is the vertical direction of the computational grid.

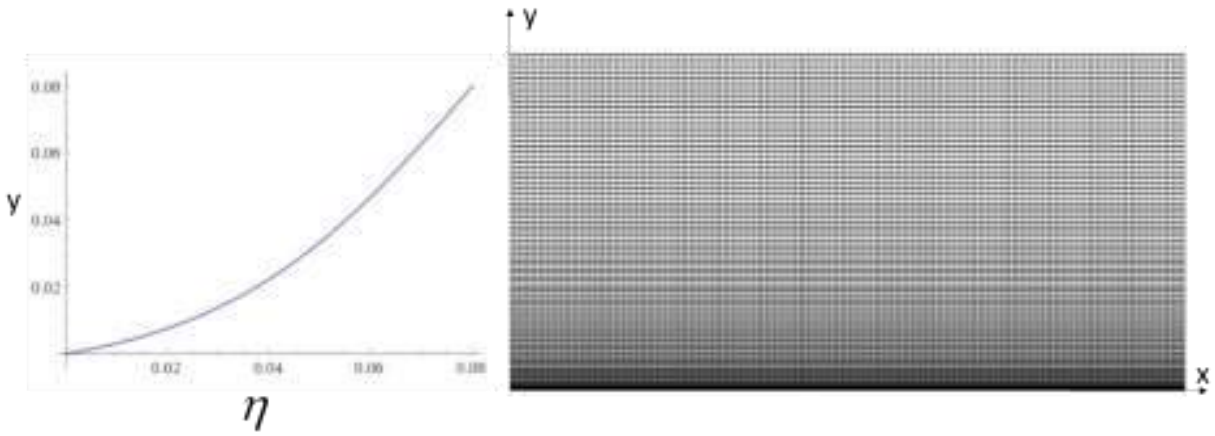

FIG. 14. Grid stretching function (one-way, Eq. (67)) with *H*=0.08 and $\gamma_y = 20$ (left) and the corresponding mesh (right)

6.3 NUMERICAL METHOD

The pressure projection method[198,199] is used in solving the boundary layer flow, which is governed by Eq. (53)-(56)with zero charge source term $S_e = 0$. Unlike the finite volume method discussed in Chapter 3, the finite difference method is unable to capture the finite numerical ionization zone. Therefore, the positive charge injection is modeled at the anode surface with a constant charge density and electric field based on Kaptsov's assumption[52].

Two potential schemes are evaluated. In the first scheme, the electric force is solved with the intermediate velocity $\mathbf{u}^{k+1/2}$.

$$\frac{\mathbf{u}^{k+1/2}-\mathbf{u}^{k}}{\Delta t}=-\nabla\bullet\left(\mathbf{u}\otimes\mathbf{u}\right)^{k}+\nu\nabla^{2}\mathbf{u}^{k}-\frac{\rho_{c}^{k}\nabla\varphi^{k}}{\rho}. \tag{68}$$

$$\nabla^{2}\varphi^{k+1}=-\frac{\rho_{c}^{k}}{\varepsilon}. \tag{69}$$

$$\frac{{\rho_{c}}^{k+1}-{\rho_{c}}^{k}}{\Delta t}=\left(\mu_{b}\nabla\varphi^{k+1}-\mathbf{u}^{k}\right)\nabla\rho_{c}^{k}+D_{c}\nabla^{2}\rho_{c}^{k}-\frac{\mu_{b}\left(\rho_{c}^{k}\right)^{2}}{\varepsilon}. \tag{70}$$

$$\nabla^{2}p^{k+1}=\frac{\rho}{\Delta t}\left(\nabla\bullet\mathbf{u}^{k+1/2}\right). \tag{71}$$

$$\frac{\mathbf{u}^{k+1}-\mathbf{u}^{k+1/2}}{\Delta t}=-\frac{1}{\rho}\nabla p^{k+1}. \tag{72}$$

For the second approach, the electric force is solved with pressure correction and the final velocity $\mathbf{u}^{k+1}$.

$$\frac{\mathbf{u}^{k+1/2}-\mathbf{u}^{k}}{\Delta t}=-\nabla\bullet\left(\mathbf{u}\otimes\mathbf{u}\right)^{k}+\nu\nabla^{2}\mathbf{u}^{k}. \tag{73}$$

$$\nabla^{2}\varphi^{k+1}=-\frac{\rho_{c}^{k}}{\varepsilon}. \tag{74}$$

$$\frac{{\rho_{c}}^{k+1}-{\rho_{c}}^{k}}{\Delta t}=\left(\mu_{b}\nabla\varphi^{k+1}-\mathbf{u}^{k}\right)\nabla\rho_{c}^{k}+D_{c}\nabla^{2}\rho_{c}^{k}-\frac{\mu_{b}\left(\rho_{c}^{k}\right)^{2}}{\varepsilon}. \tag{75}$$

$$\nabla^{2}p^{k+1}=\frac{\rho}{\Delta t}\left(\nabla\bullet\mathbf{u}^{k+1/2}\right)-\nabla\left(\rho_{c}^{k+1}\nabla\varphi^{k+1}\right). \tag{76}$$

$$\frac{\mathbf{u}^{k+1}-\mathbf{u}^{k+1/2}}{\Delta t}=-\frac{1}{\rho}\left(\nabla p^{k+1}+\rho_{c}^{k+1}\nabla\varphi^{k+1}\right). \tag{77}$$

Both methods produce similar results. The following numerical results are solved by the former method due to its computational efficiency. Second-order spatial discretization is used. 4-step Runge-Kutta scheme[198,199] is used for temporal discretization for its higher stability region. The numerical method is implemented in FORTRAN 90 and compiled with GNU fortran compiler using -Ofast optimization. The Courant-Friedrichs-Lewy condition is satisfied with the freestream velocity and the height of the first grid layer. The steady state solution is obtained when the velocity profile does not change with time.

6.4 BOUNDARY CONDITIONS

The boundary conditions used in the simulation finite difference method is given in **Table V**.

Table V. Boundary conditions for the numerical simulations for the EHD boundary layer

Boundary	Flow variables Conditions	Electric variables Conditions
Inlet	Uniform velocity, $\frac{\partial p}{\partial x}=0$	$\frac{\partial \varphi}{\partial x}=0$, $\rho_c=0$
Outlet	$\frac{\partial \mathbf{u}}{\partial x}=0$, $p=0$	$\frac{\partial \varphi}{\partial x}=0$, $\frac{\partial \rho_c}{\partial x}=0$
Upper boundary	$\frac{\partial \mathbf{u}}{\partial y}=0$, $p=0$	$\frac{\partial \varphi}{\partial y}=0$, $\rho_c=0$
Lower wall (slip)	$\frac{\partial \mathbf{u}}{\partial y}=0$, $\frac{\partial p}{\partial y}=0$	$\frac{\partial \varphi}{\partial y}=0$, $\frac{\partial \rho_c}{\partial y}=0$
Lower wall (non-slip)	$\mathbf{u}=0$, $\frac{\partial p}{\partial y}=0$	$\frac{\partial \varphi}{\partial y}=0$, $\frac{\partial \rho_c}{\partial y}=0$
Anode	$\mathbf{u}=0$, $\frac{\partial p}{\partial y}=0$	φ and ρ_c are constants
Cathode	$\mathbf{u}=0$, $\frac{\partial p}{\partial y}=0$	$\varphi=0$, $\frac{\partial \rho_c}{\partial x}=0$

6.5 NUMERICAL RESULTS

We study an electrode configuration and operating conditions which are similar to Moreau et al.[68]. The distance between anode and cathode is 40cm. The external flow is 1m/s. The high voltage anode is set at $\varphi = 32kV$, the current $I = 0.75mA$. **FIG. 15** shows the velocity profile with and without EHD effect. The numerical data are obtained at the 10mm upstream of the cathode as shown (disproportionately) in **FIG. 12**. The numerical results match the analytical ones very well for laminar boundary layer[69-71]. Comparison with the experimental data will be completed once is the data are available.

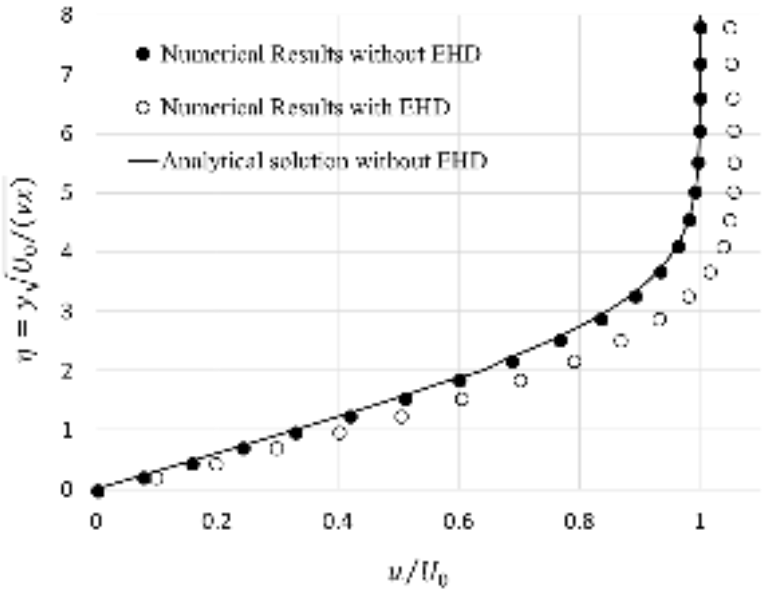

FIG. 15. Velocity profile of laminar boundary layer with or without EHD effect

FIG. 16 shows the velocity, electric potential, and charge density contours for laminar boundary layer flows with EHD effect. The velocity contour resembles the classical laminar boundary layer. The electric potential contour indicates the electric field between the surface anode and cathode. The charge density contour shows the transport of charge from anode to cathode (high electric potential to low potential). With the effect of the external electric field, the charge accelerates the flow by collision within the laminar boundary layer. Although the effect is not obvious from the velocity contour FIG. 16 (left), an increase in the velocity profile is observed, as in FIG. 15.

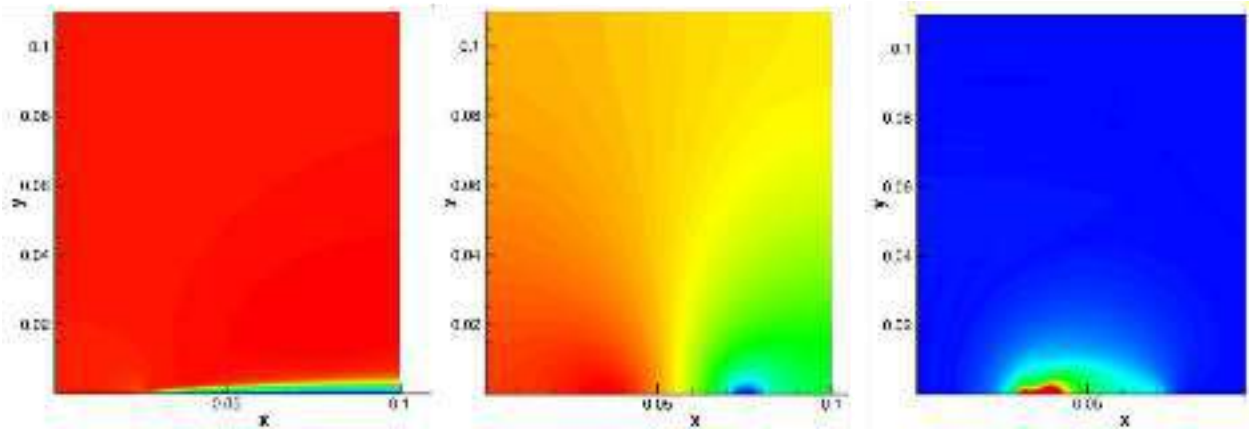

FIG. 16. Velocity(left), Electric potential(middle) and charge density(right) contours of laminar boundary layer with EHD flow

Chapter 7. ANALYSIS OF HYDRODYNAMIC STABILITY OF ELECTROCONVECTION

In this chapter, we demonstrate an alternative approach to modeling an EHD flow; our segregated solver combines (i) a two-relaxation-time (TRT) LBM [59,207-215] for modeling fluid transport and charged species, (ii) a Fast Fourier Transform (FFT) [177,179,216,217] Poisson approach for solving for the electric field directly. The TRT model introduces two relaxation parameters aiding the numerical algorithm stability without sacrificing computational efficiency.

We use this numerical method to parameterize the EC stability in the cross-flow between two parallel electrodes, as shown in FIG. 17. Couette and Poiseuille cross-flow scenarios provide shear stress; the dominant terms are determined from non-dimensional analysis of the governing equations. A subcritical bifurcation is described by the ratio of the electric force to the viscous force. FIG. 17 shows the schematic of the numerical domain. Two parallel plates are infinitely long in x and y directions, which is treated as periodic numerically. The ions drift from the high voltage injector to the grounded collector, forming an unstable equilibrium base-state. The base-state is perturbed by different patterns, as shown in FIG. 25.

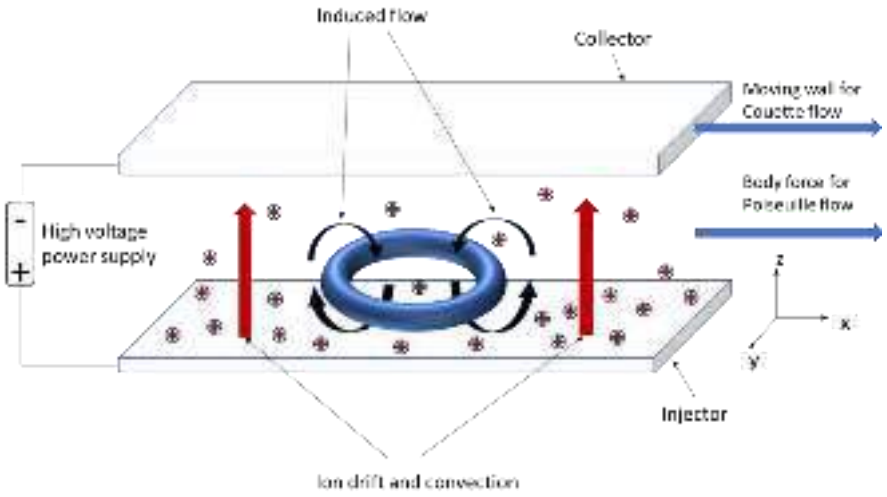

FIG. 17. The EC between parallel electrode. Positive ions drift from anode (lower plane) to cathode (upper plane).

Furthermore, we study the 3D effect of EC affected by cross-flow. Couette or Poiseuille cross-flow is added to EC convection before and after the vortices are established. DMD analysis of the numerical solution sheds insight into the formation and pattern transitions of 2D and 3D coherent fluid structures. The effects of cross-flow are parameterized by a non-dimensional number, *Y*, a ratio of electric to viscous forces.

7.1 GOVERNING EQUATIONS AND NON-DIMENSIONAL ANALYSIS

The governing equations of EC flow are the Navier-Stokes equations (NSE) with an electric forcing term $\mathbf{F_e} = -\rho_c \nabla\varphi$ added to the momentum equation, the charge transport equation, and the Poisson equation for electric potential.

$$\nabla \bullet \mathbf{u} = 0 \ , \tag{78}$$

$$\rho \frac{D\mathbf{u}}{Dt} = -\nabla P + \mu \nabla^2 \mathbf{u} - \rho_c \nabla\varphi \ , \tag{79}$$

$$\frac{\partial \rho_c}{\partial t} + \nabla \bullet \left[\left(\mathbf{u} - \mu_b \nabla\varphi \right) \rho_c - D_c \nabla \rho_c \right] = 0 \, , \tag{80}$$

$$\nabla^2 \varphi = -\frac{\rho_c}{\varepsilon} \, . \tag{81}$$

where ρ and μ are the density and the dynamic viscosity of the working fluid, $\mathbf{u} = \left(u_x, u_y, u_z \right)$ is the velocity vector field, P is the static pressure, ρ_c is the charge density, μ_b is the ion mobility, D_c is the ion diffusivity, ε is the electric permittivity, and φ is the electric potential. The electric force is a source term in the momentum equation (Eq. (79)) [28,32,81,174]. The variables to be solved are velocity field $\mathbf{u}$, pressure P, charge density ρ_c, and electric potential φ. The flow is assumed to be periodic in the x- and y-directions, and wall-bounded z-direction. Cross-flow is applied in the x-direction.

In the absence of cross-flow, the system can be non-dimensionalized with the characteristics of the electric field[81], i.e., H is the distance between the electrodes (two plates infinite in x and y), ρ_0 is the injected charge density at the anode, and $\Delta\varphi_0$ is the voltage difference applied to the electrodes. Respectively, the time t is non-dimensionalized by $H^2 / \left(\mu_b \Delta\varphi_0 \right)$, the velocity $\mathbf{u}$ by the drift

velocity of ions $u_{drift} = \mu_b \Delta\varphi_0 / H$, the pressure P by $\rho_0 \left(\mu_b \Delta\varphi_0\right)^2 / H^2$, and the charge density ρ_c by ρ_0. Therefore, non-dimensionalization of the governing equations (Eq. (78)-(81)) gives:

$$\nabla^* \bullet \mathbf{u}^* = 0, \tag{82}$$

$$\frac{D^*\mathbf{u}^*}{D^*t^*} = -\nabla^* P^* + \frac{M^2}{T}\nabla^{*2}\mathbf{u}^* - CM^2 \rho_c^* \nabla^* \varphi^*, \tag{83}$$

$$\frac{\partial^* \rho_c^*}{\partial^* t^*} + \nabla^* \bullet \left[\left(\mathbf{u}^* - \nabla^* \varphi^*\right)\rho_c^* - \frac{1}{Fe}\nabla^* \rho_c^* \right] = 0, \tag{84}$$

$$\nabla^{*2}\varphi^* = -C\rho_c^*. \tag{85}$$

where the asterisk denotes non-dimensional variables. These non-dimensional equations yield four dimensionless parameters describing the system's state [74,76,77,79,81-90].

$$M = \frac{\left(\varepsilon / \rho\right)^{1/2}}{\mu_b}, \quad T = \frac{\varepsilon \Delta\varphi_0}{\mu\mu_b}, \quad C = \frac{\rho_0 H^2}{\varepsilon\Delta\varphi_0}, \quad Fe = \frac{\mu_b \Delta\varphi_0}{D_e}, \tag{86}$$

where H is the distance between the electrodes (two plates infinite in x and y), ρ_0 is the injected charge density at the anode, and $\Delta\varphi_0$ is the voltage difference applied to the electrodes. The physical interpretations of these four non-dimensional parameters are as follows: M is the mobility ratio between hydrodynamic mobility and the ionic mobility; T is the electric Rayleigh number, a ratio between the electric force to the viscous force; C is the strength of injection [81,86]; and Fe is the reciprocal charge diffusivity coefficient [81,86].

With the addition of a cross-flow, the velocity term in the non-dimensional momentum equation is modified to account for the external flow, $\mathbf{u}_{ext}$, which is different from the previous formulations where the drift charge velocity was used [143]. Here we consider the velocity of the upper wall in Couette flow or the centerline velocity for Poiseuille flow as $\mathbf{u}_{ext}$ [143]. The non-dimensional equations then become:

$$\nabla^* \bullet \mathbf{u}^* = 0, \tag{87}$$

$$\frac{D^*\mathbf{u}^*}{D^*t^*} = -\nabla^* P^* + \frac{1}{\mathrm{Re}}\nabla^{*2}\mathbf{u}^* - \left[\frac{\rho_0 \Delta\varphi_0}{\rho \mathbf{u}_{ext}^2}\right]\rho_c^* \nabla^* \varphi^* , \tag{88}$$

$$\frac{\partial^* \rho_c^*}{\partial^* t^*} + \nabla^* \bullet \left[\left(\frac{u_{ext}}{u_{drift}}\mathbf{u}^* - \nabla^* \varphi^*\right)\rho_c^* - \frac{1}{Fe}\nabla^* \rho_c^*\right] = 0, \tag{89}$$

$$\nabla^{*2}\varphi^* = -C\rho_c^* . \tag{90}$$

where the Reynolds number is $Re = \frac{\rho \mathbf{u}_{ext} H}{\mu}$, and $X = \frac{\rho_0 \Delta\varphi_0}{\rho \mathbf{u}_{ext}^2}$ is a ratio of electric force to inertial force [174]. Since Re is essentially the ratio of inertia to viscous force, and X is the ratio of electric force to inertia, the product of these (denoted as *Y*) is the ratio of the electric force to the viscous force:

$$Y = X \times \mathrm{Re} = \frac{\rho_0 \Delta\varphi_0 H}{\mu \mathbf{u}_{ext}} = \frac{\rho_0 \Delta\varphi_0}{\boldsymbol{\tau}}, \tag{91}$$

where $\boldsymbol{\tau}$ is the shear stress $\boldsymbol{\tau} = \mu\frac{\mathbf{u}_{ext}}{H}$. In Couette flow $\boldsymbol{\tau}$ = *constant* ($\mathbf{u}_{ext} = u_{wall}$); while in Poiseuille flow, the average value in the channel flow is used hereafter ($\mathbf{u}_{ext} = u_{center}$ and *H* replaced by half height *H*/2). The parameter *Y* is analogous to the electro-viscous number determined by Md / Re [192,193], with the permittivity is replaced by an explicit number of charge density.

7.2 SYSTEM LINEARIZATION AND INITIALIZATION

In problems of flow stability, the initial linear growth region can be described by the linearized governing equations. The dimensional variables can be written as a summation of the base state (with an overbar) and perturbation (with prime), i.e., $u = \bar{u} + u'$, $P = \bar{P} + P'$, $\varphi = \bar{\varphi} + \varphi'$, and $\rho_c = \bar{\rho}_c + \rho_c'$ [81]. The base state variables are only functions of z. Substituting these expressions into Eq. (78)-(81), subtracting the governing equations for the base states, and truncating the second order perturbation terms, give the linear system

$$\nabla \bullet \mathbf{u}' = 0\,, \tag{92}$$

$$\rho \frac{\partial\, \mathbf{u}'}{\partial\, t} + \left(\mathbf{u}' \bullet \nabla\ \right)\bar{\mathbf{u}} + \left(\bar{\mathbf{u}} \bullet \nabla\right)\mathbf{u}' = -\nabla P' + \mu \nabla^2 \mathbf{u}' - \left(\rho_c'\nabla\ \bar{\varphi} + \bar{\rho}_c \nabla\ \varphi'\right)\,, \tag{93}$$

$$\frac{\partial \rho_c}{\partial t} + \nabla \bullet \left[\left(\bar{\mathbf{u}} - \nabla \bar{\varphi}\right)\rho_c' + \left(\mathbf{u}' - \nabla \varphi'\right)\bar{\rho}_c - D_c \nabla \rho_c'\right] = 0\,, \tag{94}$$

$$\nabla^2 \varphi' = -\frac{\rho_c'}{\varepsilon}\,. \tag{95}$$

The linear system can be written symbolically as

$$\frac{d\boldsymbol{\gamma}}{dt} = \mathbf{L}\boldsymbol{\gamma}\,, \tag{96}$$

where $\boldsymbol{\gamma}$ is the vector of unknowns, and $\mathbf{L}$ is the linear differential operator.

For periodic boundary conditions in x- and y-directions the normal modes take the form

$$\gamma = W(z) f(x,y) e^{\omega t}\,, \tag{97}$$

where γ represents any flow variables ($\mathbf{u}', p', \rho_c', \varphi'$); ω is the eigenvalue of the spatial-differential matrix $\mathbf{L}$, and $W(z)f(x,y)$ is the corresponding eigenfunction. The choices of the normal modes will depend on the initial perturbation (initial conditions).

To obtain various equilibrium solutions, for example, as shown in FIG. 25, different initialization (initial perturbation) schemes are used. The initializations (initial perturbation) applied in the simulations discussed below have a form similar to the eigenfunction of the normal mode $W(z)f(x,y)$. To satisfy the continuity condition (Eq. (92)), the initial velocity field can be described as

$$u_z = W(z) f(x,y),\ u_x = \frac{1}{a^2}\frac{\partial^2 u_z}{\partial x \partial z}, u_y = \frac{1}{a^2}\frac{\partial^2 u_z}{\partial y \partial z}\,, \tag{98}$$

where a depends on the wavelengths in x- and y-directions and satisfies

$$\left(\frac{\partial^2}{\partial x^2} + \frac{\partial^2}{\partial y^2}\right) u_z = -a^2 u_z\,. \tag{99}$$

The initial perturbation (initial condition) for a rolling pattern (2D) are taken to be:

$$u_x = 0\,, \tag{100}$$

$$u_y = -\frac{dW(z)}{dz}\frac{1}{a^2}\frac{2\pi}{L_y}\sin(2\pi y / L_y)\,, \tag{101}$$

$$u_z = W(z)\cos(2\pi x / L_y)\,, \tag{102}$$

$W(z)$ is chosen to satisfy the non-slip boundary conditions at the walls. L_y is the wavelength in the y-direction.

The initial perturbation (initial condition) for a square pattern (3D) is taken to be:

$$u_x = -\frac{dW(z)}{dz}\frac{1}{a^2}\frac{2\pi}{L_x}\sin(2\pi x / L_x)\,, \tag{103}$$

$$u_y = -\frac{dW(z)}{dz}\frac{1}{a^2}\frac{2\pi}{L_y}\sin(2\pi y / L_y)\,, \tag{104}$$

$$u_z = W(z)\left[\cos(2\pi x / L_x) + \cos(2\pi y / L_y)\right], \tag{105}$$

where $L_x = L_y$ to satisfy the condition (Eq. (99)); therefore:

$$a = 2\pi / L_y\,. \tag{106}$$

The initial perturbation (initial condition) for the hexagon pattern (3D) are taken to be:

$$u_x = -\frac{dW(z)}{dz}\frac{4\pi}{3\sqrt{3}Lc^2}\sin\left(\frac{2\pi x}{\sqrt{3}L}\right)\cos\left(\frac{2\pi y}{3L}\right), \tag{107}$$

$$u_y = -\frac{dW(z)}{dz}\frac{4\pi}{9Lc^2}\left[\cos\left(\frac{2\pi x}{\sqrt{3}L}\right) + 2\cos\left(\frac{2\pi y}{3L}\right)\right]\sin\left(\frac{2\pi y}{3L}\right), \tag{108}$$

$$u_z = \frac{1}{3}W(z)\left[2\cos\left(\frac{2\pi x}{\sqrt{3}L}\right)\cos\left(\frac{2\pi y}{3L}\right) + \cos\left(\frac{4\pi y}{3L}\right)\right], \tag{109}$$

where L is the side of the hexagon and parameter $c = \dfrac{4\pi}{3L}$.

To satisfy the wall-bounded no-slip boundary condition in the z-direction, we use a small perturbation amplitude:

$$W(z) = \left[\cos(2\pi z / H) - 1\right] \times \varepsilon\,, \tag{110}$$

where $\varepsilon = 10^{-3}$ is the perturbation magnitude, the same as in previous 2D analysis [143].

7.3 DYNAMIC MODE DECOMPOSITION

Among other methods, dynamic mode decomposition (DMD) has been used to analyze the behavior of a complex flow system. DMD is a data-driven analysis performed on experimental measurements or numerical solutions, unraveling the spatiotemporal dynamics of complex systems [218]. Schmid and colleagues first applied DMD to the stability analysis of fluid flow [219,220]. The eigenmodes from DMD are equivalent to global modes if the linearized equations are used in numerical simulations. DMD has been previously used to identify bifurcation points in complex systems such as flow in a lid-driven cavity of high Reynolds number [221], to reconstruct compressed high-dimensional data of a fluid system [222], and to extract coherent spatiotemporal structures in fluid flows for prediction and control [223,224].

To reveal the coherent structures leading to flow instability, we perform DMD on the numerical data of u_z. DMD can reconstruct the complex flow system using the linear growth approximation between snapshots of numerical solutions; DMD examines the coherent flow structures and can be used as a tool for flow field predictions and stability analysis. A continuous linear dynamical system (Eq. (96)) can be described by an analogous time-discretized system at intervals Δt:

$$\gamma_{k+1} = \mathbf{A}\gamma_k , \tag{111}$$

where

$$\mathbf{A} = \exp(\Delta t \mathbf{L}), \tag{112}$$

and γ_k is any flow variable ($\mathbf{u}', p', \rho_c', \varphi'$) at a time step k. The operator $\mathbf{L}$ is a spatial differential matrix of the continuous-time dynamical system as in Eq. (96). The solution to the discrete-time system can be expressed in terms of eigenvalues λ_j and corresponding eigenvectors ξ_j of the discrete-time mapping matrix $\mathbf{A}$:

$$\gamma_k = \sum_{j=1}^{r} \xi_j \lambda_j^k b_j = \boldsymbol{\xi}\boldsymbol{\Lambda}^k \mathbf{b}, \tag{113}$$

where $\mathbf{b}$ contains the coefficients of the perturbation (initial conditions) γ_1 in the eigenvector basis, such that $\gamma_1 = \boldsymbol{\xi}\mathbf{b}$, r is the rank of the reduced eigenmodes, $\boldsymbol{\xi}$ is the matrix whose columns are the eigenvectors ξ_j, and $\boldsymbol{\Lambda}^k$ is a diagonal matrix whose entries are the eigenvalues λ_j raised to the

power of k. The DMD algorithm provides a reduced-rank eigen-decomposition of the matrix $\mathbf{A}$ that linearly fits the trajectory γ_k for $k = 1, 2, ..., m$, minimizing the least-square error

$$\left\| \gamma_{k+1} - \mathbf{A}\gamma_k \right\|_2, \tag{114}$$

across all points for $k = 1, 2, ..., m-1$.

To obtain the discrete mapping matrix $\mathbf{A}$, we can arrange m snapshots into two data matrices:

$$\begin{aligned} \boldsymbol{\gamma} &= \begin{bmatrix} \gamma_1 & \gamma_2 & \cdots & \gamma_{m-1} \end{bmatrix} \\ \boldsymbol{\gamma}' &= \begin{bmatrix} \gamma_2 & \gamma_3 & \cdots & \gamma_m \end{bmatrix} \end{aligned}, \tag{115}$$

The data snapshots are sampled from the results of the numerical simulations, which provide the solution to the system of nonlinear equations. Therefore, the linear approximation (Eq. (111)) can be written in terms of these data matrices:

$$\boldsymbol{\gamma}' \approx \mathbf{A}\boldsymbol{\gamma}, \tag{116}$$

The matrix $\mathbf{A}$ can be obtained by taking the Moore-Penrose pseudoinverse of the data matrix $\boldsymbol{\gamma}^{\dagger}$

$$\mathbf{A} = \boldsymbol{\gamma}'\boldsymbol{\gamma}^{\dagger}. \tag{117}$$

The analysis of matrix $\mathbf{A}$ and solution prediction are described as follows:

1. Obtain singular value decomposition (SVD) of $\boldsymbol{\gamma}$:

$$\boldsymbol{\gamma} \approx \mathbf{U}\boldsymbol{\Sigma}\mathbf{V}^{H}, \tag{118}$$

where superscript H denotes the Hermitian transpose (conjugate transpose), $\mathbf{U} \in \mathbb{C}^{n \times r}$, $\boldsymbol{\Sigma} \in \mathbb{C}^{r \times r}$ and $\mathbf{V} \in \mathbb{C}^{m \times r}$. The columns of matrices $\mathbf{U}$ and $\mathbf{V}$ are orthonormal ($\mathbf{U}^H\mathbf{U} = \mathbf{I}_{r \times r}$ and $\mathbf{V}^H\mathbf{V} = \mathbf{I}_{r \times r}$, where $\mathbf{I}$ denotes identity matrix). Here n is the length of the vector γ_k (number of spatial points saved per time snapshot) and $r \le \min(n, m-1)$ is the rank of the reduced SVD approximation of $\boldsymbol{\gamma}$.

2. The matrix $\mathbf{A}$ is obtained using the pseudoinverse of $\boldsymbol{\gamma}$ from SVD. Substitution into Eq. (117) and Eq. (118) yields:

$$\mathbf{A} = \boldsymbol{\gamma}'\mathbf{V}\boldsymbol{\Sigma}^{-1}\mathbf{U}^{H}, \tag{119}$$

Additionally, it is more efficient to compute matrix $\tilde{\mathbf{A}}$, the $r \times r$ projection of the matrix $\mathbf{A}$ onto proper orthogonal decomposition (POD) modes:

$$\tilde{\mathbf{A}} = \mathbf{U}^{*}\mathbf{A}\mathbf{U} = \mathbf{U}^{*}\boldsymbol{\gamma}'\mathbf{V}\boldsymbol{\Sigma}^{-1}, \tag{120}$$

The matrix $\tilde{\mathbf{A}}$ determines a low-dimensional linear model of the dynamical system in proper orthogonal coordinates:

$$\tilde{\gamma}_{k+1} = \tilde{\mathbf{A}}\tilde{\gamma}_{k}, \tag{121}$$

The high-dimensional state can be reconstructed by

$$\gamma_{k+1} = \mathbf{U}\tilde{\gamma}_{k}. \tag{122}$$

3. Compute the eigen-decomposition of matrix $\tilde{\mathbf{A}}$

$$\tilde{\mathbf{A}}\mathbf{W} = \mathbf{W}\boldsymbol{\Lambda}, \tag{123}$$

where the columns of the matrix $\mathbf{W}$ are eigenvectors and the diagonal matrix $\boldsymbol{\Lambda}$ contains the eigenvalues.

4. Reconstruct the eigen-decomposition of the matrices $\mathbf{A}$ from $\mathbf{W}$ and $\boldsymbol{\Lambda}$. The eigenvalues of $\mathbf{A}$ are the same as the eigenvalues of $\tilde{\mathbf{A}}$ (contained in the diagonal matrix $\boldsymbol{\Lambda}$). The eigenvectors of $\mathbf{A}$ (i.e., the DMD modes) are the columns of the matrix $\boldsymbol{\xi}$ with

$$\boldsymbol{\xi} = \boldsymbol{\gamma}'\mathbf{V}\boldsymbol{\Sigma}^{-1}\mathbf{W}, \tag{124}$$

The results obtained by the DMD algorithm based on the data collected from the numerical simulations can be compared to the values calculated by linear stability analysis in the linear growth region.

With the low-rank approximation of both the eigenvalues and the eigenvectors, the projected future solution can be constructed.

$$\boldsymbol{\gamma}(t) \approx \sum_{j=1}^{r} \xi_j \exp(\omega_j t) b_j = \boldsymbol{\xi}\exp(\boldsymbol{\Omega}t)\mathbf{b}, \tag{125}$$

where $\omega_j = \ln(\lambda_j)/\Delta t$ and $\mathbf{b} = \boldsymbol{\xi}^{\dagger}\boldsymbol{\gamma}_1$, $\boldsymbol{\xi}$ is the matrix whose columns are the DMD eigenvectors ξ_j, $\boldsymbol{\Omega}$ is a diagonal matrix whose entries are the eigenvalues ω_j.

7.4 NUMERICAL METHOD

7.4.1 *Two Relaxation Time Lattice Boltzmann Method*

The TRT-LBM is applied to NSE (Eq. (78)-(79)) and the transport equation for charge density (Eq. (80)) The mesoscopic solutions of the LBM yield a discrete distribution function of velocity

$f_i(\mathbf{x},t)$ and charge density $g_i(\mathbf{x},t)$. The values of ρ, ρ_c, and momentum density $\rho\mathbf{u}$ can be evaluated by weighted sums.

$$\rho(\mathbf{x},t)=\sum_i f_i(\mathbf{x},t), \tag{126}$$

$$\rho_c(\mathbf{x},t)=\sum_i g_i(\mathbf{x},t), \tag{127}$$

$$\rho\mathbf{u}(\mathbf{x},t)=\sum_i \mathbf{c}_i f_i(\mathbf{x},t)+\frac{\mathbf{F}_e\Delta t}{2}=\sum_i \mathbf{c}_i f_i(\mathbf{x},t)-\frac{\rho_c\nabla\varphi\Delta t}{2}, \tag{128}$$

The discrete normalized velocity, $\mathbf{c}_i=(c_{ix},c_{iy})$ at position - $\mathbf{x}$ and time - t depends on a specific discretization scheme; here, we use the D2Q9 model (2 spatial dimensions and 9 discrete velocities) and D3Q27 model (3 spatial dimensions and 27 discrete velocities). The spatial discretization is uniform ($\Delta x=\Delta y=\Delta z$), and the temporal discretization - Δt. The $\mathbf{c}_i$ parameters (i=0~26) for D3Q27 are shown in **Table VII**.

The Lattice Boltzmann Equations (LBEs) for flow field and charge density are:

$$\begin{aligned} f_i(\mathbf{x}+\mathbf{c}_i\Delta t,t+\Delta t)=f_i(\mathbf{x},t)&\underbrace{-\Delta t\left[\omega^+\left(f_i^+-f_i^{eq+}\right)+\omega^-\left(f_i^--f_i^{eq-}\right)\right]}_{TRT\ collision\ operator}\\ &\underbrace{+\Delta t\left[\left(1-\frac{\omega^+\Delta t}{2}\right)F_i^+(\mathbf{x},t)+\left(1-\frac{\omega^-\Delta t}{2}\right)F_i^-(\mathbf{x},t)\right]}_{TRT\ source\ operator}, \end{aligned} \tag{129}$$

$$g_i(\mathbf{x}+\mathbf{c}_i\Delta t,t+\Delta t)=g_i(\mathbf{x},t)\underbrace{-\Delta t\left[\omega_g^+\left(g_i^+-g_i^{eq+}\right)+\omega_g^-\left(g_i^--g_i^{eq-}\right)\right]}_{TRT\ collision\ operator}, \tag{130}$$

f_i^{eq} and g_i^{eq} are the equilibrium distributions for flow field and charges respectively, which are given by

$$f_i^{eq}(\mathbf{x},t)=w_i\rho\left(1+\frac{\mathbf{u}\bullet\mathbf{c}_i}{c_s^2}+\frac{(\mathbf{u}\bullet\mathbf{c}_i)^2}{2c_s^4}-\frac{\mathbf{u}\bullet\mathbf{u}}{2c_s^2}\right), \tag{131}$$

$$g_i^{eq}(\mathbf{x},t)=w_i\rho_c\left(1+\frac{(\mathbf{u}-\mu_b\nabla\varphi)\bullet\mathbf{c}_i}{c_s^2}+\frac{\left[(\mathbf{u}-\mu_b\nabla\varphi)\bullet\mathbf{c}_i\right]^2}{2c_s^4}-\frac{(\mathbf{u}-\mu_b\nabla\varphi)\bullet(\mathbf{u}-\mu_b\nabla\varphi)}{2c_s^2}\right), \tag{132}$$

F_i is the forcing term accounting for the electric force

$$F_i=w_i\left(\frac{\mathbf{c}_i-\mathbf{u}}{c_s^2}+\frac{(\mathbf{c}_i\bullet\mathbf{u})\mathbf{c}_i}{c_s^4}\right)\bullet\mathbf{F}_e, \tag{133}$$

where $c_s^2 = P/\rho = (1/3)(\Delta x/\Delta t)^2$ is the speed of sound [225]; $\tau^{\pm} = 1/\omega^{\pm}$ and $\tau_g^{\pm} = 1/\omega_g^{\pm}$ are the times at which the distribution functions relax to equilibrium, and w_i is the weight for the velocity component $\mathbf{c}_i$ shown in **Table VI** for 2D and **Table VII** for 3D.

Table VI. Velocity set and the corresponding weights for D2Q9 model

i	$\mathbf{c}_i$	w_i
0	(0,0)	4/9
1	(1,0)	1/9
2	(0,1)	1/9
3	(-1,0)	1/9
4	(0,-1)	1/9
5	(1,1)	1/36
6	(-1,1)	1/36
7	(-1,-1)	1/36
8	(1,-1)	1/36

Table VII. Velocity set and weights in D3Q27 model

i	$\mathbf{c}_i$	w_i
0	(0,0,0)	8/27
1	(1,0,0)	2/27
2	(-1,0,0)	2/27
3	(0,1,0)	2/27
4	(0,-1,0)	2/27
5	(0,0,1)	2/27
6	(0,0,-1)	2/27
7	(1,1, 0)	1/54
8	(-1,-1,0)	1/54
9	(1,0,1)	1/54

10	(-1,0,-1)	1/54
11	(0,1,1)	1/54
12	(0,-1,-1)	1/54
13	(1,-1,0)	1/54
14	(-1,1,0)	1/54
15	(1,0,-1)	1/54
16	(-1,0,1)	1/54
17	(0,1,-1)	1/54
18	(0,-1,1)	1/54
19	(1,1,1)	1/216
20	(-1,-1,-1)	1/216
21	(1,1,-1)	1/216
22	(-1,-1,1)	1/216
23	(1,-1,1)	1/216
24	(-1,1,-1)	1/216
25	(-1,1,1)	1/216
26	(1,-1,-1)	1/216

The TRT approach has been previously used to model the collision operators [207-209,212,213] and the momentum source operator [226,227]. Alternatively, to SRT operators, TRT is more robust for EC problems, as it provides additional relaxation parameter, improving the numerical stability [225]. The terms specified in the TRT collision operators and the source operator are

$$f_i^+ = \frac{f_i + f_{\bar{i}}}{2},\ f_i^- = \frac{f_i - f_{\bar{i}}}{2}, f_i^{eq+} = \frac{f_i^{eq} + f_{\bar{i}}^{eq}}{2}, f_i^{eq-} = \frac{f_i^{eq} - f_{\bar{i}}^{eq}}{2} \tag{134}$$

$$g_i^+ = \frac{g_i + g_{\bar{i}}}{2},\ g_i^- = \frac{g_i - g_{\bar{i}}}{2}, g_i^{eq+} = \frac{g_i^{eq} + g_{\bar{i}}^{eq}}{2}, g_i^{eq-} = \frac{g_i^{eq} - g_{\bar{i}}^{eq}}{2} \tag{135}$$

$$F_i^{\pm} = \frac{F_i \pm F_{\bar{i}}}{2}. \tag{136}$$

Subscript $\bar{i}$ denotes the velocity component opposite to i, such that $\mathbf{c}_i = -\mathbf{c}_{\bar{i}}$. Relaxation parameters ω^+, ω_g^- are determined by

$$v = c_s^2\left(\frac{1}{\omega^+} - \frac{\Delta t}{2}\right),\ D_c = c_s^2\left(\frac{1}{\omega_g^-} - \frac{\Delta t}{2}\right). \tag{137}$$

ω^- and ω_g^+ need to satisfy

$$\Lambda = \left(\frac{1}{\omega^+\Delta t} - \frac{1}{2}\right)\left(\frac{1}{\omega^-\Delta t} - \frac{1}{2}\right),\ \Lambda_g = \left(\frac{1}{\omega_g^+\Delta t} - \frac{1}{2}\right)\left(\frac{1}{\omega_g^-\Delta t} - \frac{1}{2}\right), \tag{138}$$

where Λ and Λ_g are free factors used to control the algorithm stability [225]. Here, $\Lambda = 1/12$ and $\Lambda_g = 10^{-6}$; the large difference accounts for the mismatch between the neutral molecule and charge diffusivity.

7.4.2 *Fast Poisson Solver*

The Poisson equation (Eq.(81)) is solved by a fast Poisson solver using a 3D FFT algorithm. The discretized grid function can be written as:

$$[D_x^2 + D_y^2 + D_z^2]\varphi_{x,y,z} = s_{x,y,z}, \tag{139}$$

where D_x^2, D_y^2 and D_z^2 are 2nd order derivatives operators in x - y - z coordinates; $s_{x,y,z}$ - source term representing space charge effect. Fourier spectral method is used in the x and y-direction and 2nd order finite difference scheme in the z-direction. In x and y-direction, the FFT algorithm is used to implement the standard Discrete Fourier transform (DFT).

$$DFT_x\left[\varphi_{x,y,z}\right] = \sum_{x=1}^{NX}\varphi_{x,y,z}\exp\left[-i\frac{2\pi(k_x-1)}{NX}(x-1)\right],\ 1 \le k_x \le NX, \tag{140}$$

$$DFT_y\left[\varphi_{x,y,z}\right] = \sum_{y=1}^{NY}\varphi_{x,y,z}\exp\left[-i\frac{2\pi(k_y-1)}{NY}(y-1)\right],\ 1 \le k_y \le NY. \tag{141}$$

where k_x, k_x are the wavenumbers and NX, NY are the number of grid points in the x and y-direction. The 2nd derivative in the x and y-direction can be calculated in the Fourier domain

$$DFT_x\left[D_x^2\varphi_{x,y,z}\right] = DFT_x\left[\frac{\partial^2\varphi_{x,y,z}}{\partial x^2}\right] = -k_x^2 DFT_x\left[\varphi_{x,y,z}\right], \tag{142}$$

$$DFT_y\left[D_y^2\varphi_{x,y,z}\right] = DFT_y\left[\frac{\partial^2\varphi_{x,y,z}}{\partial y^2}\right] = -k_y^2 DFT_y\left[\varphi_{x,y,z}\right]. \tag{143}$$

Fourier transform in the z-direction uses an odd extension of the domain to satisfy the Dirichlet boundary conditions.

$$\varphi^{ext}_{x,y,z_{ext}} = \left[0, \varphi_{x,y,1}, \varphi_{x,y,2}, \cdots, \varphi_{x,y,NZ}, 0, -\varphi_{x,y,NZ}, \cdots, \varphi_{x,y,1}\right], \tag{144}$$

$$s^{ext}_{x,y,z_{ext}} = \left[0, s_{x,y,1}, s_{x,y,2}, \cdots, s_{x,y,NZ}, 0, -s_{x,y,NZ}, \cdots, s_{x,y,1}\right], \tag{145}$$

where NZ is the number of grid points in the z-direction. The size of the extended matrices is $NX \times NY \times NE$, where $NE = 2NZ + 2$; the z_{ext} is the extended z indices, ranging from 1 to NE. From the definition of DFT (Eq. (140)-(141)),

we have:

$$DFT_z\left[\varphi^s_{x,y,z+1}\right] = \exp\left(ik_z \Delta z\right) DFT_z\left[\varphi_{x,y,z}\right], \tag{146}$$

where φ^s is a periodically shifted vector by Δz of φ in z-direction. Applying a central differencing operator in z_{ext} direction gives:

$$DFT_{z_{ext}}\left[D^2_{z_{ext}} \varphi^{ext}_{x,y,z_{ext}}\right] = \frac{\exp\left(ik_{z_{ext}} \Delta z\right) + \exp\left(-ik_{z_{ext}} \Delta z\right) - 2}{\Delta z^2} DFT_{z_{ext}}\left[\varphi^{ext}_{x,y,z_{ext}}\right] = \frac{-4\sin^2\left(k_{z_{ext}} \Delta z/2\right)}{\Delta z^2} DFT_{z_{ext}}\left[\varphi^{ext}_{x,y,z_{ext}}\right]. \tag{147}$$

Therefore, the Fourier transform of Eq. (139) is

$$-\left(k_x^2 + k_y^2 + \frac{4\sin^2\left(k_{z_{ext}} \Delta z/2\right)}{\Delta z^2}\right) DFT_{x,y,z_{ext}}\left[\varphi^{ext}_{k_x,k_y,k_{z_{ext}}}\right] = DFT_{x,y,z_{ext}}\left[s^{ext}_{k_x,k_y,k_{z_{ext}}}\right]. \tag{148}$$

The Inverse Fast Fourier Transform (IFFT) algorithm transforms $DFT_{x,y,z_{ext}}\left[\varphi^{ext}_{k_x,k_y,k_{z_{ext}}}\right]$ into the spatial domain. Then, the electric potential in the original domain is obtained by retaining the first half ($1 \le z \le NZ$) of the extended solution matrix.

7.5 NUMERICAL SETUP

The numerical method is implemented in C++ using CUDA GPU computing. The number of threads in the x-direction in each GPU block is equal to NX; the number of GPU blocks in the y-direction is equal to NY. FFT and IFFT operations are performed using the cuFFT library. All variables are computed with double precision to reduce truncation errors. The numerical method was shown to be 2nd order accurate in space. To reduce computational cost while maintaining accuracy, the grid of $NX = 122$, $NZ = 100$ is used in 2D simulations. The wall-normal direction is

represented by y-direction in 2D analysis and z-direction in 3D analysis; cross-flow is applied in the x-direction. Macroscopic and mesoscopic boundary conditions are specified in **Table VIII**.

Table VIII. Boundary conditions used in the numerical simulations.

Boundary	Macro-variables Conditions	Meso-variables Conditions
x, y direction boundaries	Periodic	Periodic
Upper wall	$\mathbf{u}=0$, $\varphi=0$ and $\nabla\rho_c=0$	Bounce-back for f_i [59,207,213,215,225] Bounce-back for g_i [59,207,213,215,225]
Lower wall	$\mathbf{u}=0$, $\varphi=\varphi_0$, $\rho_c=\rho_0$	Bounce-back for f_i $\frac{\partial g_i}{\partial z}=0$

The full-way bounce-back is used for Dirichlet boundary conditions for fluid flow [87,88,228]. The bounce-back method for Neumann boundary conditions applied to impermeable solid walls can introduce spurious boundary layer because of the diagonal velocity-weights [59,215]. Nevertheless, The Neumann boundary condition for g_i is an outflow boundary condition for charge density transport [87,88,225]. The choice of small Λ_g can improve accuracy because of the horizontal boundaries [59,215].

7.6 NUMERICAL RESULTS

7.6.1 *Non-dimensional analysis and solution for hydrostatic state*

Governing equations yield four non-dimensional parameters that describe the system's state [81,86-90].

$$M=\frac{(\varepsilon/\rho)^{1/2}}{\mu_b},\quad T=\frac{\varepsilon\Delta\varphi_0}{\mu\mu_b},\quad C=\frac{\rho_0 H^2}{\varepsilon\Delta\varphi_0},\quad Fe=\frac{\mu_b\Delta\varphi_0}{D_e}, \tag{149}$$

where H is the distance between the electrodes (distance between the two infinite plates), ρ_0 is the injected charge density at the anode, and $\Delta\varphi_0$ is the voltage difference applied to the electrodes. The physical interpretation of these parameters are as follows: M - the ratio between hydrodynamic mobility and the ionic mobility; T - the ratio between electric force to the viscous force; C - the charge injection level; and Fe - the reciprocal of the charge diffusivity coefficient [81,86]. For

electroconvection system considered in this chapter, these four non-dimensional parameters can characterize the flow. Velocity is not explicitly included; however, for the scenarios with strong advection, a different set of scaling parameters can be more attractive [143,174].

FIG. 18 shows that our hydrostatic solutions for electric field and charge density agree well with the model of Luo et al. [87,88] and the analytical solution [32,140]. The analytical solution is based on a reduced set of equations for the electric field in one-dimensional coordinates.

$$\rho_c = \rho_a \left(y + y_a \right)^{-1/2}, \tag{150}$$

$$E_z = \frac{2\rho_a}{\varepsilon} \left(z + z_a \right)^{1/2}, \tag{151}$$

where ρ_a and z_a are parameters that depend on the boundary conditions and geometry. For the hydrostatic state, parameter C dominates the system [81,86].

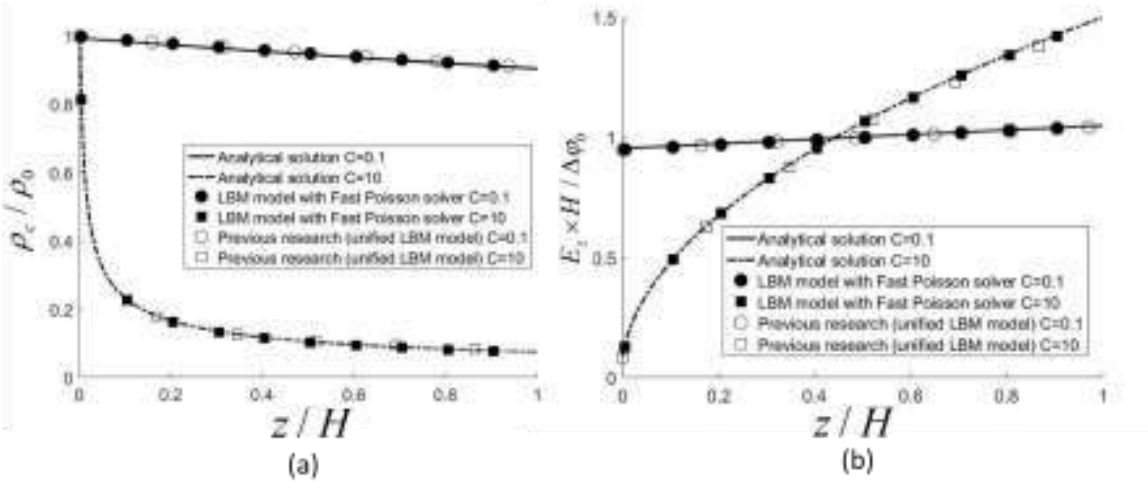

FIG. 18. Hydrostatic solution comparison of the TRT LBM and Fast Poisson solver, unified SRT LBM [87], and the analytical solution [32,140] for $C = 0.1$ and $C = 10$, $Fe = 4000$. (a) Electric field and (b) charge density;

Table IX shows the dimensional parameters used for the analytical solution and the L_2 norm error between numerical results and analytical solutions. The numerical errors are lower than reported for the unified SRT LBM simulation (e_{L_2} =0.0076) [87]. The numerical results at the hydrostatic base state acts as a validation of our numerical method and the initial condition before the initial perturbation of the EC flow.

Table IX. Dimensional parameters for the analytical model and L_2 norm errors e_{L_2} for weak ion injection $C = 0.1$ and strong ion injection $C = 10$.

C	0.1	10
$\rho_a (Coulomb/m^{5/2})$	0.218	0.75
$y_a (m)$	4.8	0.003
e_{L_2} of E_y	0.0031	0.0030
e_{L_2} of ρ_c	0.0035	0.0031

7.6.2 *Electroconvection instability in 2D without cross-flow*

To model electro-convective instability, the steady-state hydrostatic solution is perturbed using waveform functions that satisfy the boundary conditions and continuity equation:

$$\begin{aligned} u_x &= L_x \sin\left(2\pi y / L_y\right)\sin(2\pi x / L_x)\times 10^{-3} \\ u_z &= L_z\left[\cos\left(2\pi z / L_z\right)-1\right]\cos(2\pi x / L_x)\times 10^{-3} \end{aligned}, \tag{152}$$

The physical domain size is $Lx = 1.22m$ and $Lz = 1.00m$ limits the perturbation wavenumber to $\lambda_x = 2\pi / L_x \approx 5.15(1/m)$ -- the most unstable mode under the condition, where C=10, $M = 10$, $Fe = 4000$ [88]. The electric Nusselt number $Ne_0 = I_1 / I_0$ acts as a criterion of flow stability, where I_1 is the cathode current at a specific condition, I_0 is the cathode current for the hydrostatic solution [74]. For cases where EC vortices exist, $Ne_0 > 1$. For a strong ion injection, the EC stability largely depends on T; so, in the following analysis, T is varied, while other parameters are held constant: $C = 10$, $M = 10$ and $Fe = 4000$.

For $T \geq T_c$ and the perturbation is given by Eq. (152), the flow becomes unstable developing EC vortices which are maintained by an electric force acting on the ionized fluid -- a combination of applied electric field and the space charge effect. The space charge effect can alter the applied electric field in the area of high charge density [174]. FIG. 19 (a) shows the formation of counter-rotating vortices; the charge density contour plotted with streamlines. In an upward fluid motion, the local charge transport is enhanced as indicated by the higher charge density in the center of the domain. In downward flow motion, the charge transport decreases, see the darker blue in the edges of the domain. FIG. 19 (b) shows the x-directional velocity contour. High x-velocity regions are

located near the top and bottom walls; the flow is symmetric, which indicates that the steady-state solution has the same wavelength in x and y directions as the perturbation equations (Eq. (152)).

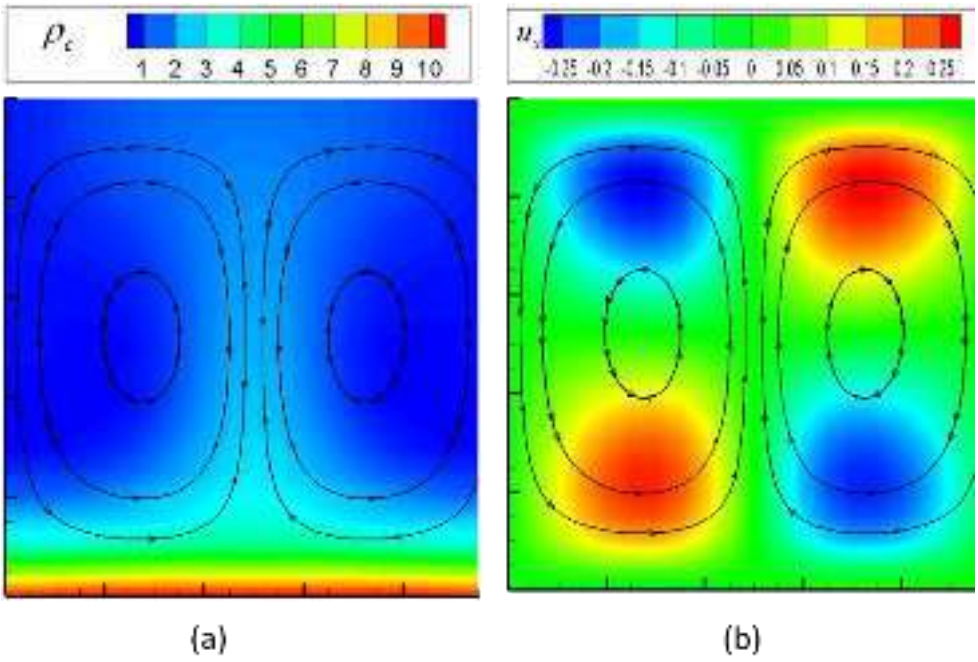

FIG. 19. Charge density and u_x contours for EHD convection with vortices.

FIG. 20 (a) shows the EC flow stability analysis, demonstrated by Ne_0 as a function of T. When $T < T_c$ the perturbation does not trigger the flow instability, the perturbed flow reverses to the hydrostatic state. If T is decreased after the EC vortices are formed, they are maintained until $T = T_f$ when the system returns to the hydrostatic state. The model predicts the bifurcation points at $T_c = 163.4$ and $T_f = 108.7$ agreeing Luo et al. [88] ($T_c = 163.1$, $T_f = 108.7$), the linear stability analysis [81,88] ($T_c = 163.5$), and the finite volume method [85] ($T_f = 108.2$) under the same conditions. Neither numerical model nor linear stability analysis agrees with the experimental data. The proposed segregated TRT-LBM approach is consistent with the previous research; however, it does not modify governing equations by introducing artificial terms needed for numerical stability and yields fast convergence of the elliptical Poisson equation enabled for the FFT approach.

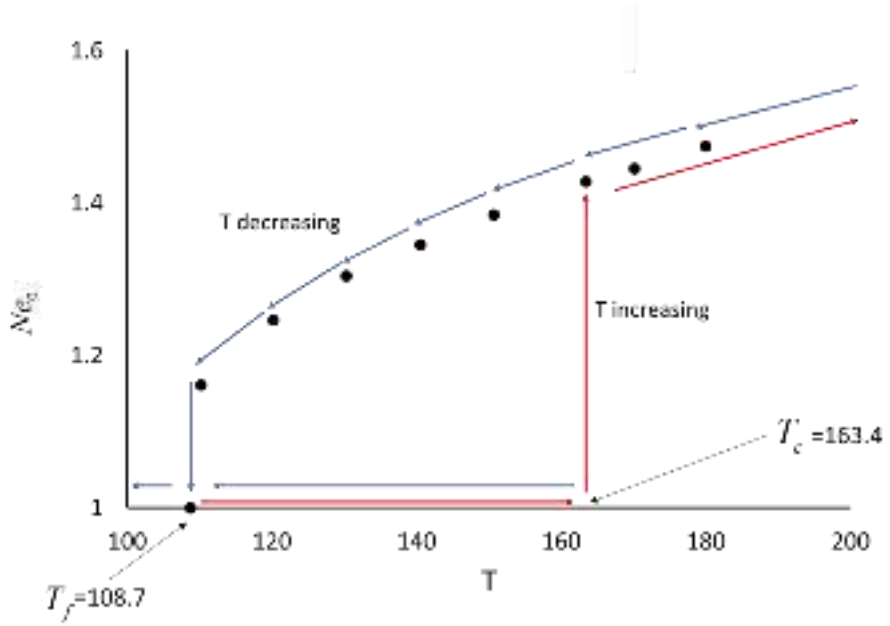

FIG. 20. Electric Nusselt number Ne_0 depends on electric Rayleigh number T

7.6.3 *Electroconvection instability in 2D with a cross-flow*

In this section, we discuss the effect of cross-flow on the 2D EC vortices. Two types of cross-flows are investigated, i.e., the Couette flow and Poiseuille flow. The Couette cross-flow is added to the simulation with EC vortices by assigning constant velocity of the upper wall. To model the Poiseuille flow, a body force in the x-direction is added. FIG. 21 shows the charge density and x-direction velocity for Couette cross-flow ($u^*_{wall} = 0.8$) and Poiseuille cross-flow ($u^*_{center} = 0.8$), where the asterisk represents non-dimensionalized by drift velocity u_{drift}. The Couette cross-flow stretches the vortices in the direction of the bulk flow and may eliminate one of the two vortices. In a Poiseuille cross-flow, the vortex pair becomes separated; the vortices are pushed toward the opposite walls. For strong cross-flow, both vortices in the pair are eliminated, and $I=I_0$, $Ne=1$(see FIG. 24). The EC contribution to the flow field is negligible at higher values of shear stress (higher velocity), and the flow field is the same as the applied cross-flow.

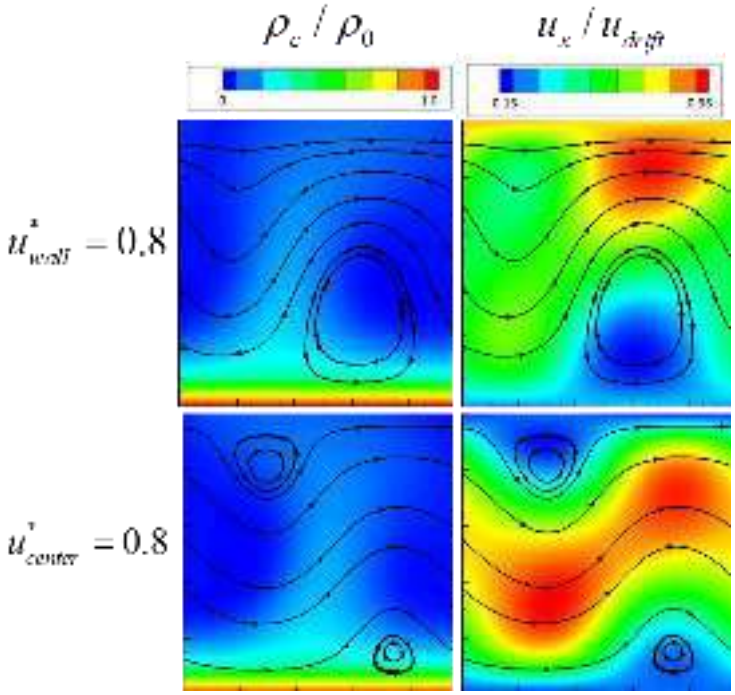

FIG. 21. Charge density and x-direction velocity contour of the EC with cross-flow. Top: Couette flow with $u^*_{wall} = 0.8$; one of the two vortices is suppressed. Bottom: Poiseuille flow with $u^*_{center} = 0.8$; two vortices are suppressed and pushed towards the walls.

FIG. 22 shows the extended stability analysis of EC without cross-flow [142] by introducing (a) finite velocity of the upper wall (cathode) and (b) a uniform body force for pressure driven flow $F_p = dp/dx$. For a constant T, Ne decreases as u_{wall} or $u_{center} = \frac{1}{2\mu}\left(\frac{H}{2}\right)^2 F_p$ increases. The applied shear stress stabilizes the EC flow.

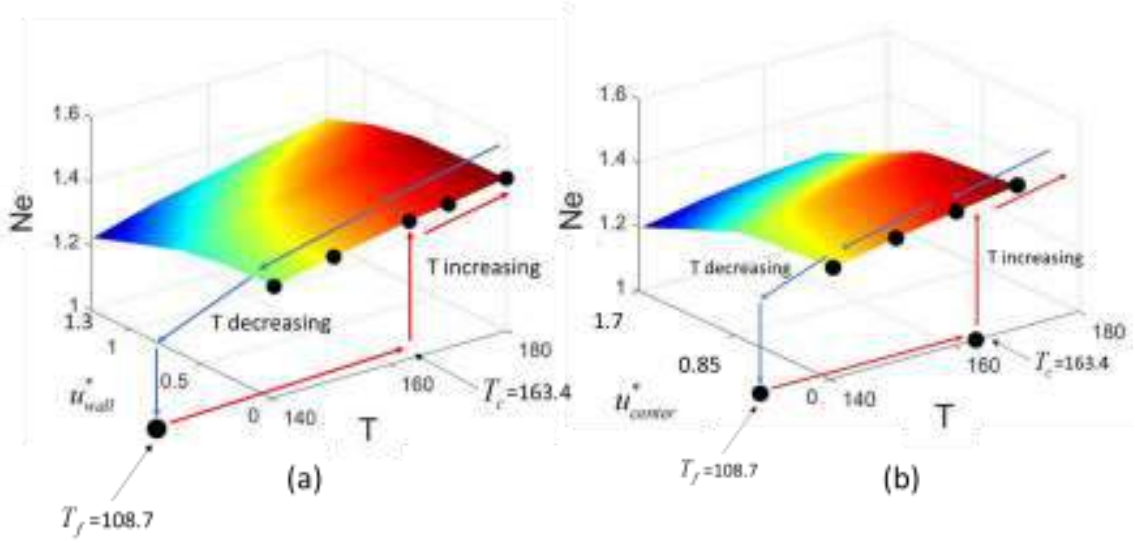

FIG. 22. Electric Nusselt number depends on the electric Rayleigh number T and applied velocity of the upper wall u^*_{wall} for Couette type cross-flow or u^*_{center} for Poiseuille type cross-flow.

FIG. 23 shows the dependency of Ne on non-dimensional parameter Y. For varying values of T, the solutions lie on the same curve of Ne normalized by $Ne_{Y\infty}$ (Ne at $Y \to \infty$, solutions without cross-flow [142]) suggesting that the EC stability with cross-flow can be characterized by a single non-dimensional parameter Y, which is inversely proportional to $\boldsymbol{\tau}$.

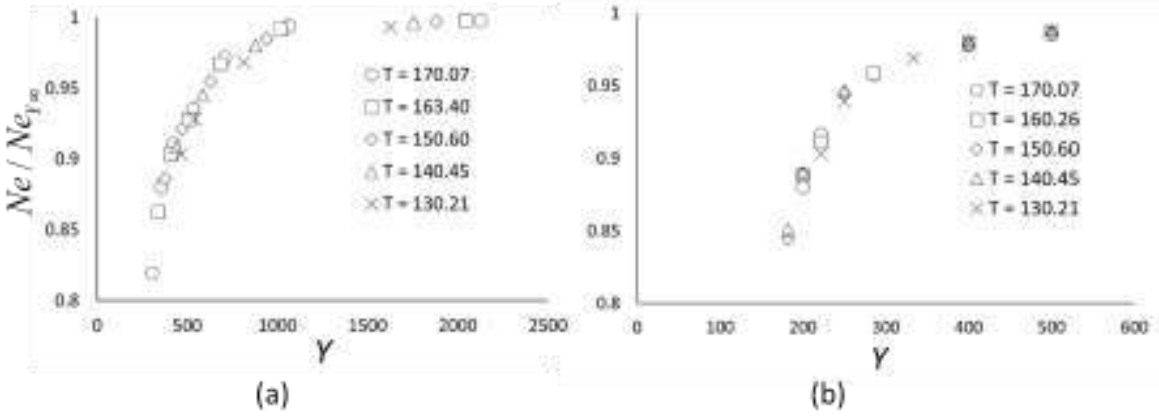

FIG. 23. Electric Nusselt number depends on the non-dimensional parameter Y. (a) Couette type cross-flow is applied. (b) Poiseuille type cross-flow is applied.

FIG. 24 shows $Ne = f(Y)$ for $C = 10$, $M = 10$, $T = 170.07$, and $Fe = 4000$ for Couette and Poiseuille cross-flow. A hysteresis loop with subcritical bifurcation is observed; the bifurcation thresholds are $Y_c = 625.25$, $Y_f = 297.32$ for Couette flow and $Y_c = 218.58$, $Y_f = 159.36$ for

Poiseuille flow. Similar to stability parameter *T* for the hydrostatic case (FIG. 22), for $Y < Y_c$, the system does not yield the EC instability, returning to the unperturbed state ($I = I_0$ and *Ne*=1). If Y decreases after the EC vortices are formed, Ne decreases nonlinearly, until $Y = Y_f$, then the EC vortices are suppressed; the Coulombic forces do not influence the flow.

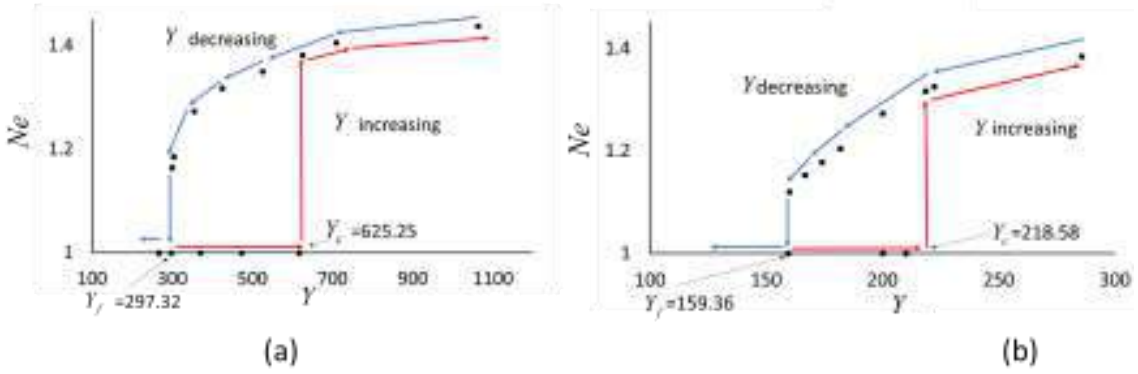

FIG. 24. ElectricNusselt number *Ne* versus *Y*. Bifurcation thresholds are: (a) Couette cross-flow $Y_c = 625.25$ and $Y_f = 297.32$; (b) Poiseuille cross-flow $Y_f = 159.36$ and $Y_f = 218.58$.

7.6.4 *Electroconvection instability in 3D: General Picture*

In this section, we investigate the 3D EC phenomenon. The TRT LBM approach is used to solve the transport equations for fluid flow and charge density, coupled to a fast Poisson solver for electric potential [142,143]. The solver is extended to 3D for the differential equations (Eq. (78)-(80)) and performed with certain initial perturbations (initial conditions) (Eq. (100)-(102) for rolling pattern, Eq. (103)-(105) for square pattern, and Eq. (106)-(109) for hexagon pattern and mixed patterns). The equilibrium state was obtained when the flow became stable. The numerical code is in SI units, and the physical constants are determined by the non-dimensional parameters. The numerical method is implemented in C++ using CUDA GPU computing. FFT and IFFT operations are performed using the cuFFT library. All variables are computed with double precision to reduce truncation errors. The numerical method was shown to be 2nd order accurate in space. The equilibrium patterns of EC flow fields without cross-flow were obtained using the initial conditions described in section 7.2. The resulting patterns depend on the non-dimensional parameter *T* and the domain size, the latter which determines the wavelengths of the vortices. FIG. 25(a-e) shows the equilibrium states of u_z at $z = H/2$. The values $C = 10$, $M = 10$, and $Fe = 4000$ are held

constant for each condition. The simulations were carried out to $T = 170$ for u_z plotted in FIG. 25(a, c-e), and to $T = 833$ for u_z in FIG. 25(b). The domain sizes and initial perturbation (initial condition) for the simulations plotted in FIG. 25(a) and (b) are the same (Eq. (100)-(102)), and therefore u_z in FIG. 25(b) is the harmonic of u_z in FIG. 25(a) that develops at the high value of *T*. For cases given in FIG. 25(c-e), different domain sizes with hexagon pattern initial perturbation (Eq. (106)-(109)) are used. When sufficiently strong Couette type cross-flow in the x-direction is applied to the 3D structures, the transition to 2D streamwise rolling patterns occurs for all initial perturbations scenarios FIG. 25(f-j).

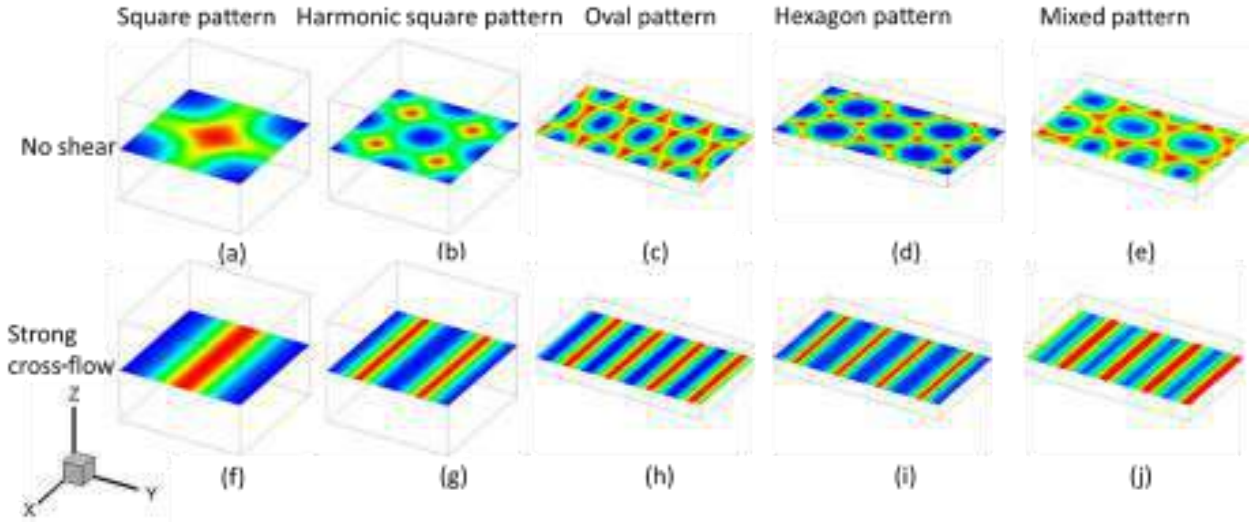

FIG. 25. Contours of u_z at $z = H/2$ at equilibrium states (a-e) without cross-flow and (f-j) with cross-flow sufficient for pattern transition. For different electric Rayleigh numbers, domain sizes, and initial perturbations (initial conditions), square patterns, oval patterns, hexagon patterns, and mixed patterns are established. Strong cross-flow in the x-direction is applied to the equilibrium states (a-e), resulting in the 3D transition to 2D streamwise vortices.

To study the mechanism for this transition dynamics to streamwise vortices, we consider the simplest scenario, i.e., the case where the equilibrium state is a one period square pattern (FIG. 25(a)). Further generalization of transition for other patterns can be a subject of future work. The physical domain used in the simulation is given by $L_x = L_y = 1.22m$ and $H = 1m$; this limits the wavenumber to $k_x = k_y = 2\pi / L_x \approx 5.15(1/m)$, and yields the most unstable mode at $C = 10, M = 10$, and $Fe = 4000$ [81,88]. The electric Nusselt number, $Ne = I / I_0$, serves as a flow stability criteria, where I is the cathode current for a given solution and I_0 is the cathode current for the base state solution without EC vortices [74,88]; thus, $Ne > 1$ when EC vortices exist. The transition to chaotic

flow at higher values of forcing term will be considered in the next chapter. Since for the EC problem with the cross-flow, the stability largely depends on Y [143], in this analysis, Y is varied, while other non-dimensional parameters are held constant at $T = 170$, $C = 10$, $M = 10$, and $Fe = 4000$.

7.6.5 *Perturbation of the hydrostatic base state without cross-flow*

An initial perturbation was applied to the hydrostatic base state after the one-dimensional electric property profiles were established as shown in FIG. 18. FIG. 26 shows that for $T > T_c$, the 2D perturbation (Eq. (100)-(102)) leads to the development of a rolling pattern with flow only in y and z directions, while the 3D square perturbation (Eq. (103)-(105)) leads to a square pattern with velocities in all three directions. FIG. 27 shows the evolution of the maximum u_z for the first 20s after the perturbation is applied. Both the rolling pattern and square pattern have the same linear growth rate (~0.224s^{-1}), which agrees with the linear stability analysis [81] and the unified SRT LBM numerical model [88]. After about 20s from the initial perturbation, the growth rate curves diverge. Although the maximum u_z is greater for the square pattern, the charge transport (based on $Ne = I / I_0$) for rolling patterns is greater, as shown later in FIG. 40 and FIG. 41. We use the dimensional quantities in this section, but all variables can be non-dimensionalized accordingly.

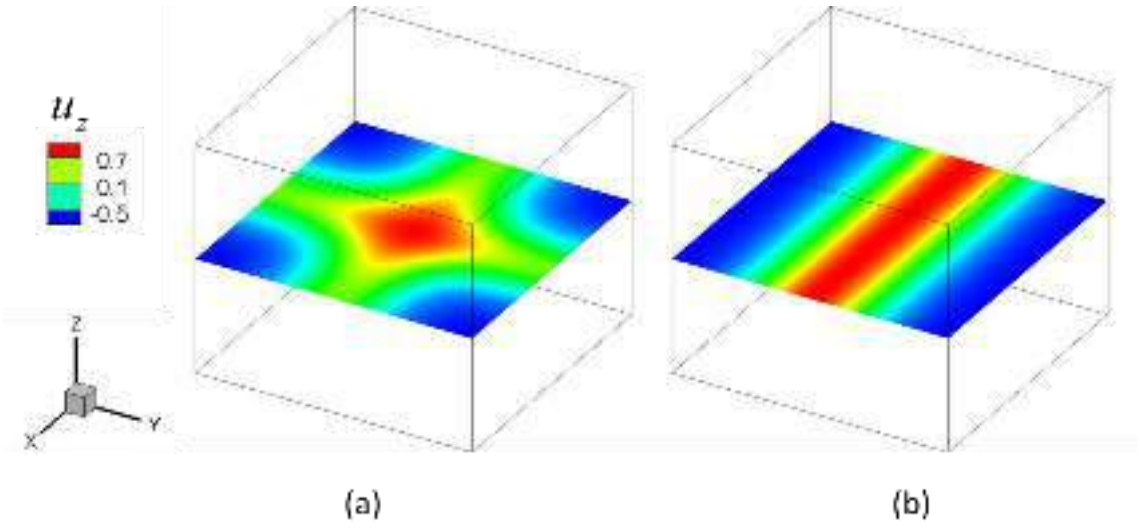

FIG. 26. Contours of u_z at z=H/2 for initial perturbation by (a) square pattern and (b) rolling pattern with $T = 170$, $C = 10$, $M = 10$, and $Fe = 4000$.

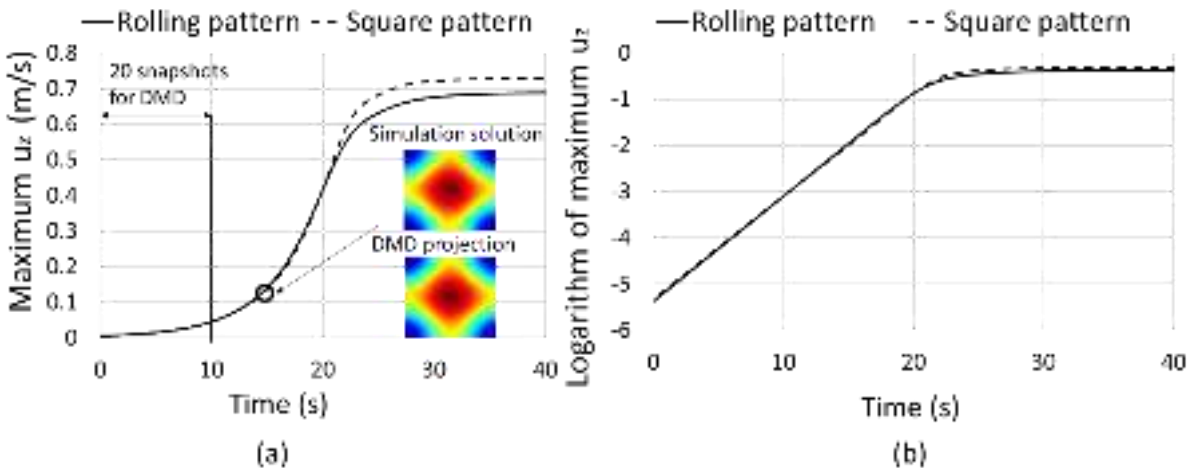

FIG. 27. Time evolution of maximum u_z for the rolling pattern and square pattern in (a) linear scale and (b) logarithmic scale. Both patterns have similar growth rates (~0.224 s^{-1}) in the linear growth region (t=0~20s). The DMD algorithm based solutions in the interval t=0-10s projects the state at 15s.

DMD is performed based on the numerical data of the square pattern perturbation case from 0-10s at intervals of $\Delta t = 0.5s$. FIG. 28 shows the eigenvalues λ of the discrete-time mapping matrix $\mathbf{A}$ as in Eq. (112) and the logarithmic mapping of the eigenvalues ω of the matrix $\mathbf{L}$ as in Eq. (96). The eigenvalues λ are shown in relationship to the unit circle (dashed line); most of the values are inside the circle and therefore, represent stable dynamic modes. Three unstable modes (solid dots) with positive growth rates are found. The imaginary parts of these unstable modes are zero ($\lambda_i = 0$); these modes do not oscillate.

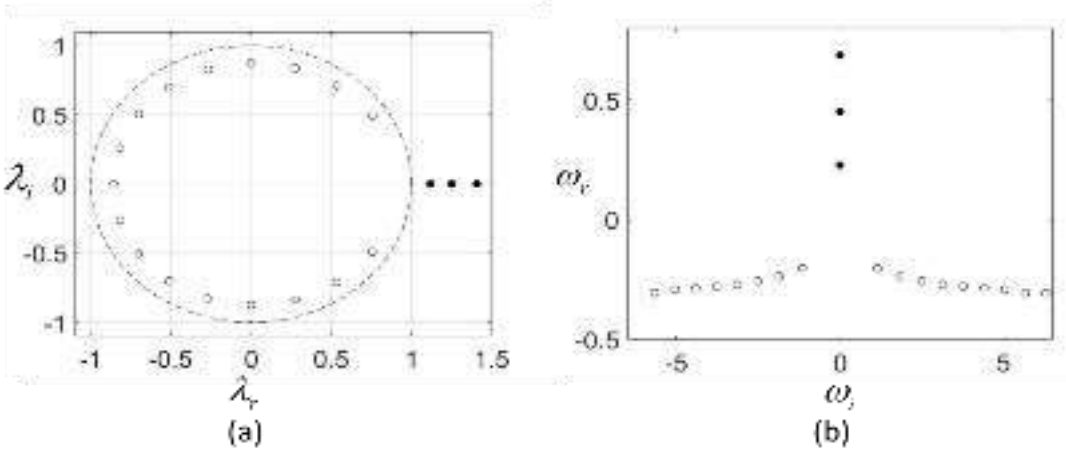

FIG. 28. (a) Eigenvalues of the discrete-time mapping matrix $\mathbf{A}$ and (b) logarithmic mapping of eigenvalues of $\mathbf{L}$. The eigenvalues outside the unit circle, whose logarithmic value has a real component ω_r greater than 0, represent the unstable dynamic modes. The logarithmic mapping of the eigenvalue $\mathbf{L}$ indicates the growth rate of each dynamic mode.

The three unstable modes with positive growth rates dominate the flow pattern. FIG. 29 shows the eigenvectors of these three modes, along with the simulation result at 10s, plotted on the plane $z = H/2$. The plots show square patterns with different wavelengths and the phase shifts. Although the mode $\omega_r = 0.227$ has a lower growth rate, it contains >99% of the energy of the perturbation (its initial amplitude of b=1.826 is much greater than that of the others). The overall growth rate (~0.224s^{-1}) from FIG. 27 is very close to the growth rate of this dynamic mode shown in FIG. 29(c). The comparison of the dynamic modes FIG. 29(a-c) and simulation solution FIG. 29(d) verifies that the dynamic mode $\omega_r = 0.227$ dominates the flow system. The growth rates of rolling and square patterns are very close to each other, which was also observed in the previous investigation[88].

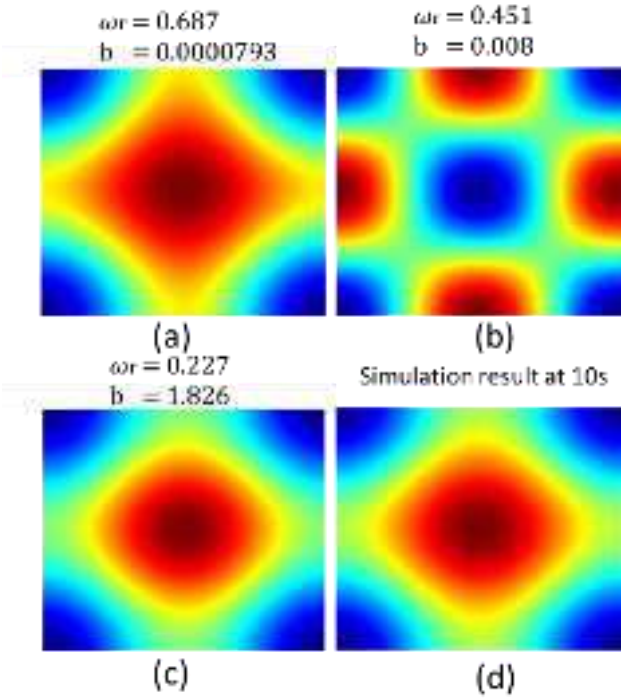

FIG. 29. Unstable dynamic modes visualized by u_z at $z = H/2$. The dynamic mode $\omega_r = 0.227$ (c) perturbation has the greatest of projection (b=1.826) on this eigenmode, and therefore, it contains most of the energy of the system. The growth rate of this mode $\omega_r = 0.227$ is close to the general growth rate of the entire system (~0.224) from FIG. 27.

7.6.6 *Perturbation of the hydrostatic base state including a cross-flow*

In this section, we investigate the EC problem with an initial perturbation applied to the hydrostatic base state after a cross-flow field has been added in the x-direction. Cases for two cross-flows are studied. The square pattern initial perturbation is used (Eq. (103)-(105)). The first is a Couette flow, which is obtained by applying the speed u_{wall} to the upper wall while holding the bottom wall fixed. The second is a Poiseuille flow, which is driven by a body force representing the pressure drop - F_p, so the center speed is $u_{center}= \frac{1}{2\mu}\left(\frac{H}{2}\right)^2 F_p$. FIG. 30 shows the evolution of maximum u_z and *Ne* for both cases. For the first 20s after the initial perturbation (Eq. (103)-(105)), the growth is linear, and the growth rate of ~0.224s^{-1} is the same for all solutions. The growth rate is the same with and without cross-flow because the cross-flow does not affect the streamwise vortices, and as it is shown in FIG. 27 the streamwise vortices grow at the same rate as the 3D square patterns. After about 20s, the growth rates diverge to reach different equilibrium states for different cross-flows scenarios and perturbation schemes. With weak cross-flow (u_{wall}=0.4m/s for Couette flow, u_{center}=0.42m/s for Poiseuille flow), the final solutions exhibit oblique 3D vortex structures; both transverse and regular longitudinal rolls coexist. The maximum values of u_z in these oblique 3D vortices are greater than for cases with rolling patterns. For strong cross-flow (u_{wall}=1.0m/s for Couette type and u_{center}=0.96m/s for Poiseuille type), the systems develop directly into a longitudinal rolling pattern regardless of the initial perturbation; i.e., transverse rolls do not exist even when the initial perturbation has the square pattern. The maximum u_z of the streamwise vortices in the cross-flow case is the same as the 2D rolling vortices without cross-flow, as shown in FIG. 27; in other words, streamwise vortices are superimposed onto the base state cross-flow solution. With respect to the final steady state (oblique 3D or 2D rolling vortices), the solutions with and without cross-flow bifurcate at u_{wall}=0.55m/s for Couette type and u_{center}=0.70m/s for Poiseuille flow at about 20s. Before reaching an equilibrium state, the cases with the moderate cross-flow exhibit an intermediate state where the maximum u_z can be greater than the final longitudinal rolling pattern case (u_z=0.688m/s) or even the square pattern case with transverse and longitudinal rolls (u_z=0.728m/s). After reaching the peak, in each case, u_z decreases to an equilibrium solution corresponding to the cross-flow strength. For the intermediate cross-flow cases, the systems first develop oblique 3D structures similar to the weak cross-flow cases, and

then transition to longitudinal rolling vortices (for Couette flow at u_{wall}=0.56 and 0.6m/s; for Poiseuille flow at u_{center}=0.71,0.74,0.85 m/s), as shown in FIG. 31. For strong cross-flow (for Couette flow at u_{wall}=1.0m/s; for Poiseuille flow at u_{center}=0.95m/s) the flows develop directly into longitudinal 2D rolling patterns.

Unlike the evolution of the maximum u_z, *Ne* always increases during the transition from 3D to 2D vortices (FIG. 30 c-d). However, for cross-flow below bifurcation occurs (the cross-flow is not strong enough to suppress the 3D structures), the steady-state value of *Ne* for the stronger cross-flow can be lower than in the weaker cross-flow. If the cross-flow suppresses the transverse structures, the system develops into a longitudinal rolling pattern with a constant *Ne*=1.41, which is independent of the strength or type of cross-flow. As with the u_z analysis, the charge transport by the longitudinal vortices is superimposed onto the cross-flow regardless of the flow profile.

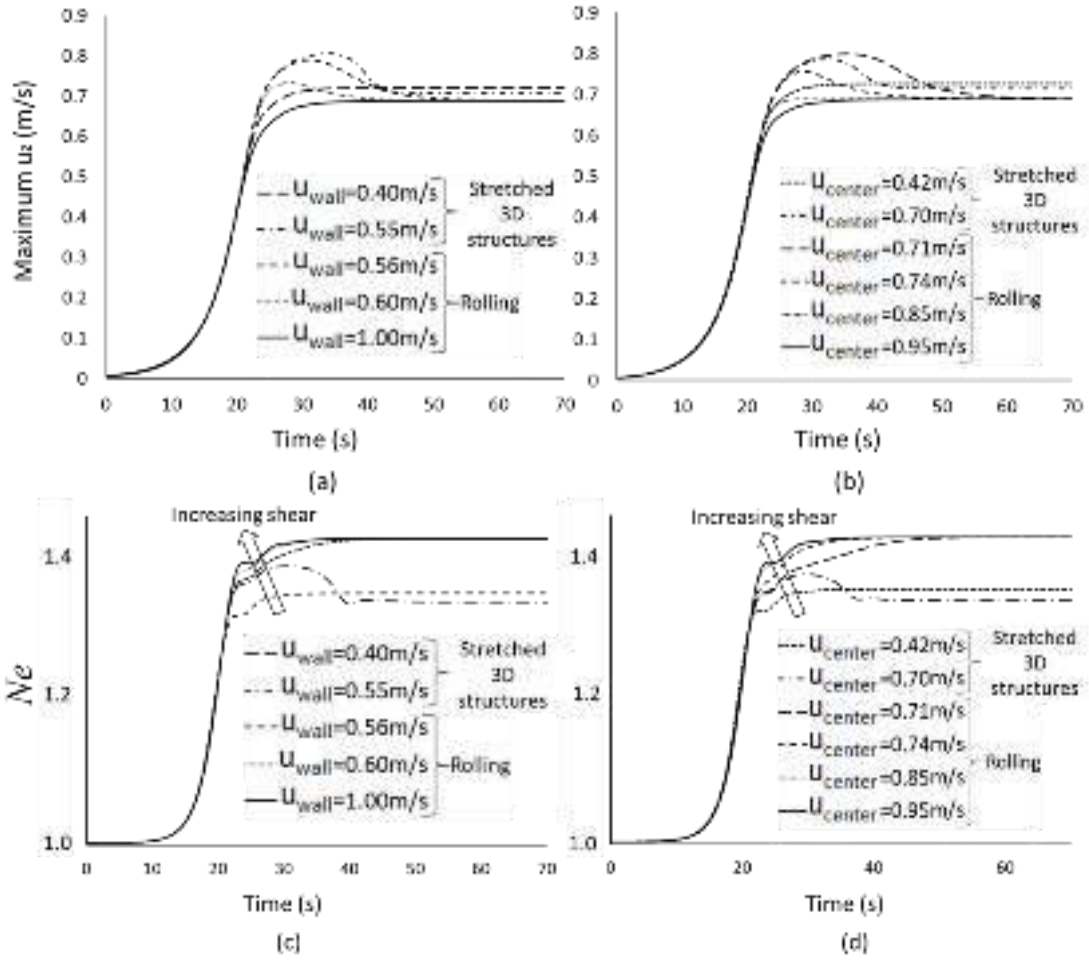

FIG. 30. Time evolution of maximum u_z and *Ne* for (a, c) Couette cross-flow and (b, d) Poiseuille cross-flow. Maximum u_z have similar growth rates (~0.224s^{-1}) in the linear growth region (t=0~20s). The square pattern initial perturbation scheme (Eq. (103)-(105)) is used. For strong cross-flow, the systems develop into longitudinal rolling patterns. For the weak cross-flow, the systems develop into oblique 3D structures with both transverse and longitudinal structures.

FIG. 31 shows u_z at $z=H/2$ and t=30s for (a) Couette cross-flow with u_{wall}=0.56m/s and (b) Poiseuille cross-flow with u_{center}=0.71m/s; this time is when the maximum u_z reaches its peak value in the non-linear growth region. Both plots exhibit a dominating longitudinal vortex pattern, i.e., aligned with the cross-flow in the x-direction. The transverse structures are suppressed due to the interaction of the vortex's x-velocity components with the cross-flow; these interactions are most profound near the walls where x-velocity components of the initial 3D vortices are the greatest. For example, in Couette flow the clockwise vortex deforms at some oblique angle as in x-direction (streamwise) flow accelerates the upper region of the 3D structure and retards the

bottom region in the transverse direction (relative to the mean velocity). This is reversed in the case of the counterclockwise rotating vortex. Eventually, these transverse structures become suppressed, and the systems develop into longitudinal rolling patterns [143]. Since the longitudinal rolling pattern is two dimensional in y and z-directions, it does not interact with the bulk cross-flow. For the Poiseuille flow, the mechanism is slightly different; however, the interactions of the vortex structure and the bulk flow exist only in the x-direction; thus y-z structures are not affected by the cross-flow; therefore, the streamwise vortices cannot be suppressed by any type of the cross-flow.

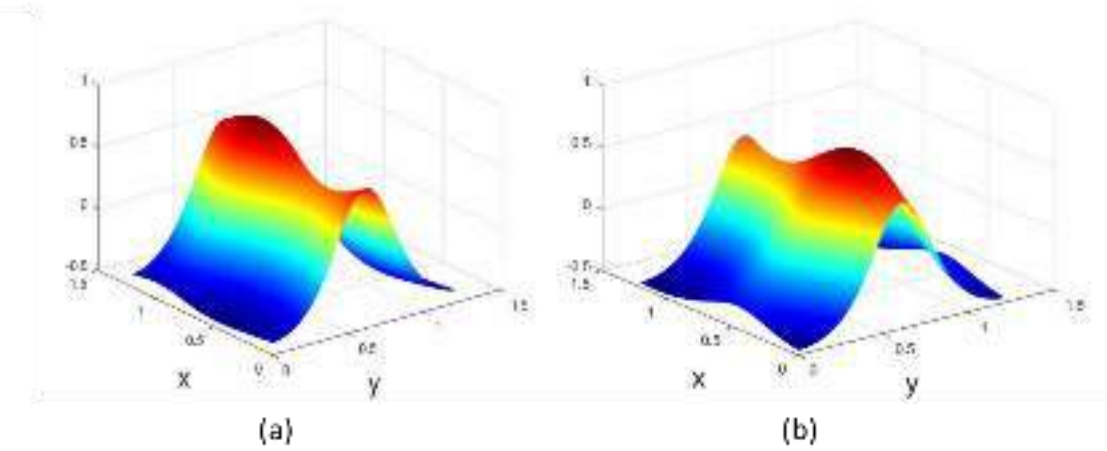

FIG. 31. Contours of u_z for z=$H/2$, t=30s: (a) Couette cross-flow $u_{wall}=0.56m/s$; (b) Poiseuille cross-flow $u_{center}=0.71m/s$.

DMD analysis of the EC vortices in the cross-flow was performed using the numerical data of u_z in linear growth region (0-28s for Couette type and 0-25s for Poiseuille type) at time intervals of $\Delta t=0.5s$. Additional unstable dynamic modes exist in the oblique 3D pattern compared to the rolling pattern. FIG. 32 shows the λ for Couette cross-flow at (a) u_{wall}=0.55m/s and (c) u_{wall}=0.56m/s. Similarly, FIG. 33 shows λ for Poiseuille cross-flow: (a) u_{center}=0.70m/s and (c) u_{center}=0.71m/s. As in the u_z evolution in hydrostatic base states without cross-flow (FIG. 27-FIG. 29), a perturbation in cross-flow arouses several unstable dynamic modes. Most of the dynamic modes are similar in corresponding flows, resulting in a similar flow field up to the bifurcation point. However, in both cases, the lower velocity flow contains additional unstable modes, i.e., m_1 and the conjugate pair $m_2-\bar{m}_2$ in Couette cross-flow, and mode $m_3-\bar{m}_3$ in Poiseuille cross-

flow. These additional unstable dynamic modes correspond to 3D features changing the stability of the system. They appear in nonlinear growth region up to the bifurcation point where the curves of weak and strong cross-flow start to diverge, see FIG. 30(a-b).

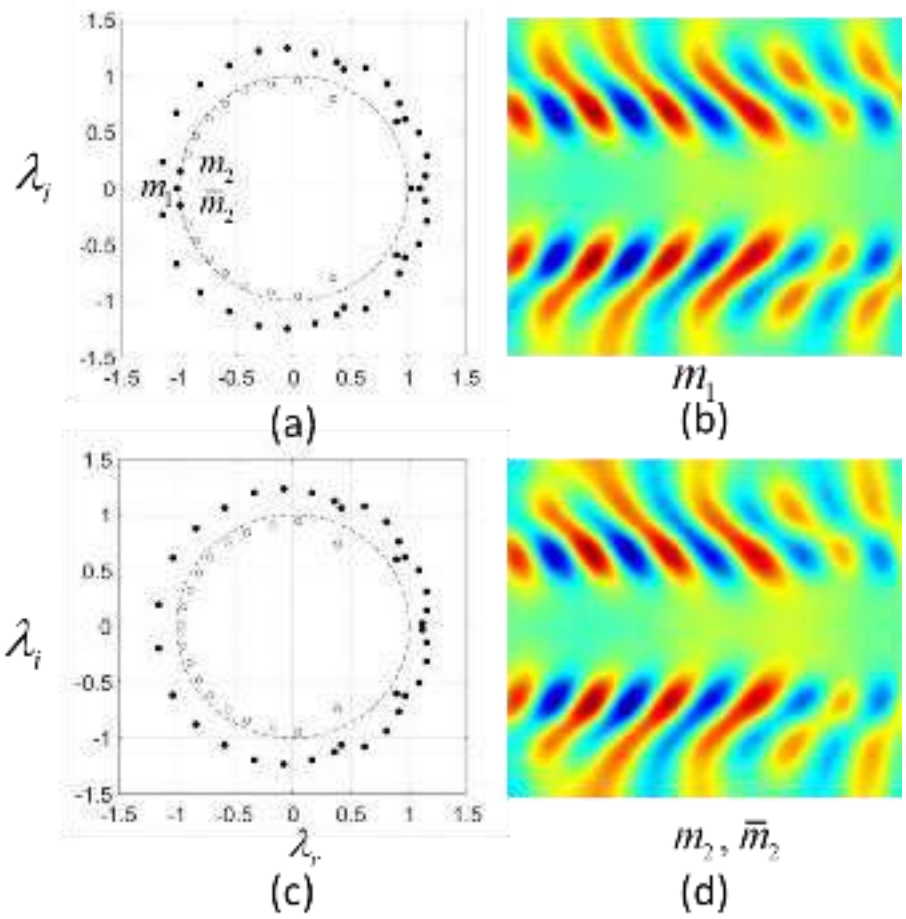

FIG. 32. Eigenvalues λ_i for u_z in linear growth region (0-28s) for Couette cross-flow ((a) u_{wall}=0.55m/s and (c) u_{wall}=0.56m/s). Three additional unstable dynamic modes in u_{wall}=0.55m/s case change the equilibrium solution from a rolling pattern to oblique 3D structures. The corresponding eigenvectors sliced at $z = H/2$ are shown in (b) mode m_1 and (d) mode m_2 and $\bar{m}_2$.

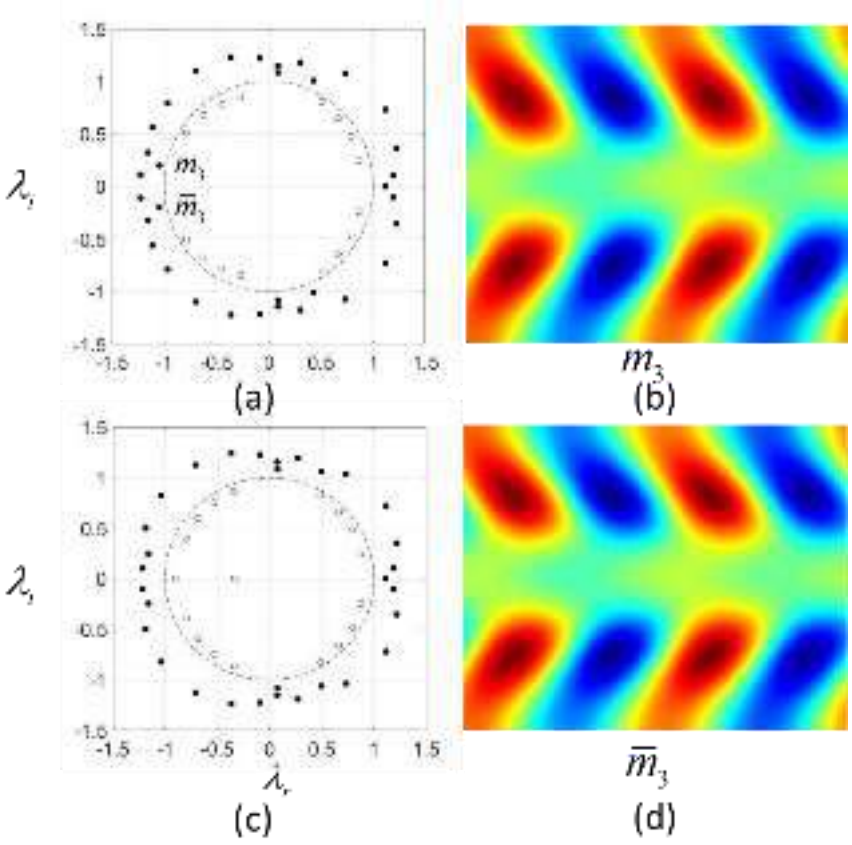

FIG. 33. Eigenvalues λ_i for u_z in linear growth region (0-25s) for Poiseuille cross-flow ((a) u_{center}=0.70m/s and (c) u_{center}=0.71 m/s). An additional pair of conjugate unstable dynamic modes in u_{center}=0.70m/s case change the equilibrium solution from a rolling pattern to an oblique 3D structure pattern. The corresponding eigenvectors sliced at $z = H/2$ are shown in (b) mode m_3 and (d) mode.

7.6.7 *Pattern transition after cross-flow application*

In this section, the transitions from 3D to 2D patterns were studied by applying the cross-flow to already developed 3D vortex structures (a single period square pattern). With weak cross-flow, the systems exhibit oblique 3D vortex structures (oblique transverse and regular longitudinal structures coexist). For strong cross-flow, the flows develop into a longitudinal rolling pattern, i.e., transverse structures are fully suppressed. FIG. 34 shows the time evolution of maximum u_z in Couette cross-flow. For small u_{wall} and, therefore, weak applied shear stress (e.g., u_{wall}=0.60m/s), the maximum u_z decreases to an equilibrium value somewhat greater than that of the rolling pattern flow (u_{wall} =0.688m/s). Interestingly, with a further increase in u_{wall} (e.g., u_{wall}=0.80m/s), the equilibrium value for u_z may decrease below the value of the rolling pattern. And with even further

increasing u_{wall} (e.g., u_{wall}=0.96m/s), the equilibrium solution develops an oblique 3D structure with maximum u_z that is greater than that of the rolling pattern. However, at u_{wall} = 0.97m/s, a bifurcation occurs, and the steady-state solution has only 2D streamwise vortices. The transition from 3D to the 2D rolling pattern is marked by a significant increase in u_z to a value greater than the original square pattern, before finally decaying to the same value as for the rolling pattern. This significant increase is a result of kinetic energy transfer from modes with 3D structures to the dominating 2D structures. For larger u_{wall}, the peak u_z value is reduced and the time required for pattern transition also decreases. When the applied u_{wall} is sufficiently large (e.g., u_{wall}>1.70m/s), the maximum value of u_z never reaches the levels above that of the rolling pattern.

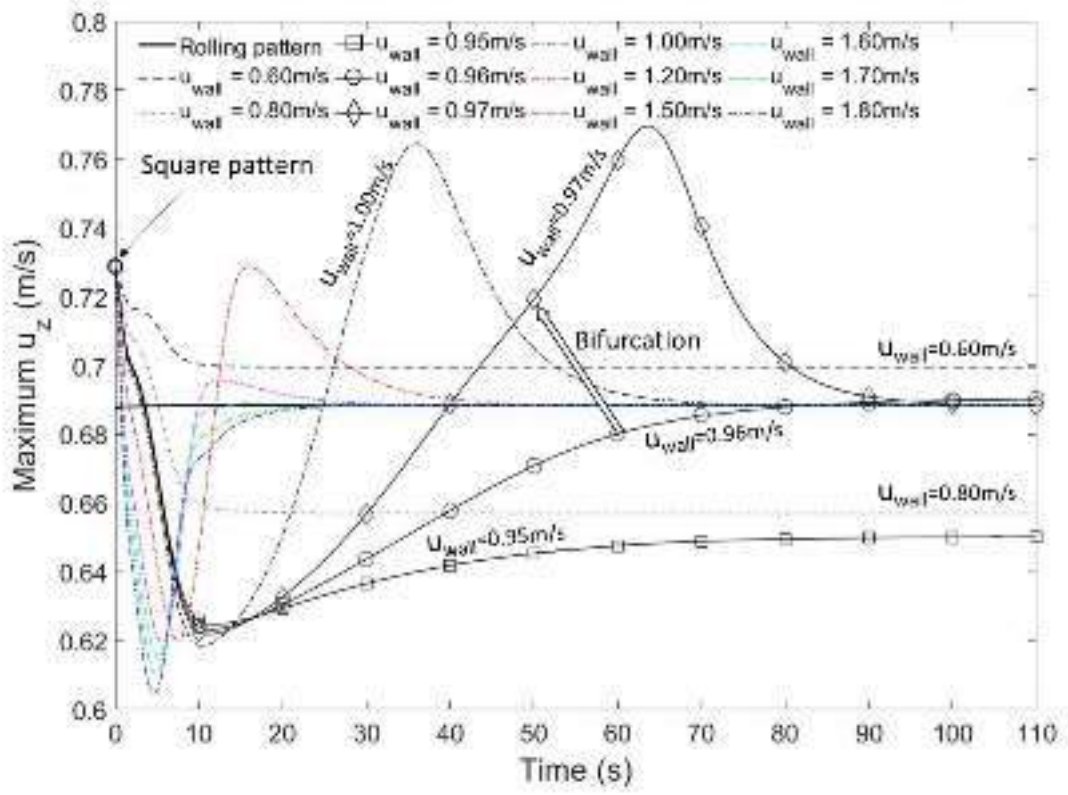

FIG. 34. Time evolution of maximum u_z after a finite velocity is applied to the upper wall. For small u_{wall}, the maximum u_z decreases and reaches a new equilibrium state where oblique 3D structures are observed. For large u_{wall}, the maximum u_z decreases down to the rolling pattern where longitudinal rolls dominate, after a nonlinear transition. Bifurcation happens at u_{wall}=0.97m/s.

Similar behavior is observed when the cross-flow is a Poiseuille flow. FIG. 35 shows the time evolution of maximum u_z due to an applied uniform body force F_p, used to obtain the Poiseuille

flow. For small u_{center} and, therefore, weak applied shear stress (e.g., u_{center}=0.85m/s), the maximum u_z decays to an equilibrium state with a value greater than that of the rolling pattern (0.688m/s). With increasing F_p (e.g., u_{center}=0.98m/s), the equilibrium solution develops an oblique 3D structure as the maximum u_z slightly increases after decaying to a minimum value. With u_{center} up to 0.98m/s, both oblique transverse and longitudinal structures coexist. However, at u_{center} =0.99m/s, a bifurcation occurs, and the steady-state solution has only 2D streamwise vortices. The transition from 3D to the rolling pattern is marked by a significant increase in u_z to a value greater than the original square pattern, before ultimately decaying into the rolling pattern. For large F_p, the peak value of u_z is reduced, and the time required for pattern transition also decreases. When the applied F_p is sufficiently large (e.g., u_{center}=1.38m/s), the maximum value of u_z does not reach the levels above that of the rolling pattern.

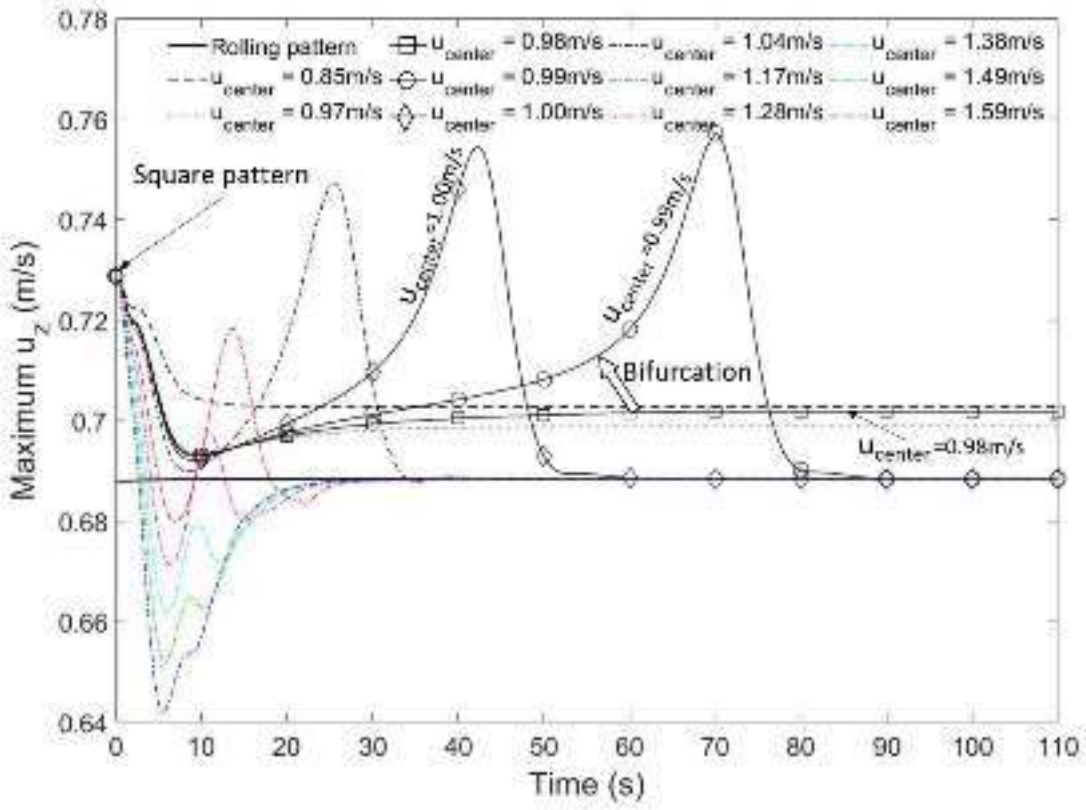

FIG. 35. Time evolution of maximum u_z after a uniform body force is applied to the flow field. For small u_{center}, the maximum u_z decreases and reaches a new equilibrium state where oblique 3D structures are observed. For large u_{center}, the maximum u_z decreases to the rolling pattern values where longitudinal rolls dominate, after a nonlinear transition. Bifurcation occurs at u_{center}=0.99m/s.

To analyze the coherent structures leading to the suppression of the instabilities, DMD analysis of the EC in the cross-flow was performed using the numerical results from square-rolling transition regions at intervals of $\Delta t = 1.0s$. FIG. 36 shows λ_i for the weak cross-flow cases (a) u_{wall}=0.96m/s for Couette cross-flow and (c) u_{center}=0.97m/s for Poiseuille cross-flow. The corresponding unstable eigenvectors correspond to the non-decaying coherent flow structures. In addition to the dominant dynamic modes (m_4 and m_{10}) corresponding to the rolling pattern, unstable dynamic modes (m_5-m_9 and m_{11}-m_{12}) exist; these are associated with the oblique 3D features. The unstable modes are similar to the ones obtained from the linear growth of perturbation in the cross-flow scenario, see FIG. 32 and FIG. 33, which can lead to changes in the stability of the entire system. FIG. 37 shows for strong cross-flow cases (u_{wall}=0.97m/s for Couette and u_{center}=1.04m/s for Poiseuille cross-flows). Only a single unstable eigenvalue is observed which corresponds to rolling

pattern eigenvectors m_4 or m_{10} in FIG. 36 (rolling pattern). The DMD analysis is consistent with the numerical simulation; the EC flow transforms from 3D square to 2D rolling with the strong cross-flow.

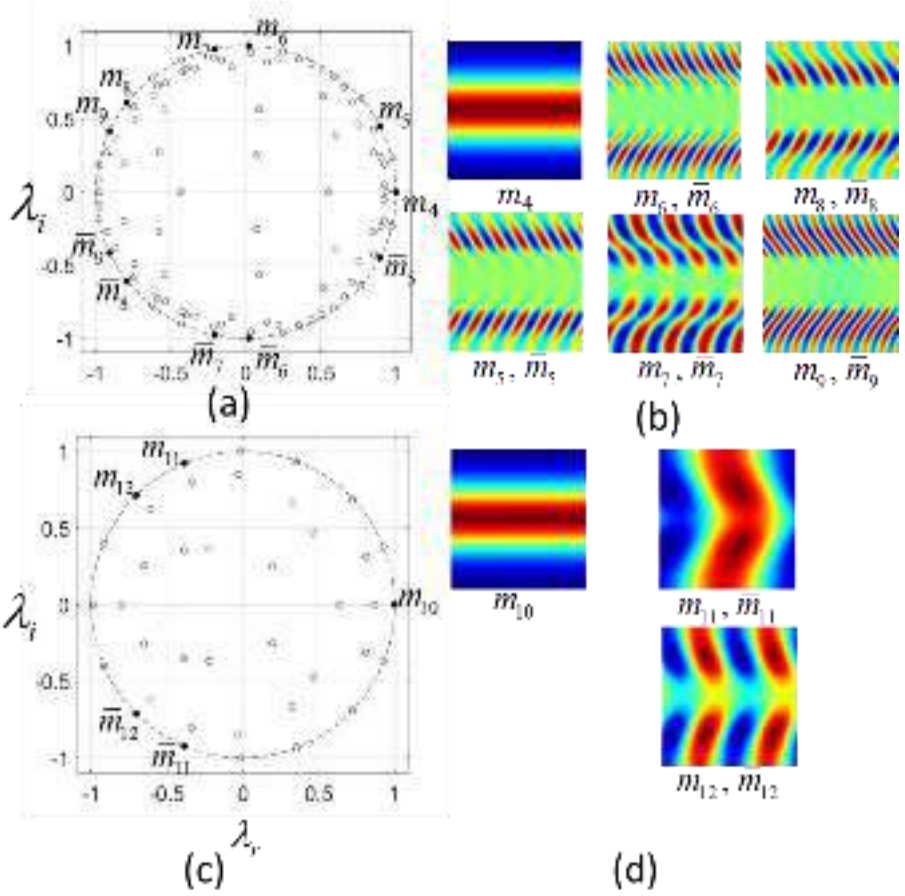

FIG. 36. Eigenvalues λ_i for u_z in transition region for Couette type cross-flow (a) u_{wall}=0.96m/s and Poiseuille type cross-flow (c) u_{center}=0.97m/s. Unstable dynamic modes change the equilibrium solution from a square pattern to oblique 3D structures. The corresponding eigenvectors sliced at $z = H/2$ are shown in (b) mode $m_4 - \bar{m}_9$ and (d) mode $m_{10} - \bar{m}_{12}$.

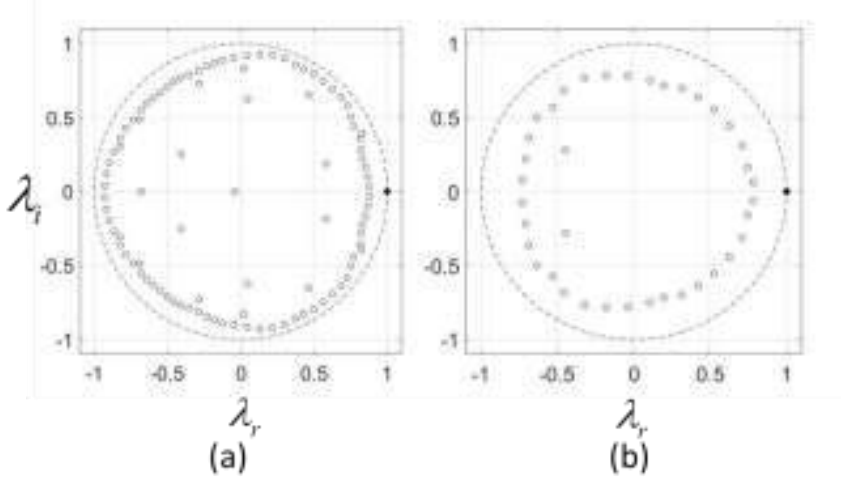

FIG. 37. Eigenvalues λ_i for u_z in transition region for Couette type cross-flow (a) u_{wall}=0.97m/s and Poiseuille type cross-flow (c) u_{center}=1.04m/s. The remaining unstable dynamic modes change the equilibrium solution from a square pattern to rolling structures.

FIG. 38 shows the u_z at $z = H/2$ for Couette cross-flow and Poiseuille cross-flow when the maximum value reaches the valley (t=10s, u_{wall}=0.97m/s and t=8s, u_{center}=1.04m/s) and peak (t=63s, u_{wall}=0.97m/s and t=25s for u_{center}=1.04m/s), as shown in FIG. 34 and FIG. 35. For both types of cross-flow, the u_z patterns are similar. When the maximum u_z is at its valley, oblique 3D structures are more pronounced, while a rolling pattern dominates the flow for high maximum u_z . The transition can be interpreted as energy transfer from one dominant mode to another. Further analysis of the nonlinear transition behavior can be performed by solving for a reduced nonlinear system such as given by coupled Ginzburg-Landau equations for transverse and longitudinal rolls, similar to the analysis of the effects of cross-flow on RBC [122-124].

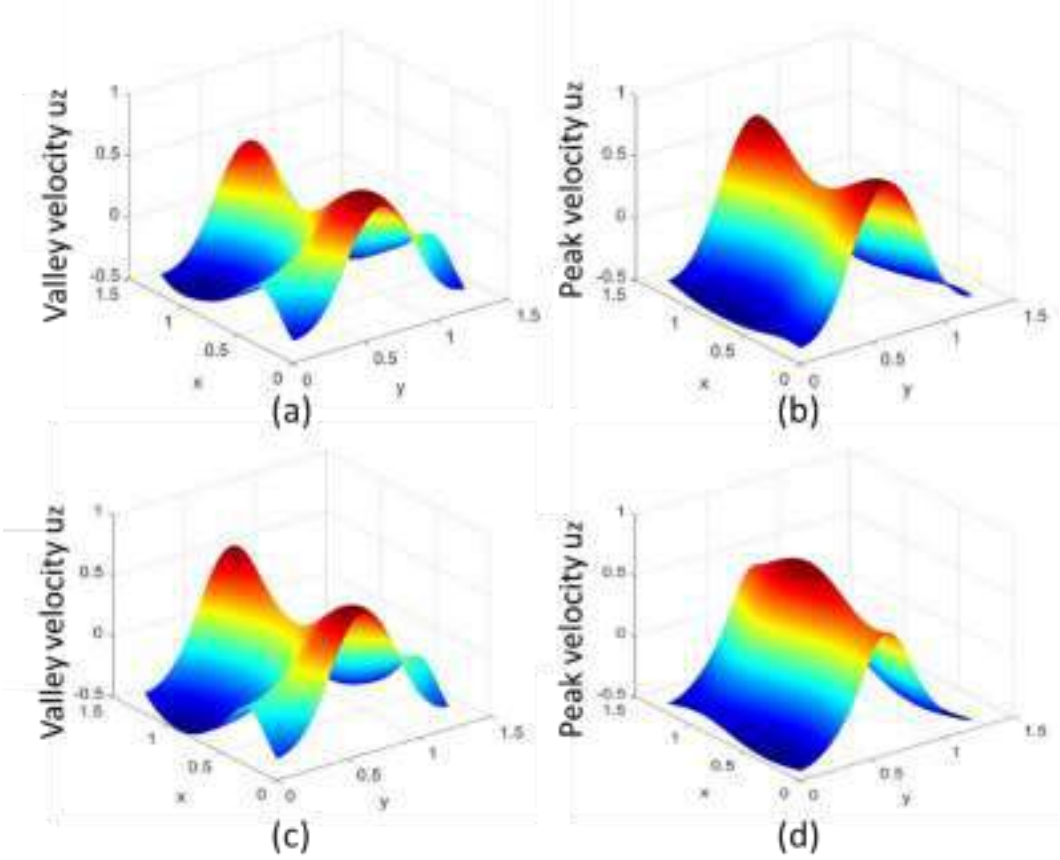

FIG. 38. Contours of valley and peak velocity u_z for (a-b) Couette cross-flow (u_{wall}=0.97m/s) and (c-d) Poiseuille cross-flow (u_{center}=1.04m/s)

FIG. 39 shows the iso-surfaces of charge density during the transition from square to a rolling pattern. Square patterns of charge density are observed at the conditions without cross-flow, as shown in FIG. 39(a). When a weak cross-flow is applied, the iso-surfaces are obliquely stretched in the x-direction, as in FIG. 39(b-c). For strong cross-flow the transverse patterns are suppressed, the rolling pattern is observed, as in FIG. 39(d). The iso-surface of charge density is identical for all strong cross-flows, and for the rolling pattern perturbation without cross-flow.

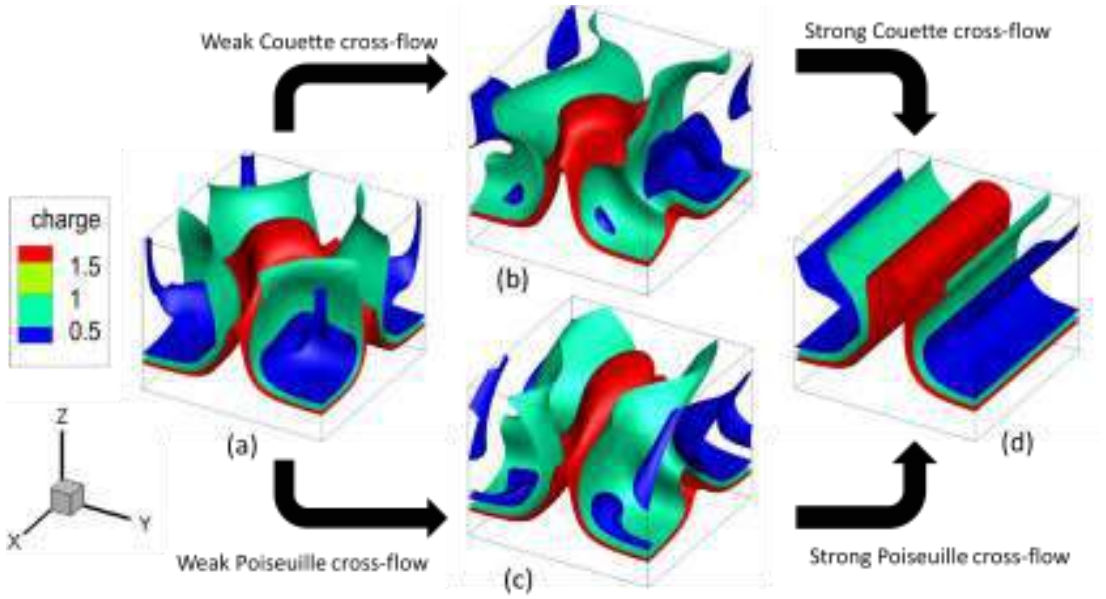

FIG. 39. Iso-surfaces of charge density for (a) square pattern without cross-flow, (b) u_{wall}=0.96m/s, (C) u_{center}=0.98m/s and (d) strong cross-flow/rolling pattern.

FIG. 40 and FIG. 41 shows the dependence of the electric Nusselt number on the non-dimensional parameter Y calculated in the x-direction. Hysteresis behavior with well-defined bifurcation is observed for both Couette and Poiseuille cross-flows. The bifurcation thresholds are $Y_c = 772.73$, $Y_f = 438.14$ for Couette cross-flow and $Y_c = 300.75$, $Y_f = 213.90$ for Poiseuille cross-flow. At $Ne = 1$ (base state) EC vortices are not present. If $Y > Y_c$, the square pattern perturbation results in oblique 3D structures. For $Y < Y_c$, any perturbation results in streamwise rolling vortices as the equilibrium solution. Oblique 3D flow features develop when shear stress is applied to the square pattern. As Y is reduced (shear stress increased), the oblique features persist until Y=Y_f, additional reduction in Y suppresses the features in transverse direction -- only longitudinal structures become possible. The Ne value is lower in 3D EC vortices; the oblique 3D structures result in decreasing Ne. When Y is close to Y_f, Ne slightly increases before transitioning to the rolling pattern value. This increase of Ne agrees with trends in maximum u_z, as shown in FIG. 34 and FIG. 35. The inserts in FIG. 40 and FIG. 41 show u_z contour plots at $z = H/2$; the u_z profiles become oblique in the cross-flow direction for both Couette and Poiseuille cross-flows. The hysteresis loop can be closed by introducing a y-directional cross-flow to suppress the rolling pattern vortices [143].

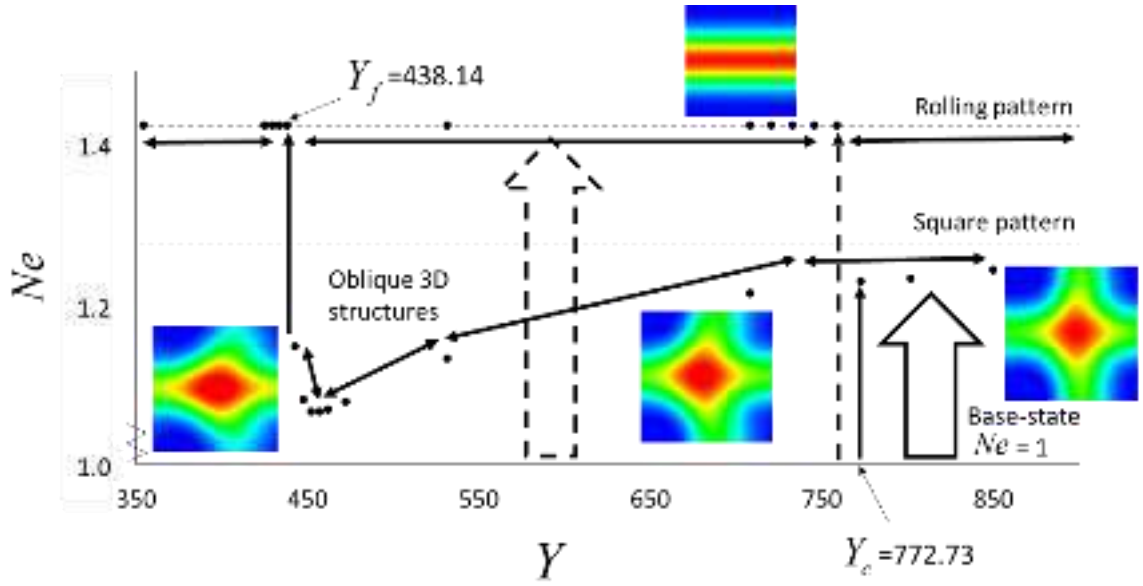

FIG. 40. Hysteresis loop of Ne versus Y for Couette-type cross-flow. The bifurcation thresholds are $Y_c = 772.73$, $Y_f = 438.14$.

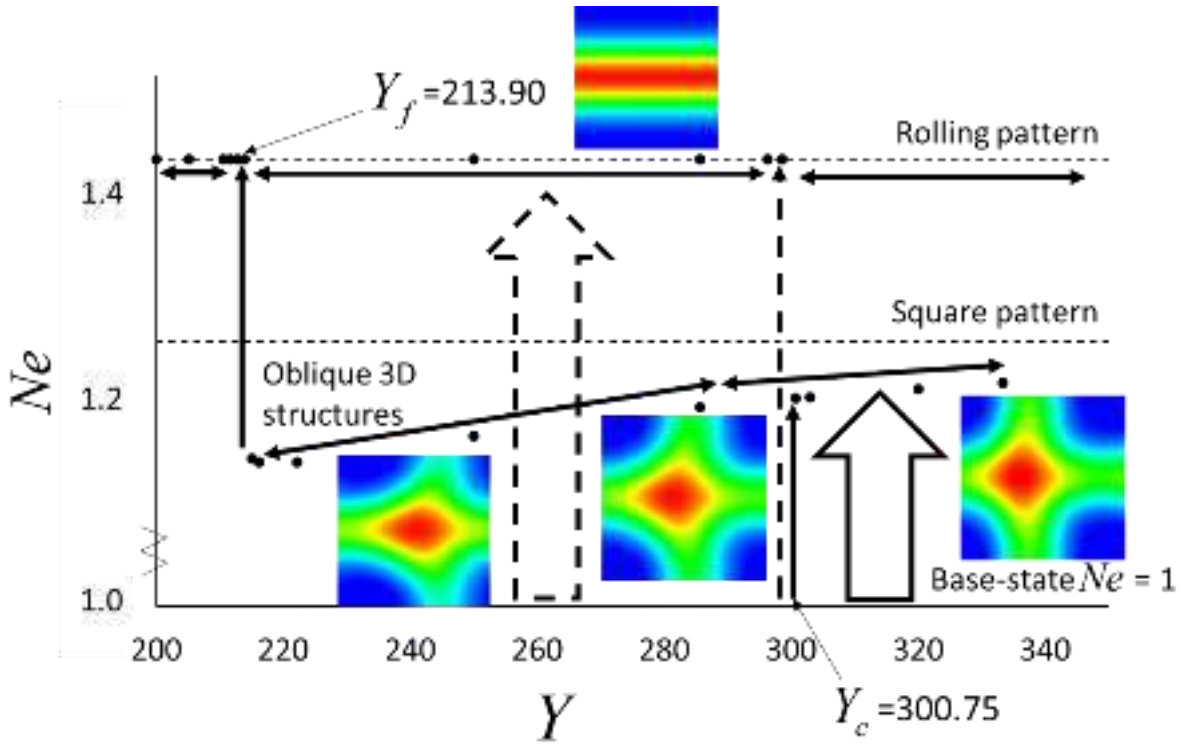

FIG. 41. Hysteresis loop of Ne versus Y for Poiseuille type cross-flow. The bifurcation thresholds are $Y_c = 300.75$, $Y_f = 213.90$.

Chapter 8. CONCLUSIONS

8.1 EHD FLOW IN POSITIVE POINT-TO-RING DISCHARGE

8.1.1 *Analytical model*

An analytical model describes the corona discharge induced EHD flow, independent of the electrode configuration, is developed and validated by comparison of the $\varphi - I$ and $\varphi - u$ relationships in the EHD flow for an axisymmetric point-to-ring configuration. The model addresses the effect of the ion motion due to the electric field on the surrounding neutral gas. The $\varphi - I$ relationship found by analytical derivation is similar to Townsend's equation, with a modified coefficient to take into account the different corona-electrode configuration. The model agrees within ~10% of the experimental measurements. The conductance term (I/φ) has a nonlinear relationship with the corona voltage φ for low electric field values. The linear trends described in the literature hold for higher corona voltages. The analytical model captures the linearity of the EHD flow velocity with the corona voltage, as shown in the experimental data for $\varphi - u_{\max}$, presented here and elsewhere [28]. The maximum velocity in axisymmetric point-to-ring EHD flow is located at the centerline.

The velocity profile predicted by the analytical model is in excellent agreement near the centerline region of the EHD generator. The analytical model over-predicts the gas velocity near the edge of the domain. The limitations of the model are the results of the simplified assumptions in the flow and electric field: (i) the application of the EHD force in the axial direction neglects the effect of the three dimensional nature of the electric field that can result in the formation of complex flow patterns; and (ii) the EHD flow generation model needs to be divided into an pure ion acceleration region model and an inertial flow section where the flow develops under the triple balance between EHD forcing, convective flow acceleration, and viscous shear stresses to capture the transition between the wall-bounded pipe flow and the EHD-driven centerline.

The new EHD flow analytical model can be generalized for electrode configurations in planar, cylindrical, and spherical coordinate systems. The model takes advantage of the fact that the ion dynamics characteristic time scale is $O(10^2)$ faster than the convective flow component. The model is readily implemented in the numerical simulation framework [174]. The multiphysics aspects of the EHD flow provide the insights into flow development and the local effect of the electric forces on the flow in complex flow geometries. The asymptotic method for estimating onset voltage and boundaries of the ionization region, similar to the approach described by Monrolin et al. [93], can be used for the description of the ionization region allowing to construct an EHD model that would not require an empirical input.

8.1.2 *Numerical model*

Numerical simulations of corona discharge-driven flow in point-to-ring geometry are performed utilizing a finite volume approach. The simulations are compared with the experimental data, which includes corona voltage, current, and velocity profile measurements. The numerical approach accounts for the electric force exerted by the ions on the neutral gas; this body force is added to the Navier-Stokes equations. The addition of the volumetric charge flux into the numerical ionization zone allows for the direct simulation of the corona-driven EHD flow. The model uses the measured corona voltage and anode current as inputs to resolve the velocity and electric fields and the charge density. Local balances of electric and inertial terms are used to determine a nondimensional parameter X, which has similarity to the electro-inertial number N_{EI} [192]. As the global criteria, $N_{EI} > 1$, indicates the presence of the secondary EHD flows [194], the local criteria, $X \geq 1$, sheds insight on the relationship between the electric body force and inertial flow and determines the flow dominated by the electric field, inertia, or viscous effects. The numerical model is validated using axisymmetric simulations compared against the experimental data for point-to-ring corona-driven EHD flow; the cathode current and the outlet velocity profile from the simulation agree within 5% error of the experimental data. The maximum velocity is directly proportional to the corona voltage, consistent with previous results [28]. Unlike in canonical internal pipe flow, the velocity profile in the point-to-ring EHD flow is analogous to a submerged jet [189], for which the Re is determined by the dimension of the acceleration zone and mean velocity. Jet values of $\mathrm{Re} = 300 - 1000$ correspond to the laminar regime in the flow acceleration region [190].

The model takes into account the effect of viscous stresses near the walls, as well as the balance between inertia and electric forces; it captures the experimental velocity profile better than the analytical model that provides accurate predictions only near the centerline. The exit velocity profile is used to calculate the electric to kinetic energy transfer efficiency. The efficiency is highest when the point-to-ring distance is largest, due to a smaller angle between the electric field gradient and the flow direction and to the lower viscous losses. The efficiency peaks at intermediate corona voltages, for a given electrode distance, due to the quadratic current-voltage relation and the nonlinear decrease of velocity away from the centerline, as well as the field line distortions caused by space charge effect near the ionization region.

8.2 EC HYDRODYNAMIC STABILITY ANALYSIS WITH AND WITHOUT CROSS-FLOW

A numerical investigation of electroconvection phenomena between two parallel plates combines (i) TRT-LBM for solving the transport equation of flow field and charged species and (ii) Fast Poisson solver. The TRT model allows for the use of two relaxation parameters, accounting for the difference between the transport properties of neutral molecules and charged species. The choice of relaxation parameters allows for both accuracy and stability over a wide variety of conditions. FFT algorithm for Poisson's equation directly solves for electric field enabling fast overall algorithm convergence. The numerical method is 2^{nd} order accurate; it shows robust performance and agrees with previous results for the hydrostatic solution and for the solution where EC vortices are present.

The 2D numerical study applies the EC stability analysis to Couette and Poiseuille flows between two infinitely long parallel electrodes. The cross-flow deforms the EC vortices and leads to their suppression. The non-dimensional analysis of the governing equations is used to derive parameter *Y,* a ratio of electric force to viscous force, in the presence of cross-flow. The non-dimensional parameter for the effect of the shear stress, analogous to a non-dimensional group Gr/Re^2 (ratio of buoyancy to the inertial forces) used to parametrize the effect of the applied shear in Rayleigh Benard convection. FIG. 23 shows a similarity behavior of *Ne* as a function of *Y*, and therefore, we suggest using *Y* as the replacement of *T* when a cross-flow is applied. The electric Ne, defined as a current ratio, is used as stability criteria. Similar to stability parameter *T* for the hydrostatic

case, a hysteresis loop with subcritical bifurcation *Ne=f(Y)* is observed. The bifurcation thresholds are $Y_c = 625.25$, $Y_f = 297.32$ for Couette flow and $Y_c = 218.58$, $Y_f = 159.36$ for Poiseuille flow.

The 3D numerical study extends the EC stability analysis of 2D flow structures in Couette and Poiseuille cross-flows between two infinitely long parallel plates. As in 2D simulations, the numerical modeling approach uses a second order TRT-LBM scheme to solve the flow and charge transport equations coupled to a Fast Poisson solver for the electric potential. Shear containing cross-flow first stretches the EC cells at obliques angles due to the interaction of streamline velocity components between the vortices and the bulk flow. These interactions form oblique 3D features before transitioning to 2D streamwise vortices at sufficiently high cross-flow velocities. The transition from 3D to 2D equilibrium states was observed for all initial perturbation schemes and independents of the domain dimensions considered in this work, i.e., square and its harmonic, oval, hexagonal, and mixed perturbations. Two transitional scenarios are studied, where the cross-flow is applied before and after the EC vortices are established. If the cross-flow is applied before the perturbation leading to the formation of EC vortices, bifurcation occurs at u_{max}=0.55m/s for Couette flow and u_{center}=0.70m/s for Poiseuille flow. If the cross-flow is applied after the EC vortices are established, the bifurcation occurs at u_{max}=0.97m/s for Couette flow and u_{center}=0.99m/s for Poiseuille flow.

DMD analysis is performed in linear growth region and nonlinear transition region, shedding insight into the development of the coherent fluid structures, predicting the linear behavior, and identifying bifurcation thresholds. The dynamic modes obtained from the linear growth region agree with the global growth rates obtained by the evolution of u_z. The DMD based predictions are in agreement with the simulation results and can be used to accelerate the computational process in the linear growth region of systems such as EC, RBC, and magneto-convection. The bifurcation thresholds between oblique 3D structures and the rolling pattern are characterized by the presence of unstable dynamic modes in the weak cross-flow cases leading to the development of oblique 3D flow features.

To parameterize the effect of cross-flow on EC vortices, the non-dimensional analysis of the governing equations uses a parameter Y in the streamwise direction. Similar to the 2D cases where

cross-flow is used to suppress rolling patterns [143], a hysteresis phenomenon in 3D cases is observed. The bifurcation thresholds are $Y_c = 772.73$, $Y_f = 438.14$ for Couette flow and $Y_c = 300.75$, $Y_f = 213.90$ for Poiseuille flow. The applied shear organizes the flow into 2D streamwise vortices and enhances the convection marked by an increase in *Ne*, similar to heat convection problem with moderate Rayleigh number [229]. The presented approach can be applied to other convection flow systems such as RBC, Marangoni effects, and magneto-convection with extended non-linear perturbation schemes such as triangular or hexagon patterns.

APPENDIX A: Chaotic electroconvection

In this chapter, we investigate the chaotic phenomenon induced by strong charge injection in low viscosity systems, i.e., high electric Rayleigh number. Following the previous chapter, we examine the case where the equilibrium state has a single period square pattern, see FIG. 25(a), and hexagon pattern see FIG. 25(d). Further generalization of transition for other patterns can be a subject of future work. The electric Nusselt number, $Ne = I / I_0$, serves as a flow stability criteria, where I is the cathode current for a given solution and I_0 is the cathode current for the base state solution without EC vortices [74,88]; thus, $Ne > 1$ when EC vortices exist. The other non-dimensional parameters are held at constant $C = 10, M = 10$, and $Fe = 4000$ [81,88] while T varies.

FIG. 42 shows that Nu is a function T for both square and hexagon patterns. The solid symbols indicate steady-state equilibrium. For an increasing T over the threshold value, T=997 for square and T=650 for hexagon, the system develops into a chaotic system if an infinitesimal perturbation is applied. The mean value of chaotic Nu is shown by hollow markers and the fluctuations are represented by the error bars. At lower T value, the Nu are very similar for both patterns, which was also observed in previous research[88,89]. When T is large, Nu asymptotically approaches approached the same value range independent of the initial patterns, which may indicate the onset of electroconvective turbulence with a broad spectrum of vorticity.

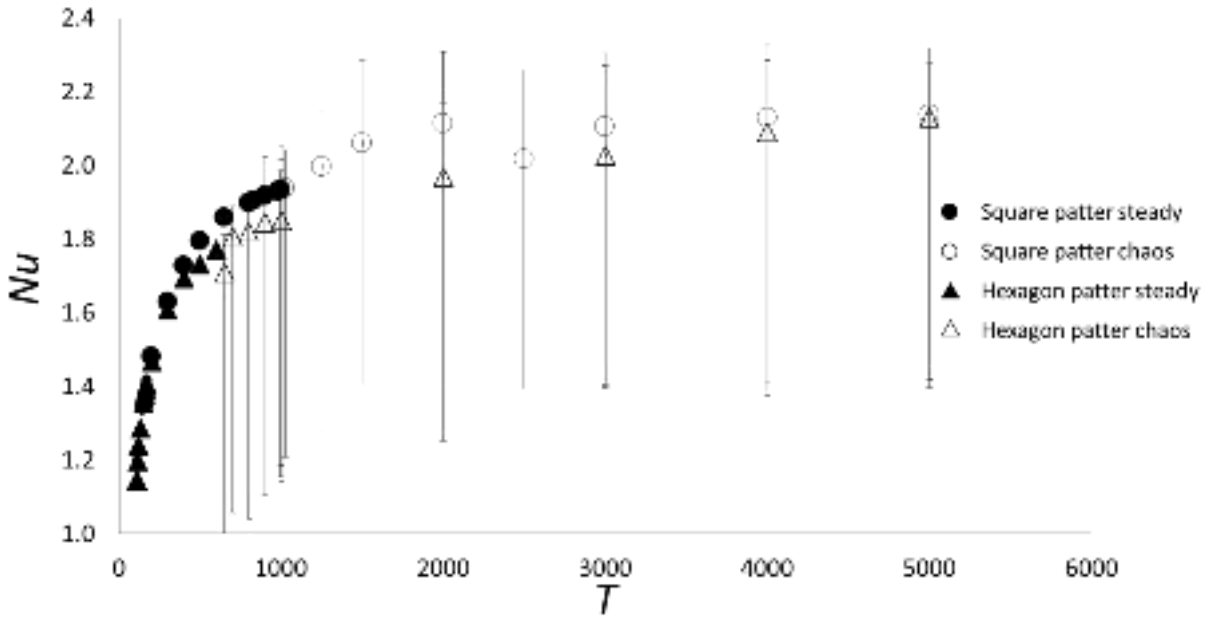

FIG. 42. Electric Nusselt number Nu is a function of electric Rayleigh number T. The onset of chaotic flow behavior occurs at T=997 for square pattern convections and at T=650 for hexagon pattern. Both square and hexagon patterns have similar values of Nu at lower T until the onset of chaos. Nu converges for T=5000 which means the initial condition is insignificant.

FIG. 43 shows the charge density contours for chaotic electroconvection with initial square and hexagon patterns. The original patterns are ostensible at the onset of chaos, i.e. T=997 for square pattern and T=650 for hexagon pattern. As T increases, the patterns become more homogeneous. When T value is large enough, the system behaves similarly, which means the initial patterns does not play a role and the Nu or convection strength depends on the system input T only.

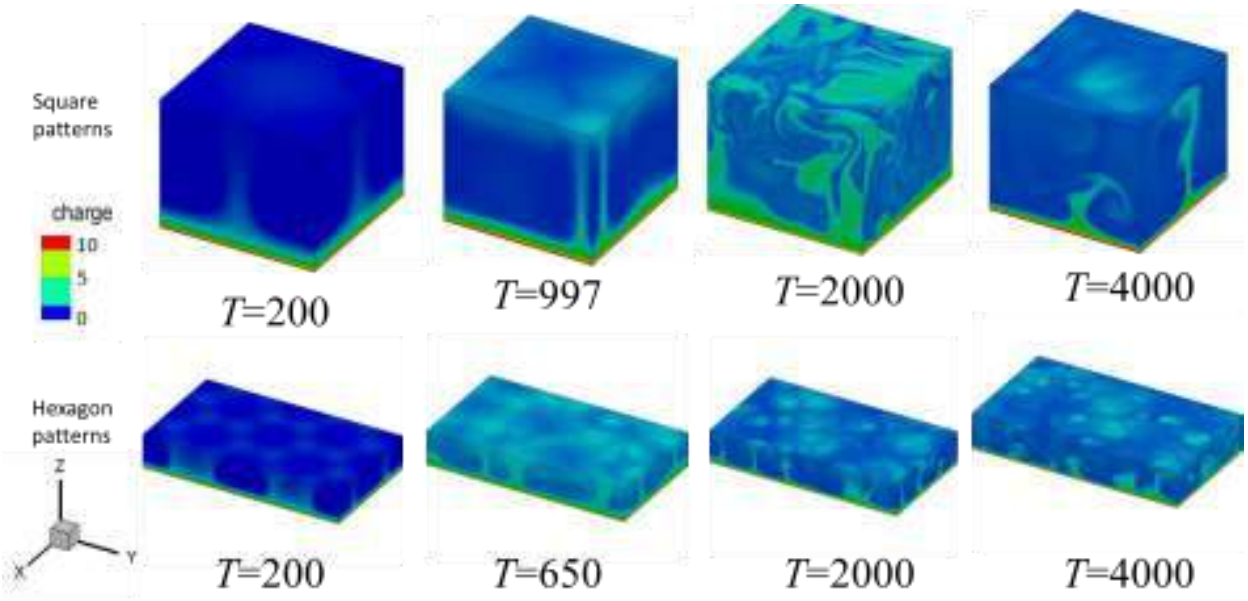

FIG. 43. Charge density contour plot for chaotic square patterns and hexagon patterns with various T values. At the onset of chaos, the patterns are ostensible, i.e. T=997 for square and T=650 for hexagon patterns. The patterns become more homogenous as T increases.

APPENDIX B: EHD flow in point to tube corona discharge[230]

INTRODUCTION

Gas phase collisions between the particles and ion medium play an important role in governing the behavior of aerosols [231-234] and dusty plasmas [235,236]. The presence of the electric field and the ion medium plays a major role in particle trapping since particles acquire a charge from ion collisions [237]. The electrostatic force on a charged particle in the electric field can be greater than gravitational, inertial and thermal forces. However, the charging mechanisms for nanoparticles in corona discharge driven flow have not been reported due to the complexity of physical phenomena and a lack of experimental data.

The EHD effect has been used for plasma-assisted combustion [238,239], convective cooling [4,240-242] and control of the aircraft [39,243]. The success of EHD technology has been limited due to the modest pressure achieved by the EHD blowers; however, in the applications with the low-pressure drop, the EHD driven flow is appropriate. Several benefits of the EHD approach are the ability to operate at a small scale without moving parts, straightforward control of the system, and quiet operation. In propulsion applications, corona induced EHD flow converts electric energy into kinetic energy

directly and breaks the size limit of any moving mechanical parts [244-246]. The current to voltage relationship describes the system behavior related to ion transport between the electrodes. The classical voltage to the current relationship is derived by Townsend for a coaxial corona configuration [247]. This quadratic relationship has been observed for other configurations, i.e., point to plate [248] and point to ring corona [174]. A generalized analytical model for voltage to current and voltage to velocity relationship for EHD driven flow has been recently developed [32]. The maximum velocity for point-to-ring electrode configuration was recorded at ~9 m/s; the analytical model has a good comparison with the experimental data at the center (EHD dominated flow), and it decreases near the walls of the internal flow channel (viscosity dominated region). To gain insight into the complex EHD flow numerical modeling is required; the properties of the electric field, ion concentration, and velocity fields can be computed using numerical methods. The ion interaction with the neutral air molecules can be modeled as an external force term in the NSE. Most EHD flow models [49,249-251] have used an iterative method to solve for the electric field and charge density. The models iteratively set a constant charge density on the anode so that the cathode current matches the experimental results. This method is inefficient and requires multiple iterations. More recent EHD modeling studies implement a more direct solver for the elliptical equation. A unified Lattice Boltzmann model (LBM) [87-90] transforms the elliptic Poisson equation to a parabolic reaction-diffusion equation. A two-relaxation-time approach was recently proposed to solve the electric field elliptical equation [142,143] directly. However, Lagrangian particle tracking, needed to study particle-flow interaction, has not been incorporated into these codes. Another approach is to introduce a volumetric flux charge density as a source term in the finite volume solver using the flux boundary conditions based on the experimentally measured current [174]. The ionization boundary has been defined by Peek's law [252]; these thresholds for the onset of the ionization are imposed in numerical ionization zone.

In Appendix B, we describe the EHD in a needle-to-tube corona discharge device. The flow is studied by the numerical simulations to resolve the spatiotemporal characteristics of ion concentration, velocity, and electric field. The numerical results are validated by the experimental data.

MODELING

The Computational Fluid Dynamics (CFD) modeling is performed to gain insight into the flow properties in the EHD device. ANSYS Fluent software was used with custom subroutines for two-way coupling of ion motion and fluid flow. Fig. 44 shows the schematic of the modeled geometry. The 2D axisymmetric assumption is used in the numerical simulation for its high computational efficiency while maintaining sufficient accuracy [174].

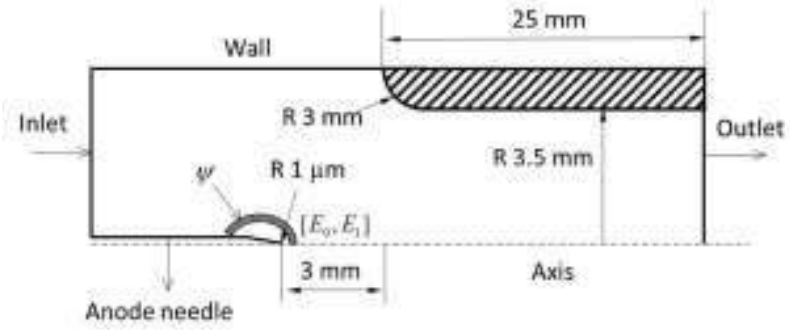

Fig. 44. Schematic of the computational domain; the model includes the ion generation region defined by the thresholds of the electric field

The flow field is solved using a finite volume laminar solver; the ion motion effects are incorporated by adding user-defined scalars to represent the electric potential φ and charge density ρ_e. The electric force's effect on the flow is solved by introducing a body force $F_e = -\rho_e \nabla \varphi$ into the momentum equations, thus the governing equations for the flow are:

$$\nabla \cdot \mathbf{u} = 0 , \tag{153}$$

$$\rho \frac{D\mathbf{u}}{Dt} = -\nabla P + \mu \nabla^2 \mathbf{u} - \rho_c \nabla \varphi , \tag{154}$$

μ is the dynamic viscosity of the air, ρ is the density of the air, $\mathbf{u}$ is the velocity vector and P is the static pressure. The equations for charge transport are:

$$\frac{\partial \rho_e}{\partial t} + \nabla . \left[\left(\mathbf{u} + \mu_b \vec{E} \right) \rho_e - D_e \nabla \rho_e \right] = S_e , \tag{155}$$

$$\nabla^2 \varphi = -\frac{\rho_e}{\varepsilon_0} , \tag{156}$$

where μ_b is the ion mobility, which is approximated as a constant [*2.0E-4 m^2/(Vs)*] [32,174] and ε_o is the electric permittivity of free space. D_e is the ion diffusivity described by the electric mobility equation (Einstein's relation) [32,174]:

$$D_e = \frac{\mu_b k_B T}{q} \quad , \tag{157}$$

where k_B is Boltzmann's constant ($\sim 1.381\times10^{-23}$ J/K), T is the absolute temperature, and q is the electric charge of an ion, which is equal to the elementary charge (1.602×10^{-19} C). S_e is the source term of charge density which has a unit of $C/m^3.s$, it is calculated from the corona current measured at the anode. In the simulation, the charges are introduced into the computational domain within the ionization zone boundary region at the rate calculated from the anode current. Instead of defining a thin surface within the computational domain to mark as the ionization zone boundary, a region with finite volume is determined by the electric field strength magnitude and constrained within 1mm of the needle tip.

$$S_e = \begin{cases} I/\psi, for\ |E| \in [E_0, E_1] \,\&\, x_{tip} - x < 1mm \\ 0, otherwise \end{cases} \quad , \tag{158}$$

where ψ is the volume of the region satisfying $|E| \in [E_0, E_1] \,\&\, x_{tip} - x < 1mm$ and I is the corona current. The $x_{tip} - x$ term limits the ion production along the needle; in the experiments, the needle tip extends only 1 mm from the needle holder. E_0 is the critical field below which the number of ions recombination is larger than production per drift length, and it is for air. E_1 is the breakdown electric field strength for air (*3.23 MV/m*). In fact, both E_0 and E_1 can be used as the criteria for ionization boundary. Since the charge density is balanced inside the ionization region, the corona current equals to the charge density flux at the ionization boundary. Therefore, by introducing a volumetric flux of charges coming into the domain, the two ionization boundary conditions are used to mark the numerical "ionization region" where the charges (ions) are generated. More details on the treatment can be found in [174].

Table X shows the numerical schemes used in the CFD calculations. The second order upwind scheme is used to reduce numerical diffusion. The transient laminar solution is computed, the convergence criteria and the simulation time are set to achieve time steady velocity profile at the outlet. Since the ions drift velocity is orders of magnitude greater than the convective flow velocity, the solution for charge transport and electric field converge significantly faster (in convective time)

than the flow equations. The boundary conditions are shown in Table XI. The total pressure difference between the inlet and outlet is zero as the flow is accelerated only by the ionic drag.

Table X. Numerical schemes for CFD

Model Parameter	Spatial Discretization
P-V Coupling	SIMPLE
Pressure	2nd order upwind
Momentum	2nd order upwind
Electric potential	2nd order upwind
Charge density	1st order upwind

Table XI. Boundary conditions for the numerical simulations

Boundary	The value given at the boundary
Inlet pressure	Atmospheric pressure
Outlet pressure	Atmospheric pressure
Anode needle	3~5 kV & Zero diffusion flux for charge
Cathode tube	0 kV & Zero diffusion flux for charge
Wall boundaries	Zero diffusion flux for electric potential & charge density

RESULTS AND DISCUSSION

Voltage-Current Characteristics

The corona current and the downstream ion concentration are measured to determine the ion production and ion transport. **Table Xii** shows the corona current (anode current) vs. anode voltage. The current increases with the applied voltage quadratically, which agrees with other results in the literature for different corona configurations [19,247,248,253,254]. The current values from the experiments were used in the numerical model as the ionization zone boundary condition. In some previous literature, the input charge density was iteratively adjusted to match the measured cathode current, e.g. [242,255]. Here, the cathode current is computed by the code using the ionization model; the numerical model uses corona voltage and anode current as input parameters. The cathode current is determined by integrating the charge flux on the cathode

$$I_{cathode} = \int_{\substack{cathode \\ area}} -\mu_b \rho_e \nabla\varphi \mathbf{dA}_{\mathbf{cathode}} \quad , \tag{159}$$

where $I_{cathode}$ is the cathode current and $\mathbf{A}_{\mathbf{cathode}}$ is the area vector of the cathode.

Table XII. Comparison of cathode current between the experiments and CFD

Voltage (kV)	Anode current (μA)	The experimental cathode current (μA)	CFD cathode current (μA)
3	0.7	0.62	0.59
4	3.8	3.34	3.23
5	7.5	6.68	6.64

The cathode current in the simulation agrees within 5% with the experimental measurements. The cathode recovers 85-90% of the ion current that is generated; the other 10-15% are associated with ions exiting the geometry. These computed values of cathode current yield good agreement against the experimental data validating the numerical approach with respect to ion concentration field in the ionization and collection regions of the EHD collector.

The numerical approach models the process by which the ion-molecule collisions accelerate the bulk flow. Fig. 45(a) shows the computed electric field lines. The maximum electric field strength is near the tip of the corona needle where a small radius of curvature concentrates the electric field lines; the field intensity reaches the threshold for ion generation. The effect of the space charge on the electric field is apparent by field line distortions in the region of high ion concentration. These distortions are significantly smaller away from the electrode tip where the charge density is reduced.

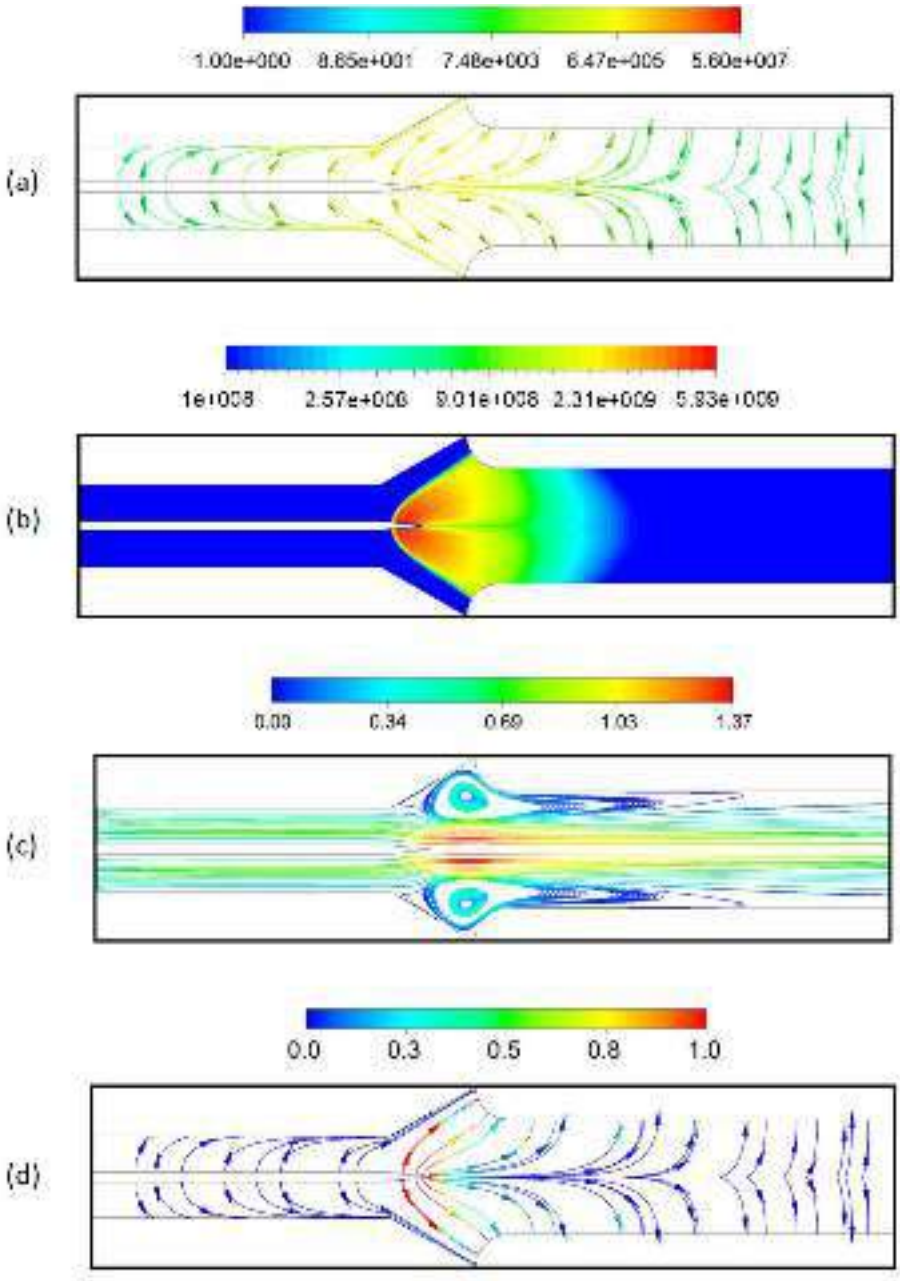

Fig. 45. Contour plots of the (a) electric field (V/m), (b) ion concentration (#/cc), (c) velocity (m/s) and (d) electric field lines by the non-dimensional parameter X for 3 kV corona voltage between the needle and the ground tube. The dash lines on the velocity contour (c) indicate the location at which the velocity of EHD flow is compared with the experiments. (d) The contours of X are clipped to the value of unity; the region which indicates EHD dominated flow.

Fig. 45 (b) shows the ion density contours. The ions are generated at the needle tip, and their motion is dominated by the electric field due to their high electric mobility, as the ion drift velocity is two orders of magnitude greater than the bulk flow [174,248,256]. Downstream of the charging region, the electric field is weak, especially near the centerline, and ions exit the domain due to

high flow velocities. A recirculation zone is formed upstream of the cathode tube near the rounded edge as shown in Fig. 45(c). This is due to the flow expansion which creates an adverse pressure gradient in the near wall acceleration region. To determine the effect of the Coulomb force in the EHD flow, the ratio of electrostatic force to the inertial force is plotted; this ratio is described as a non-dimensional parameter $X = \rho_e \varphi / \rho \mathbf{u}^2$ [174]. Fig. 45(d) shows electric field lines colored by the values of X, indicating the regions where the electric force is greater than inertial force dominating the flow is located between the corona needle and the ground tube.

Velocity Voltage Characteristics

To validate the EHD modeling approach, the numerical results for corona voltages of φ = 3-5 kV are compared with the experimental exit velocities. Fig. 46 shows the velocity profiles plotted for three voltage values. The experiments and numerical results show the maximum velocity is located at the centerline; the profile decays with radial distance. The maximum velocity of the point-to-cylinder corona discharge device is ~4m/s for both experiments and simulations at 5kV corona voltage. At higher voltages arc discharge occurs, the flow velocity drops to zero. The maximum velocities in the numerical simulation are within 10% of the experimental data; the predictions are less accurate at the edges of the domain. The maximum outlet velocity increases linearly with corona voltage. The linear trend of centerline velocity is observed previously in experiments [174,256].

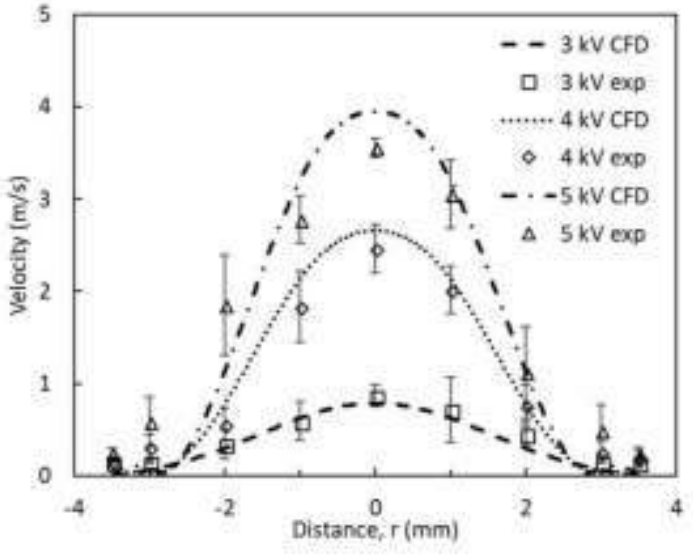

Fig. 46. Comparison of velocity profile between the experimental results and simulations at the outlet of the EHD induced flow device as shown in Fig. 45(c).

The velocity profile shows that EHD induced flow in a point-to-tube corona discharge resemble Poiseuille flow near the axis and is significantly different from the pressure-driven flow profile near the walls. The point EHD source generates the flow similar to the submerged laminar jet flow [257]. Laminar flow characteristics are apparent from the experimental data. The Reynolds number (*Re)* is determined based on the tube diameter and the mean velocity at the exit; *Re*~160 for corona voltage of 3 kV and *Re*~400 for corona voltage of 5 kV. Since the 6 kV cases result in the arc, it appears that the corona induced flow without additional contribution from pressure term remains laminar for the considered internal flow geometry. If any high local Re number regions or flow instabilities are present in the jet at its source, these temporal fluctuations decay by the time the flow reaches the outlet.

APPENDIX C: Numerical investigation of corona discharge induced flow on a flat plate

The EHD flow is studied on a conducting flat plate with a shallow rectangular cavity. Fig. 47 shows the schematic representation of corona discharge induced flow in the wall boundary layer region on a conducting flat plate with a cavity. Its objective is to accelerate the flow near the wall to modify the boundary layer profile. The serrated edge copper electrode with a thickness of 0.2 mm serves as the anode. The pitch of the sawtooth is 5 mm. The ground electrode is a 1.5 mm thick steel rod. The flat plate is fabricated using 3D printing in polylactic acid polymer. A shallow rectangular cavity of 15 mm wide and 1.3 mm deep is built into the flat plate to aid ionization.

The anode overhangs the backward facing step of the cavity by 6 mm, as shown in Fig. 47 such that the distance between the anode tips and the cathode (L) is 9 mm. The width of the experimental setup is 100 mm. The cathode is flush mounted against the forward-facing step, see Fig. 47. The top of the electrode protrudes 0.2mm above the flat plate. The cathode protrusion results in the Stokes flow, not affecting the downstream velocity profile development.

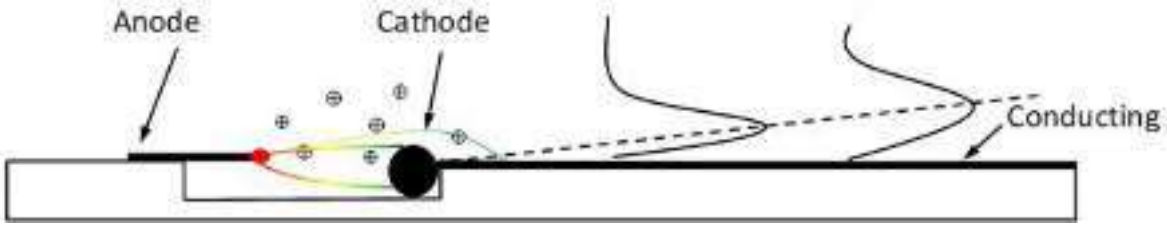

Fig. 47. Schematic diagram of the corona driven EHD wall jet; colored lines show electric field line, solid down – velocity profile.

The flow field is solved using a finite volume laminar solver; the ion motion effects are incorporated by adding user-defined scalars to represent the electric potential φ and charge density ρ_e. The electric force's effect on the flow is solved by introducing a body force $F_e = -\rho_e \nabla \varphi$ into the momentum equations, thus the governing equations for the flow are:

$$\nabla \cdot \mathbf{u} = 0 , \tag{160}$$

$$\rho \frac{D\mathbf{u}}{Dt} = -\nabla P + \mu \nabla^2 \mathbf{u} - \rho_c \nabla \varphi \ . \tag{161}$$

μ is the dynamic viscosity of the air, ρ is the density of the air, $\mathbf{u}$ is the velocity vector and P is the static pressure. The equations for charge transport are:

$$\frac{\partial \rho_e}{\partial t} + \nabla . \left[\left(\mathbf{u} + \mu_b \vec{E} \right) \rho_e - D_e \nabla \rho_e \right] = S_e \ , \tag{162}$$

$$\nabla^2 \varphi = -\frac{\rho_e}{\varepsilon_0} \ , \tag{163}$$

where μ_b is the ion mobility, which is approximated as a constant [*2.0E-4 m^2/(Vs)*] [32,174] and ε_o is the electric permittivity of free space. D_e is the ion diffusivity described by the electric mobility equation (Einstein's relation) [32,174]:

$$D_e = \frac{\mu_b k_B T}{q} \ , \tag{164}$$

where k_B is Boltzmann's constant ($\sim 1.381 \times 10^{-23}$ J/K), T is the absolute temperature, and q is the electric charge of an ion, which is equal to the elementary charge (1.602×10^{-19} C). S_e is the source term of charge density which has a unit of $C/m^3.s$, it is calculated from the corona current measured at the anode. In the simulation, the charges are introduced into the computational domain within the ionization zone boundary region at the rate calculated from the anode current. Instead

of defining a thin surface within the computational domain to mark as the ionization zone boundary, a region with finite volume is determined by the electric field strength magnitude and constrained within 1mm of the needle tip.

$$S_e = \begin{cases} I/\psi, for\ |E| \in [E_0, E_1] \,\&\, x_{tip} - x < 1mm \\ 0, otherwise \end{cases}, \tag{165}$$

where ψ is the volume of the region satisfying $|E| \in [E_0, E_1] \,\&\, x_{tip} - x < 1mm$ and I is the corona current. The $x_{tip} - x$ term limits the ion production along the needle; in the experiments, the needle tip extends only 1 mm from the needle holder. E_0 is the critical field below which the number of ions recombination is larger than production per drift length, and it is for air. E_1 is the breakdown electric field strength for air (*3.23 MV/m*). Both E_0 and E_1 can be used as the criteria for ionization boundary. Since the charge density is balanced inside the ionization region, the corona current equals to the charge density flux at the ionization boundary. Therefore, by introducing a volumetric flux of charges coming into the domain, the two ionization boundary conditions are used to mark the numerical "ionization region" where the charges (ions) are generated. More details on the treatment can be found in [174].

Commercial package ANSYS Fluent was used with user-defined functions to model the three-way coupling of ion motion, electric field, and fluid motion. Fig. 48 shows the schematic of the modeled geometry; the 2D assumption is used in the numerical simulation

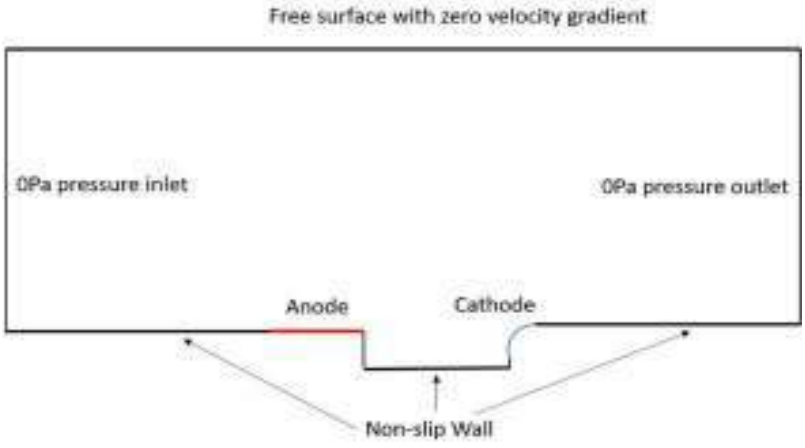

Fig. 48. Computational domain for the numerical simulation

RESULTS AND DISCUSSION

The CFD models the process by which the ion-molecule collisions accelerate the bulk flow. Fig. 49 (a) shows the ion density contours. The ions are generated at the anode tip, and their motion is dominated by the electric field due to their high electric mobility, as the ion drift velocity is two orders of magnitude than the bulk flow [248]. The effect of space charge is observed as the charge density drifts upstream. The cathode recovers 85-90 % of the ion current that is generated, the other 10-15 % of charge species are recovered on the conducting plate reducing the parasitic effect of ions traveling upstream, as seen in the point to ring corona with insulating walls [174]. To parameterize the effect of the electrostatic force on the flow, the ratio of electric to the inertial force is defined as a non-dimensional parameter $X = \rho_e \varphi / \rho \mathbf{u}^2$ [174]. Fig. 49 (b) shows the velocity streamlines colored by the values of X, indicating the regions where the electric force is greater than the inertial force. The electric force is dominant between the cathode and anode where both the ion concentration and electric field strength are high. In the region downstream of cathode the effect of the ion interaction with the flow is minimal.

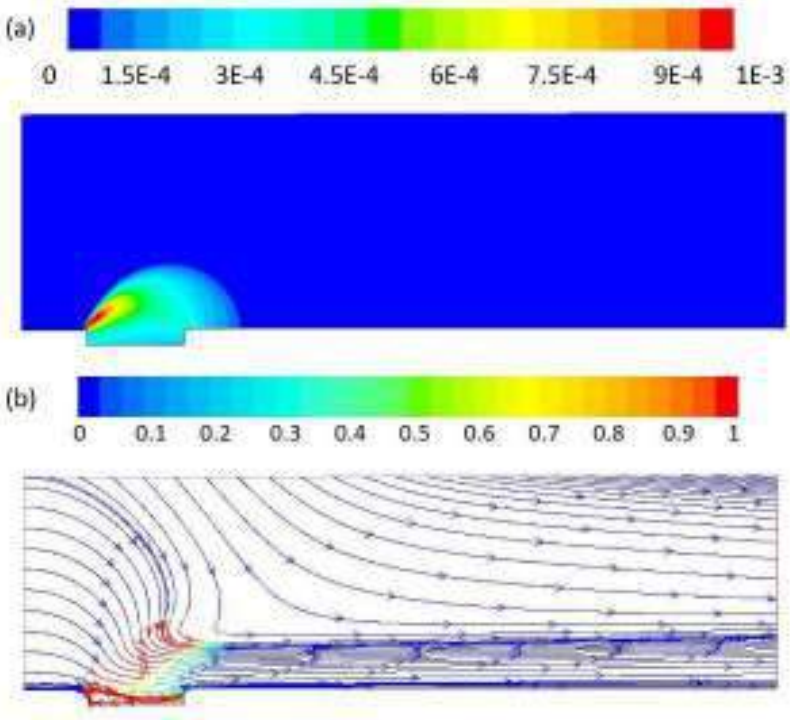

Fig. 49. Contour plots of the (a) charge density (C/m^3) and (b) streamlines by local X (clipped to 1) for 8 kV case. Maximum - X=100

Velocity Voltage Characteristics

The numerical results for φ = 8 kV case are compared with the experimental velocity profiles. The corona driven flow entrains gas in the vicinity, both streamwise and normal (impinging) components are present upstream of the cathode. Downstream of the cathode the normal component diminishes. The experimental and numerical velocity profile downstream of the cathode show similar trends exhibiting wall jet behavior [258-260]. The velocity reaches a maximum and then decays to near zero away from the plate. Both CFD and experimental data show the maximum velocity is 2mm from the surface. The maximum velocities in the numerical simulation are ~ 1.7 m/s, and it is within the 10% of the experimental data.

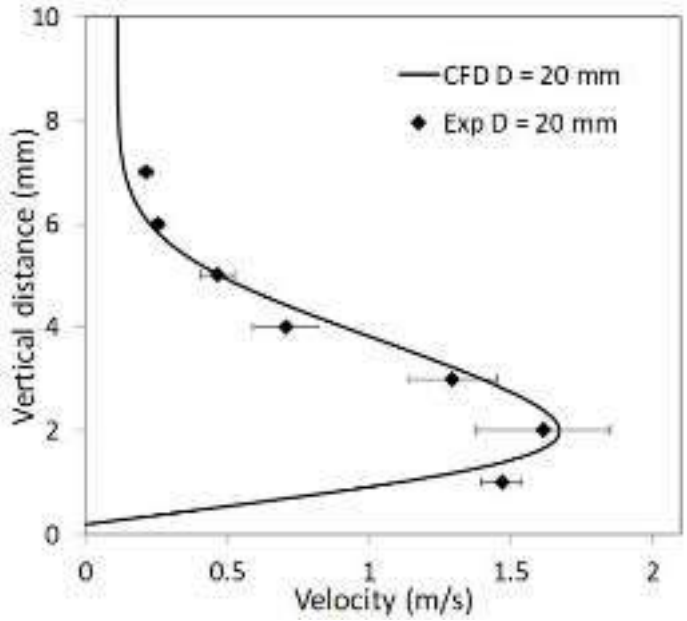

Fig. 50. Comparison of velocity profile between the experimental results and simulations at D = 20 mm of the EHD induced flow on a flat plate

Energy Transfer Efficiency

The energy conversion efficiency can be calculated from the ratio of the kinetic energy flux to the electric power produced by the corona discharge.

$$\eta = \frac{\frac{1}{2}\rho \int u^3 dA}{\varphi I} \quad , \tag{166}$$

The corona voltage and the anode current are obtained from the experiments. The kinetic energy flux is calculated for both experimental and numerical velocity profiles. TABLE XIII shows the values that are used for calculation. The energy transfer coefficient to the fluid is greater for

external flow compared to internal flow due to entrainment of the surrounding fluid. Parasitic losses associated with the upstream motion of the ions and formation of the flow recirculation zone due to adverse pressure gradient are largely avoided by the introduction of conducting surface downstream of the cathode.

TABLE XIII: Comparison of electric and kinetic power between the experiments and CFD

	8 kV
I (μA)	35
$W_{K, Exp}$ (mW)	6.1 ± 15.2%
$W_{K, CFD}$ (mW)	5.9
W_E (mW)	280

Energy transfer efficiency is 2.17 % ± 0.33% based on experimental and 2.1% based on CFD results. It was previously shown that the energy transfer efficiency is non-linear with respect to corona voltage [174]. The energy transfer efficiency for external flows is higher than in the point to ring internal flow (~ 1%) [174]. Further improvement in the energy transfer efficiency can be achieved by optimization of electrode geometry configuration, operational condition.

CONCLUSION

This work presents an experimental and numerical investigation of planar corona discharge in the wall boundary layer. The experimental data includes voltage, current, and velocity profile measurements. Multiphysics numerical simulation sheds insights into the interaction of force exerted by the motion of the ions in the electric field on the airflow. The addition of charge flux as a generation of ions allows for the direct computation of electric body force. The numerical simulations agree with the experimental data within 10%. The velocity profile of the corona driven is similar to a wall jet downstream of the cathode. Parametrization of the EHD wall jet and comparison with the traditional wall jet can be achieved using CFD modeling. The integrated velocity profile is used to calculate the electric to kinetic energy transfer efficiency. The efficiency is ~2%, which is greater than in the internal flow geometry due to higher flow entrainment. Energy transfer efficiency can be optimized by electrode geometry configuration, operational conditions.

APPENDIX D: Evaluation of lean blow-out mechanism in a toroidal jet stirred reactor[261]

INTRODUCTION

Jet stirred reactors (JSRs) are typically used to study gas-phase kinetic oxidation and pyrolysis [262] and pollutant species formation. The intense mixing in the JSR approximates the flame zone in gas turbine application. For example, Sturgess et al. used the jet-stirred reactor to study the flame stability within a gas turbine combustor [263]; other researchers focused on NOx formation with respect to the combustion conditions and fuel composition [264,265]. The intense mixing in the JSRs, in principle, allows to simplify the modeling of turbulence-chemistry interactions; however, in many practical scenarios, the composition in the reactor cannot be assumed to be uniform. In this work, we investigate a lean blowout (LBO) mechanisms of a toroidal jet-stirred reactor.

Research literature suggests several mechanisms of LBO, relating the flame blowout to the conditions in the flame stabilizing flow structures. In the study of combustion stabilized by the bluff body recirculation, Longwell et al. [266] suggested that the combustion within the recirculation zone can be approximated as a homogeneous second-order chemical reaction region. Plee et al. [267] developed a model that calculates the characteristic times for fluid mechanics and chemical kinetics to the study of flame stabilization near blowout. The authors found that the ratio of the fluid mechanic time scale to the chemical time in the shear layer agrees with the experimental data of Zukoski [268]. Glassman generalizes the approach by relating the blowout limit to a ratio of the residence time and chemical kinetic time scale, which is also known as the Damkohler (*Da*) number [269]. The chemical reaction time scale (τ_{chem}) is based on the Arrhenius chemical kinetic rate and is independent of the geometry length scales. As noted by Turns [270], in well-stirred reactors, the mean residence time for the gaseous fuels in the reactor is defined as $\tau_{res} = \rho V/\dot{m}$, where ρ is the mean density inside the reactor. In the PSR limit, the residence time in the combustion system must be greater than the chemical reaction time, or $Da>1$, to sustain combustion [269]. An alternative definition of *Da* number is a ratio of turbulent time scale to the characteristic chemical time scale $Da= \tau_{turb}$ scale$/\tau_{chem}$, which often used to studies turbulent premixed flames [270]. Several studies examine the role of major combustion species and free

radicals, such as CO and hydroxyl (OH) radicals on flame stability [271-275]. Other studies investigate the effect of additional species, such as hydrogen [272], CO [276], or alternative fuels [277] on LBO. Understanding the interaction between fluid dynamics and chemical kinetics near the LBO region for industrial systems and aero-engines is critical for improving the design and for optimizing the operational envelope related to combustion stability and pollution control. The interaction of the flame with the recirculation zone in LBO mechanisms have been studied for gas turbine applications [278] or aero-engine combustors [279]. The transient behavior of the flames and their interaction, when stabilized by recirculating, are found to significantly affect the LBO [280].

Due to the rapid development of computational power and state-of-the-art fluid dynamics and combustion models, CFD became widely used in modeling turbulent combustion flows. The LBO condition for the gas turbine combustor has been previously investigated using CFD modeling, e.g., [263,281,282]. The Reynolds-averaged Navier-Stokes (RANS) model is often used in modeling industrial combustors due to its low computational cost [283]; recently, large eddy simulation (LES) [284,285] models gained popularity due to their ability to resolve turbulent structures in the inertial range. These models provide more accurate results, but they suffer from high computational cost, especially when modeling practical combustion systems [281,284,285]. RANS simulations with the Reynolds stress model (RSM) closure model has been shown appropriate for modeling swirling turbulent flow using a steady-state approach with relatively low computational cost [286-289]. In modeling combustion systems, several investigators concluded that the RSM produces a good agreement with experimental data [283,290,291]. To incorporate combustion chemistry in flow simulations, among other models, Magnussen et al. proposed an eddy-break-up (EBU) model and later extended the EBU model, which is known as the eddy dissipation concept (EDC) model [292-294]. The EDC model has been used to model different combustors, including laboratory reactors [295] and industrial burners [296]. However, under certain conditions, such as reacting impinging jets, EDC has been shown to overpredict the chemical reaction rate due to the high turbulence dissipation rates near the wall [297].

The laboratory TJSR was developed [298] to enhance the mixing characteristics in the combustor compared to the spherical combustor [299-302]. The mixing behavior inside the TJSR was modeled [303] as 0D, 1D, and 2D coalescence-redispersion models examining the effect of the jet angles, the

number of jets on the mixing frequencies, and the characteristic times. Barat [304] studied the behavior of the TJSR near blowout; he concluded that turbulent mixing is fast relative to the chemical time, so the temperature and species composition gradients should be negligible. He suggested that at high-temperature conditions, the TJSR approaches PSR-like behavior. At lower equivalence ratios, the temperature and emissions measurements indicated localized regions of extinction, which was attributed to a failure of the incoming jet fluid to ignite as it entrained the surrounding bulk gasses. The author hypothesized that the reactor volume effectively decreases near blowout due to localized extinction. More recently, Vijlee et al. [305,306] presented new data and CFD modeling for the TJSR, relating the OH levels to the reactor LBO. The first order CFD model and PSR model showed moderately good agreement with the temperature data for higher fuel-air ratios but failed to predict the blowout accurately. In this work, both first order and second order discretization models are investigated. The first order model provided is found to be of limited usefulness for modeling the complex flow, even with the heat transfer modeled and mesh refined. A higher order scheme is needed to gain insight into the LBO mechanism.

LBO mechanism based on the local parameters in the TJSR is investigated. The unanswered questions related to the understanding of LBO in the swirl stabilizing TJSR are: (i) if the high-order discretization steady-state CFD has the potential to model the behavior of the flame in the TJSR accurately, and (ii) if the local flame extinction events trigger the global LBO. To test these hypotheses, we investigate the blowout behavior in a TJSR operated on methane using 3D CFD; the results are compared with the experimental data of Vijlee et al. [305,306]. Effects of the numerical discretization scheme on LBO prediction are evaluated over a range of fuel-air equivalence ratios using a skeletal chemical kinetic mechanism based on GRI 3.0 [295] with the EDC model. The modeling is used to gain insight into the combustion parameters related to flame stability and the lean flame blowout mechanism.

COMPUTATIONAL SETUP

The reaction chamber of the experimental TJSR [305,306] has a total volume of 250 mL. FIG 51 shows the solid model of the TJSR. The reactor body is constructed of aluminum oxide ceramic. The ports on the lower toroid are used for the placement of an emission probe, a thermocouple, an igniter, and a pressure sensor. An Inconel nozzle ring has 48 nozzles (ID 0.86 mm each), which are angled 20 degrees to the toroid

radius, as shown in FIG 52. The jet angle facilitates the toroidal flow pattern in the reactor. In the experimental study, the gas temperature is measured 5 mm above the bottom of the reactor.

FIG 51: TJSR schematic: the reactor volume is 250 mL, the nozzle ring has 48 nozzles ID0.86 mm, angled 20 degrees from the toroid radius. The ports in the lower section are used for an emission probe, a thermocouple, an igniter, and a pressure sensor.

In a previous CFD modeling study of the TJSR, Briones et al. [307] used symmetry assumptions for the reactor mid-plane (aligned with fuel-air nozzles). In a later study, Vijlee et al. [306] modeled a single section with one jet (out of 48 identical jets) by applying periodic boundary conditions; the authors allowed the flow to develop in poloidal and toroidal directions and observed significant asymmetry within the TJSR flow pattern. **Table XIV** and **Table XV** summarize the boundary conditions and the numerical algorithm used by Vijlee et al. One of the concerns related to the previous modeling efforts is the use of the linear stress-strain relation in modeling swirling turbulent flow which neglects the anisotropy and flow curvature [308]. The model has good agreement with the experimental temperature measurements for stable combustion conditions due to the fitted heat loss rate. However, the model does not show good agreement for blowout conditions, which can be attributed to the several assumptions made by the authors: the added numerical viscosity of the low order numerical scheme simplified model for heat loss and the use of the linear stress-strain relation.

FIG 52 shows a 3D view of the computational domain, 15-degree section of the toroid which includes two (out of 48) nozzles to account for the jet-jet interaction; the two-jet section was not modeled successfully in the previous work [306]. The periodic boundary conditions used here neglect the flow patterns and instabilities in the toroidal direction. Nevertheless, this assumption provides a practical (engineering) approach, which is required to model the reacting flows in a relatively large domain with small mesh size. Limited simulations using three jets show nearly identical

results with the two-jet model. The jet-jet interaction affects the formation of flow pattern as the round jets merge into the planar jet downstream of the inlet. The flow patterns in the region between the jets determine the interaction of the two recirculation zones. Periodic boundary conditions allow for the interaction between adjacent sections with the low computational cost. The fuel-air mixture inlets model as square channels of the same effective area as a round nozzle to match the inlet velocity. The major flow patterns include poloidal and toroidal recirculation zones and the transitional zone where the interaction between the recirculation regions occurs.

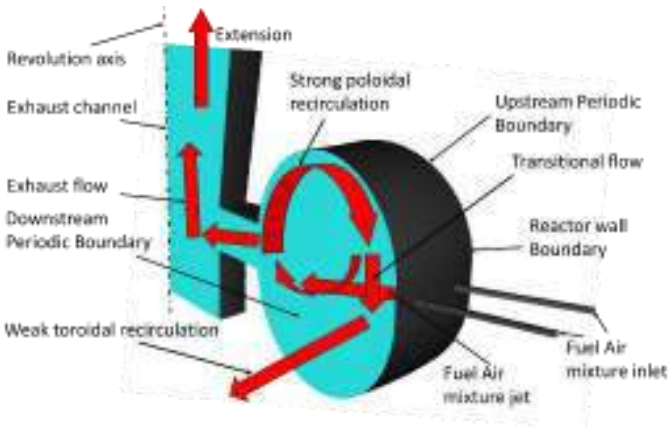

FIG 52: Computational domain with the boundary conditions and major flow patterns. The model includes two jets angled at 20 degrees from the radial direction. The axis indicates the axial symmetry.

The periodic faces are set as a rotational periodic boundary condition. The fuel-air inlet is set to a pressure inlet using the experimental values; the assigned inlet pressure in the CFD matched the experimental flow rates. The pressure outlet boundary condition is set to atmospheric pressure. The flow straightener located in the reactor exhaust pipe is not modeled due to difficulty with meshing; instead, a 1-meter long extension section is added; the outlet flow direction is set normal to the outlet face eliminating reverse flow to aid model convergence. We assume that the downstream boundary condition does not affect the flow behavior in the toroidal section of the reactor.

Another major difference between this and the previous model is in the heat transfer modeling. The previous work assumed the uniform temperature profile of the reactor inner wall to match an average calculated heat loss of 2.5% based on the flow rate and fuel heating value. The assigned wall temperature profile results in gas temperature over-prediction in the TRZ. Our model has

refined mesh near the wall to capture the temperature gradient in the wall boundary layer. During the simulation, the wall temperature is calculated based on the local heat transfer coefficient; the model includes conduction through the wall, free convection/radiation heat transfer is set for the outside wall. The walls are modeled as non-slip boundaries with scalable wall function [309]. The boundary layer is constrained so that the first grid point is located at a distance of $y^+ = 1$. The wall conduction model includes triple-layer shell conduction with a 20 mm-thick 85% alumina layer, a 10 mm Kaowool insulation, and a 1 inch steel housing. The external emissivity is assigned to be 0.8 according to the properties of the oxidized steel [310]. The heat transfer coefficient calculations follow the methodology described in [311]. The Nusselt number is approximated based on the velocity field in the reactor [312]. The typical size of an element in the combustion region is of the order of 1e-3 mm3. The typical mesh size of the exhaust tube is 1 mm3; the maximum cell size within the exhaust tube can be as large as 10 mm3. The mesh size is unable to eliminate the truncation errors generated by the numerical discretization, which may require a mesh size at the Kolmogorov scale to resolve all the turbulence structures, which is currently not possible in high Reynolds number reacting flow for a practical combustor. In this work, a second order discretization is used to reduce the truncation error, compared to the first order scheme used in the previous work [306]. Mesh independence studies have been performed for both 1st and 2nd order schemes.

The mesh comprises of hexagonal elements; after conducting the mesh independence study, the size of the mesh is around 313,000 elements. The commercial software ANSYS Fluent (v17.0) [313] is used. RSM is used as the turbulence closure model [287]; Yang et al. [290,291] found that the model is well suited for predicting the effect of swirling flow on jet entrainment rates. Gravity is included in the simulations. Several combustion kinetic modeling options have been considered; although the global mechanisms have been used for the modeling of industrial combustors due to their efficiency, these mechanisms are limited to only the major combustion species and are, thus, not well suited for studying LBO [282,314]. Detailed chemical kinetic mechanisms are the best option. However, the high computational requirements often make them prohibitive for use in a parametric study. A skeletal chemical mechanism of Karalus et al. [295] is used as a compromise between computational efficiency and the ability to provide detailed species concentration. The chemical mechanism contains 22 species and 122 reactions; it predicts a similar blowout ϕ as the GRI 3.0

when applied in a PSR. Two sets of numerical simulations are performed to test the hypothesis that the high-order discretization scheme can describe flame behavior in a toroidal reactor near blowout. In the CFD simulation, heat capacity, mass diffusivity, and viscosity are calculated using the mixing law approach. The species diffusion is modeled by multicomponent diffusion, and the thermal diffusion is modeled using kinetic theory. The turbulent diffusivity is modeled using the RSM turbulence closure model. The turbulent Prandtl number ranges from 0.75 to 0.85; the Schmidt number is ~0.74. These values agree with the typical values reported in the literature [315]. The CPU time is 180 sec/core-iteration, and one solution requires ~3000 iterations to converge; thus, the CPU time is about 5.4e+5 sec/core-solution. Table XIV and Table XV summarize the boundary conditions and the numerical algorithm used in this study.

Table XIV. Boundary conditions for the numerical simulations.

Boundary	**Type**	**Parameter**	**Vijlee et al. model [306]**
Inlet	Φ	0.47-0.548	0.44-0.55
	Pressure inlet	107450 Pa gauge	107450 Pa gauge
	Mass flow rate	0.173g/s	0.173g/s
	Temperature	430K	430K
Outlet	Pressure outlet	0 Pa gauge	0 Pa gauge
	Flow direction	y-axis	y-axis
Wall	Heat transfer	Mixed: Convection, radiation, conduction modeled	Constant heat loss 12000w/m^2
	Inner layer	20mm Al_2O_3 ceramic	Not included
	Insulation	10mm- thick Kaowool	Not included

	Metal housing	25mm -thick steel	Not included
	Ext. emissivity	0.8	Not included
	Heat transfer coef.	196.7 W/m^2-K	Not included
Periodicity	Periodic	Rotationally	Rotationally

Table XV. Numerical methods

Model	**1st order (this work)**	**2nd order (this work)**	**Vijlee et al. model**
Grid	3D two-jet domain	3D two-jet domain	3D one-jet domain
Number of cells	312992	312992	309860
Solver	Steady	Steady	Steady
Viscous model	RSM	RSM	RSM
Stress-strain relation	Quadratic	Quadratic	Linear
Near-wall treatment	Scalable wall function	Scalable wall function	Standard wall function
Buoyancy effects	Included	Included	Not included
Reaction model	EDC	EDC	EDC
Diffusion model	Multicomponent	Multicomponent	Not included
Mechanism	Skeletal GRI3.0[295]	Skeletal GRI3.0[295]	Skeletal GRI3.0[295]
Density	Ideal gas	Ideal gas	Ideal gas

Model	**1st order (this work)**	**2nd order (this work)**	**Vijlee et al. model**
Mass diffusivity	Kinetic theory	Kinetic theory	Constant 2.88e-5
Thermal diffusivity	Kinetic theory	Kinetic theory	Kinetic theory
Numerical discretization scheme			
P-V Coupling	Coupled	Coupled	SIMPLE
Pressure	PRESTO!	2nd order	Standard
Momentum	1st order	2nd order	1st order
Density	2nd order	2nd order	1st order
Turbulence	1st order	2nd order	1st order
Species	2nd order	2nd order	1st order
Energy	2nd order	2nd order	1st order

RESULTS AND DISCUSSION

In this steady-state CFD simulation, the operational conditions are varied over a range of ϕ and compared with the experimental data. The flow field is first solved with a transient solver for a non-burning (cold) solution. FIG 53 shows the streamlines colored by velocity magnitude for a transient cold solution. Immediately after the initialization, two counter-rotating vortices form on either side of the jets, see FIG 53(a). The flow at this point is nearly symmetric with respect to the jets position; both poloidal vortices have similar intensities. This flow field is similar to the assumptions made by Briones et al. [307] in their model. The toroidal flow is relatively weak. As the flow develops, two major changes are observed: (i) the toroidal flow component becomes stronger, and (ii) one of the poloidal vortices becomes dominant. The development of the strong toroidal flow component is expected and is described in the earlier TJSR papers as the jets angle drives the

flow in a toroidal direction. FIG 53(b) shows that the strong poloidal recirculation exists only above the air-fuel jets. The flow bifurcation is caused not by the interaction between the jet and the surrounding structures, but by the interaction between the initially counter-rotating vortices. The two vortices are not completely separated by the planar jet, which forms after the individual jets merge; the region in-between the jets allow the vortices to cross-talk. In FIG 53(b), the downward flow from the upper vortex penetrates into the bottom vortex resulting in the formation of the local stagnation region (in the poloidal plane) located below the inlet. Once the bottom vortex is blocked from interaction with the jet, it effectively dies out, and the dominant vortex grows stronger as it entrains the entire mass of the jet. The patterns are similar to the studies of asymmetric jets by Cherdron et al., Lai et al., and Zaman [316-318]. This finding is significant from the standpoint of numerical scheme selection and the description of the combustion stabilization mechanism. The use of the linear stress-strain relation of the eddy-viscosity model is not appropriate for such flow [308]. Based on the CFD results, we hypothesize that a supercritical pitchfork bifurcation happens due to the interaction of the counter-rotating vortices. The parameters that determine the location of the strong recirculation can be influenced by the numerical schemes, buoyancy, number of jets modeled, and so on. In this work, we do not test this hypothesis.

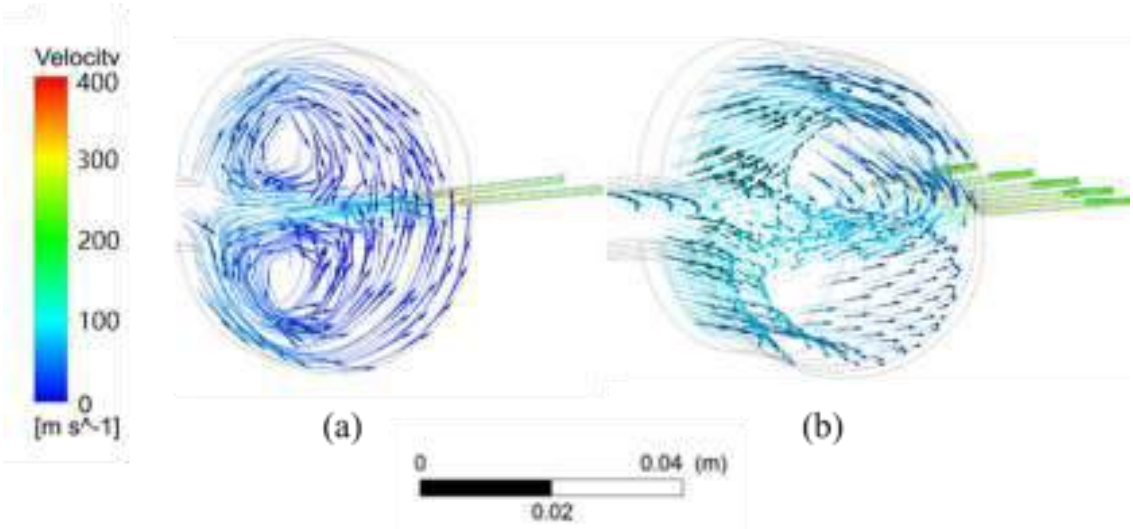

FIG 53: Streamline colored by velocity magnitude for non-combusting flow, second order numerical scheme: (a) Developing flow field, the initial flow field is symmetric with two counter-rotating vortices; the toroidal component is small. (b) Developed flow solution – the toroidal component develops; the penetration of the dominant poloidal vortex reduces the strength of the poloidal recirculation below the jets. The maximum velocity is 376 m/s, which is located at the exit of the nozzles.

After obtaining the cold flow solution with a transient solver, the combustion is initialized by patching the region of high temperature and the model is switched to a steady-state solver. The steady-state solutions are obtained for the range of ϕ, from ϕ=0.548 to the lowest stable burning conditions. FIG 54 shows the streamlines colored by temperature for the entire reactor; for better visualization, the streamlines are translated periodically based on the solution of the modeled 15-degree sector. Strong toroidal direction flow persists in the reactor. PRZ flow penetration into the region below the jets is visible in the transitional zone.

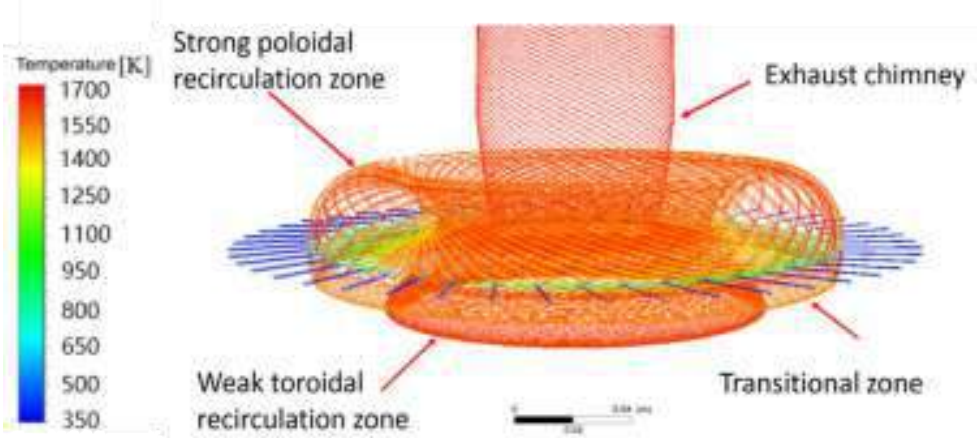

FIG 54: Flow streamlines for stable combustion conditions (ϕ=0.548), colored by temperature. The flow is divided between PRZ and TRZ. The strong recirculation zone shows poloidal and toroidal velocity components of similar magnitude (near 45 degrees streamline direction). The flow from strong PRZ penetrates to TRZ in-between the jets. The maximum temperature is 1667 K and minimum temperature is 351.9 K.

FIG 55 shows the vectors are colored by temperature for a stable combustion simulation. Similar to the cold flow solution, a strong poloidal recirculation exists only above the air-fuel jets. The mixture enters the strong PRZ and has minimum interaction with the TRZ. The average mass flux for the strong recirculation zone is about 22 kg/(m2-s) in toroidal direction and 10.5 kg/(m2-s) in poloidal direction. In the weak recirculation zone, the toroidal flow is about 21kg/(m2-s), and the poloidal flow is 0.03 kg/(m2-s). The toroidal flow component is uniform over the whole TJSR, but the poloidal flow component is much greater in the strong recirculation zone. As in the cold flow solution, the penetration of PRZ flow into the TRZ results in the formation of the asymmetric jet. The entrainment of TRZ gas into the fresh fuel-air mixture is blocked, and only the hot combustion products from PRZ are entrained by the jets. In this scenario, flame stabilization primarily depends on the temperature and gas composition of the strong PRZ. The combustion in the TRZ is sustained

mostly by the escaped gas from the PRZ due to the flow penetration and turbulent diffusion. From a modeling perspective, the selection of the numerical approach is critical to the analysis of the flow patterns in the reactor: the numerical scheme should be able to describe the highly swirling flow of the PRZ and the interaction between the jet and the surrounding flow structures. From the design and application perspective, the choice of the numerical scheme is driven by the computational turn around cycle time and computational cost. However, the easy to converge first order numerical schemes may not be appropriate due to their high numerical viscosity and inadequate pressure-strain relationship for predicting high swirling flows.

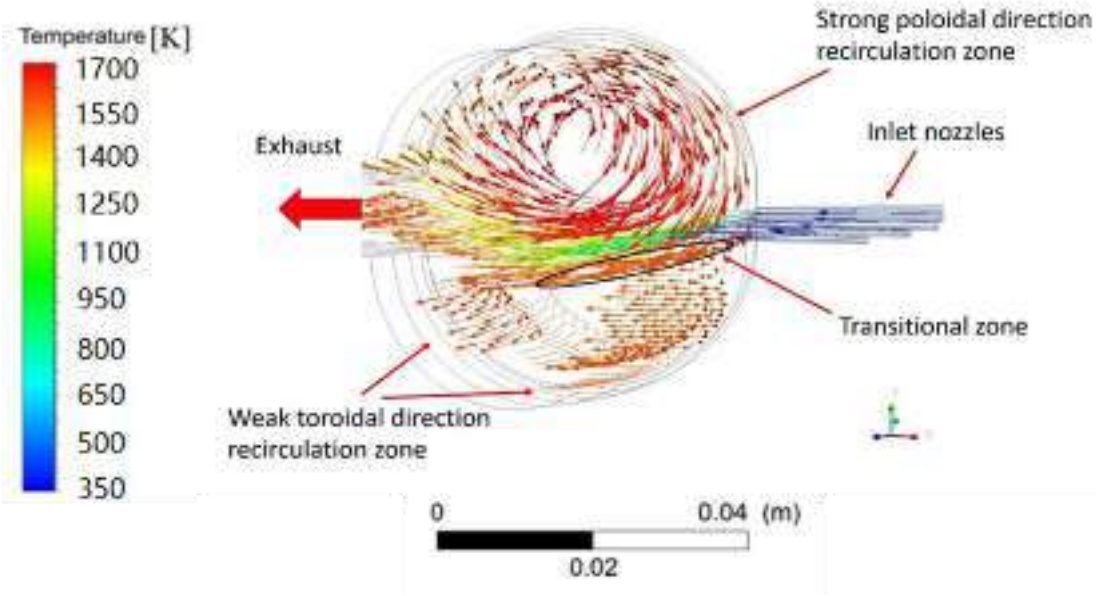

FIG 55: Section view of the toroidal reactor for stable combustion ϕ=0.548, vectors colored by temperature; the strong PRZ displaces the jet downwards. In the transition zone, PRZ flow penetrates between the jets into the TRZ, breaking the coherent poloidal vortex below the jet. The transitional zone sheathes the entrainment of the flow from the TRZ. The maximum temperature is 1667 K and minimum temperature is 351.9 K.

FIG 56 shows the temperature contours on a periodic plane for first and second order schemes under a stable combustion condition (top) and approaching LBO (bottom). Both numerical schemes show large temperature gradients between the PRZ and the TRZ near blowout. The first order scheme has more defined flow structures for both conditions due to the added numerical viscosity in the turbulence equation. The added numerical viscosity tends to reduce the gradients and thus the turbulent kinetic energy (k) production, which is likely to result in reduced turbulent diffusion. For example, the jet penetration is better defined in the lower order simulation; the first order shows four distinct jets on a periodic plane vs. two for the second order scheme. Furthermore, when approaching the blowout, the lower order solution has a well-defined stabilization vortex, which explains the increased flame stability of the lower order numerical scheme. FIG

56 also indicates the jet-jet interaction modeled by the two-jet system. There are at least 3 cold pockets in the cross-section indicating the entrainment of jets, while a similar figure (Figure 11) in previous work [306] does not show the jet-jet interaction clearly.

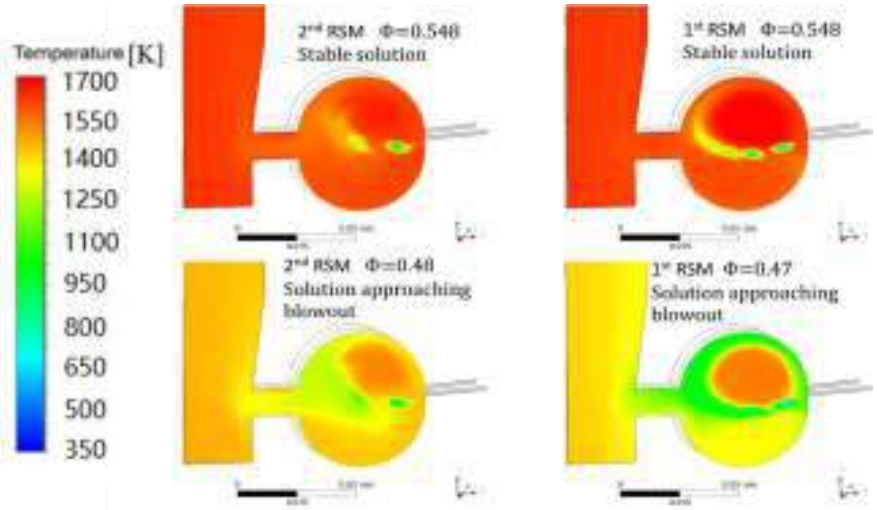

FIG 56: Temperature contours for the stable solution and solution at the incipient LBO. The higher ϕ (top panel) shows more uniform temperature fields. The lowest stable ϕ is 0.48 for second order scheme and 0.47 for the first order scheme (bottom panel). The maximum temperature is 1667 K, and the minimum temperature is 351.9 K.

FIG 57 shows the maximum temperature ratio of PRZ to TRZ. At stable combustion conditions, the ratio is nearly constant. The temperature ratio increases non-linearly approaching blowout, which is associated with the cooling of a less intense TRZ. In general, the first order scheme simulations have a greater ratio than the second order scheme, which agrees with the earlier observation that the first order has less mixing due to the increased numerical viscosity.

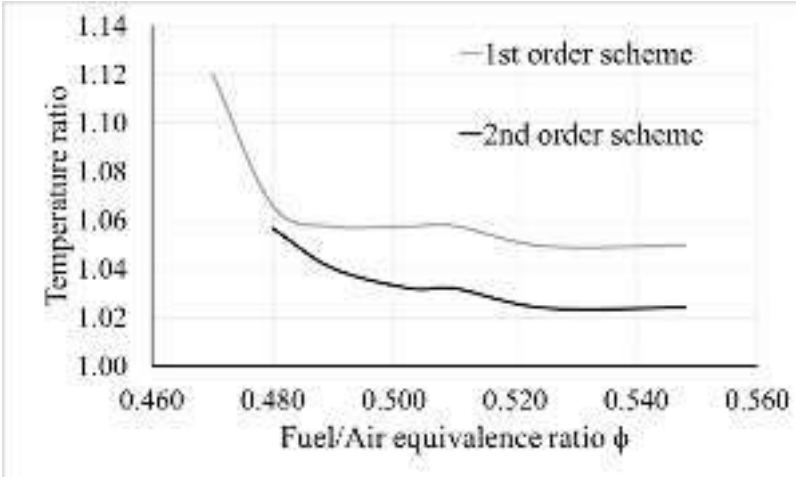

FIG 57: Ratio of maximum temperatures (T_{PRZ}/T_{TRZ}). The first order scheme shows a greater difference. For both schemes, the ratio increases approaching blowout due to a nonlinear temperature decrease in TRZ.

FIG 58 compares modeling results from this and the previous study to the data of Vijlee et al. Experimental temperature measurements are taken "roughly 5 mm above the bottom wall of the TJSR" [305]. The temperature from the CFD solution corresponds to the same location—5 mm from the lower TJSR wall. All CFD solutions consistently under-predict the experimental data by 20-40 K, possibly due to the numerical diffusivity of the models, the ambiguity of the temperature measurement location, thermocouple correction calculation, or uncertainties in the mass flow rate calculations. Though the absolute temperature from CFD does not match experiments perfectly, the trend matches well and can be used for the analysis of flame stability. The model of Vijlee et al. shows the closest agreement with the experimental temperature measurement with the location of the hot stabilizing vortex in the lower part of the TJSR (the gravity was not included in the previous study. These results do not have good agreement with the experimental blowout conditions, showing a stable solution for ϕ values as low as 0.45. The discrepancy can be attributed to the approximation in the heat transfer model, the added numerical viscosity of the low order numerical schemes, and the absence of the jet-jet interaction in the single nozzle reactor domain, and other numerical approximations, see Table 2. In the previous model, a simplified approach to heat transfer is used: a constant wall temperature and 2.5% heat loss to the reactor wall [306]. The solution did capture the wall temperature variation. In our model, convection, radiation, and shell conduction are included; the local wall temperatures and overall heat loss are computed explicitly. Our CFD simulations show a similar trend between temperature and ϕ in the stable combustion region. The temperature decreases linearly from a high ϕ value down to the experimental blowout

point ($\phi \approx 0.5$). The nonlinear CFD trend approaching blowout is due to the temperature decrease of the TRZ.

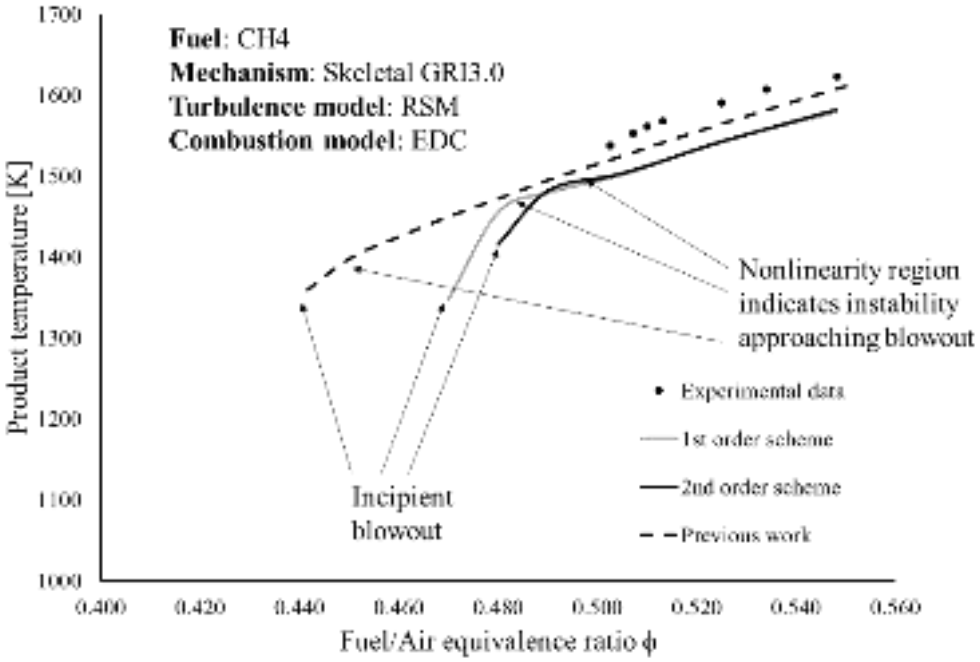

FIG 58: Temperature comparison of the experimental data and numerical solution. The CFD temperature is taken 5 mm from the wall of the lower toroid; the CFD temperature is lower than the data by 20-40K for all stable experimental conditions. The CFD solution shows a nonlinear trend in the region below the experimental LBO associated with the TRZ cooling. The first order scheme sustains combustion at a lower ϕ.

FIG 59 shows the contours of the species mass fraction for first and second order schemes under a stable combustion condition and the leanest stable conditions. Similar to the temperature profiles, the species profiles from the lower order calculations are less uniform owing to the added numerical viscosity. The first order scheme shows a better-defined flame region indicated by the maximum CO concentrations, as well as the flame stabilization vortex indicated by the maximum values of the OH radical. The turbulent diffusion of the second order scheme allows the species to populate the TRZ, especially approaching LBO conditions where the chemical reaction time increases while the mixing time stays relatively constant. FIG 59 shows that the higher CO concentration for the first order scheme is about 0.014 kg_{CO}/kg_{total} and only 0.01 kg_{CO}/kg_{total} for the second order scheme. The high concentration of CO in the TRZ for near blowout conditions suggest a quenched CO oxidation, which is typically associated with local blowout conditions.

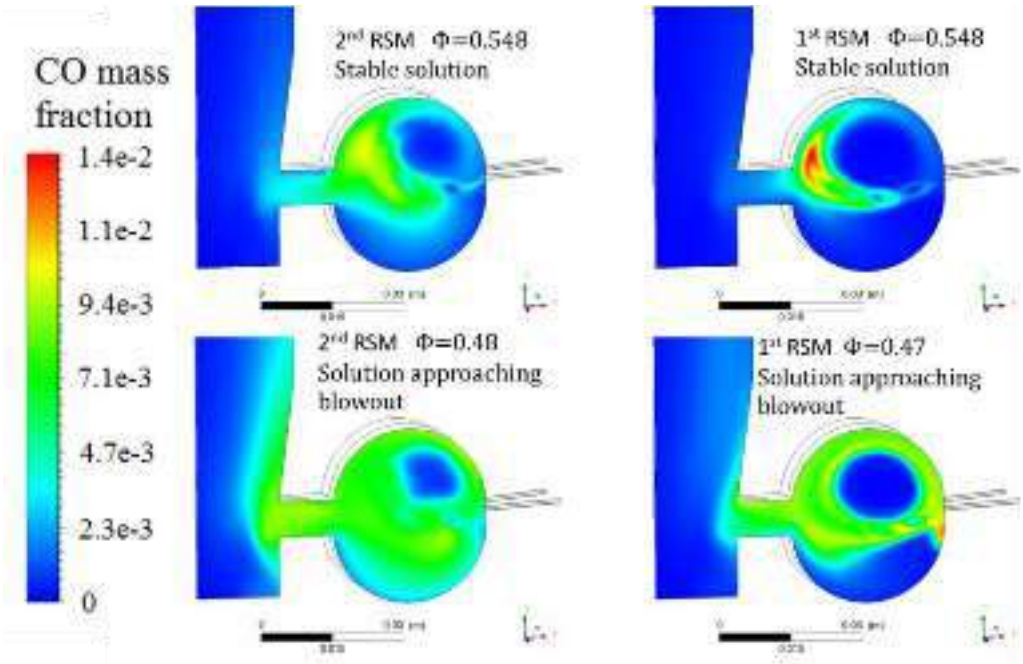

FIG 59: The CO mass fraction contours of a stable solution and at the incipient blowout. The first order solution shows more defined regions with high concentrations of CO at stable conditions. The lower ϕ solutions show significantly higher and more uniform CO concentrations in the weak recirculation zone due to the increased chemical time constant.

FIG 60 shows the OH-radical mass fraction; the second order scheme has higher dissipation of OH-radicals, which agrees with the previous discussion that the recirculation zones in the second order simulation have more interaction than in the less diffusive lower order scheme. The maximum values of the OH-radical mass fraction in the flame stabilizing structure at blowout conditions is about 7e-4 kg_{OH}/kg_{total} or about 0.1% by volume. The OH-radical blowout threshold values are independent of the numerical scheme. One approach is to consider the average OH concentration in the domain as a criterion for a blowout. The average OH for stable solutions (ϕ =0.548) is 4.35e-4 kg_{OH}/kg_{total} and 5.78e-4 kg_{OH}/kg_{total} for first and second order schemes, respectively. The average OH for solutions approaching blowout is 2.17e-4 kg_{OH}/kg_{total} and 2.97e-4 kg_{OH}/kg_{total} for first and second order schemes, respectively. The average value of OH reduced when approaching the LBO; this may provide useful criteria for proximity to LBO. However, the criteria do not account for the spatial distribution of the OH radical within the reactor and are limited, as shown in the PSR analysis of Vijlee et al. [306]

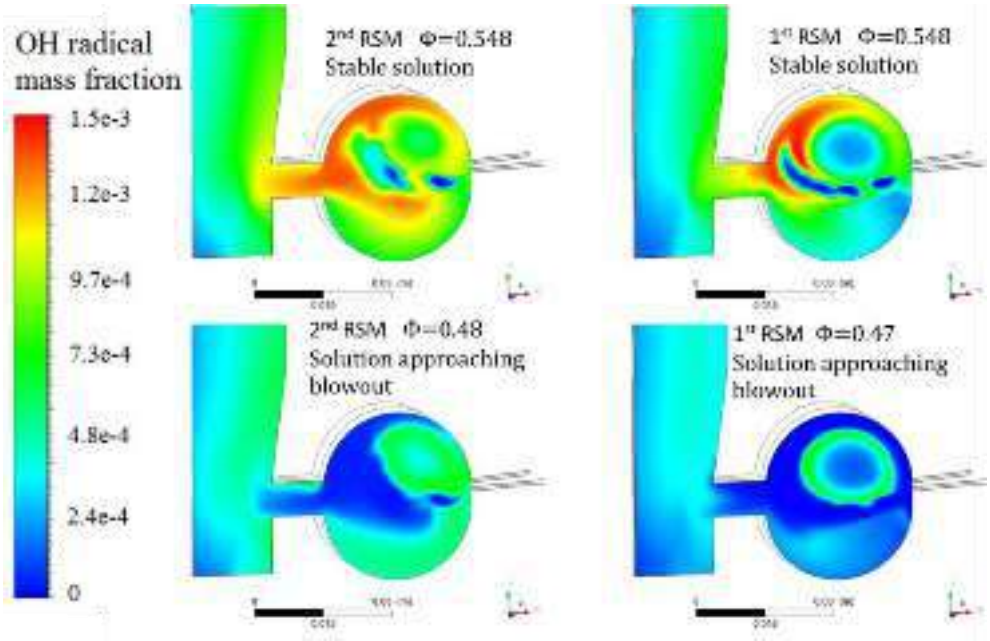

FIG 60: The OH-radical mass fraction contours of a stable solution and at an incipient blowout. The higher ϕ shows higher OH concentrations; the first order solution shows lower concentrations in TRZ. The maximum OH mass fraction at the incipient blowout for both schemes is about 7e-4 kg_{OH}/kg_{total}.

FIG 61 shows the maximum computed species mass fraction as a function of ϕ; the concentrations decrease with ϕ. The trend of decay is comparable to the levels shown in DePape et al.[319] The threshold concentrations at the blowout are independent of the convergence scheme. The second order scheme shows nonlinear behavior for $\phi<0.5$ indicating a high-temperature gradient, thus the non-uniform combustion chemistry rates between the PRZ and the TRZ.

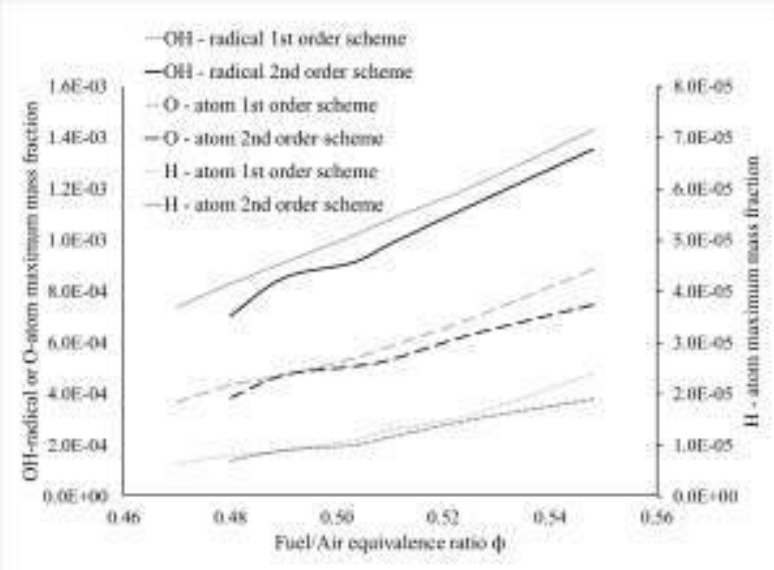

FIG 61: Maximum species mass fraction versus ϕ for OH radical, O-atom, and H-atom.

FIG 62 and FIG 63 show the local *Da* number for considered cases. The *Da* number is calculated as the ratio of the turbulent time scale $\tau_T = l_0 / v'_{rms}$ to the characteristic chemical time scale $\tau_{chem} = \delta_L / S_L$, where l_0 is the extreme of the length-scale spectrum characterizing the largest eddy sizes, v'_{rms} is the root-mean-square of the turbulent velocity fluctuations related to turbulent kinetic energy, δ_L is the laminar flame thickness, and S_L is the laminar flame speed for premixed methane combustion [270], The turbulent time scale is based on turbulent kinetic energy calculated by the CFD, and the chemical time scale is based on the laminar flame speed of the lean premixed methane/air fuel [320,321]. Previously, Koutmos et al. suggested that the local *Da* number needs to be greater than the critical *Da* number for stable combustion [322]. The threshold (critical) *Da* number in our simulations in the flame stabilizing zone is in the range of 0.2-0.3. For the reactors where the well-stirred conditions are met, such as in this case, the flow field can be described by the local parameters; here the *Da* number can be obtained from the local properties calculated using CFD. The *Da* number definition can be modified as shown by previous researchers [322,323]. The local *Da* number in the TRZ is an order of magnitude less than the *Da* in the flow stabilizing region. At ϕ ~0.5-0.52, the *Da* levels in TRZ fall below the values of 0.1; at the same ϕ, the temperature and species concentration in this region exhibit nonlinear trends. We conclude that the TRZ cannot sustain combustion by itself and is likely to result in local flame extinction events, which, by themselves, do not result in the global blowout in the CFD simulation. The flame front *Da* is

calculated for the location of maximum CO concentration, as shown in FIG 59. The flame front *Da* monotonically decreases with ϕ; the stable experimental conditions (ϕ > 0.5-0.51), Da_{flame} < 0.1 which not sufficient to sustain combustion by itself, additional flame stabilization (entrainment of recirculating gas) is required for TJSR combustion.

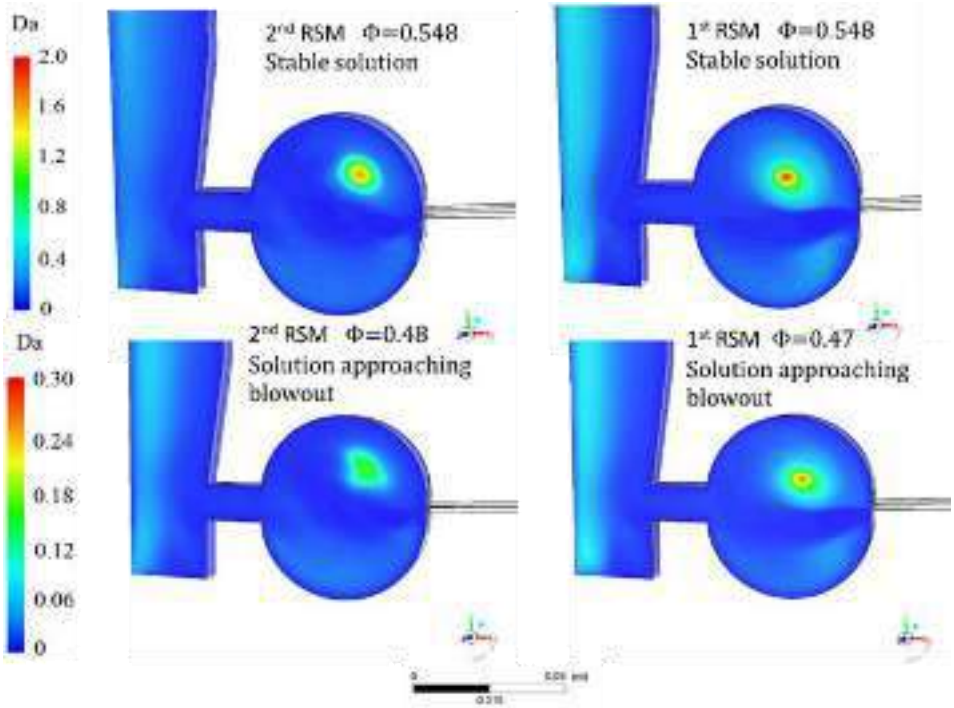

FIG 62: *Da* number contours of a stable solution and at the incipient LBO. The maximum *Da* in the PRZ.

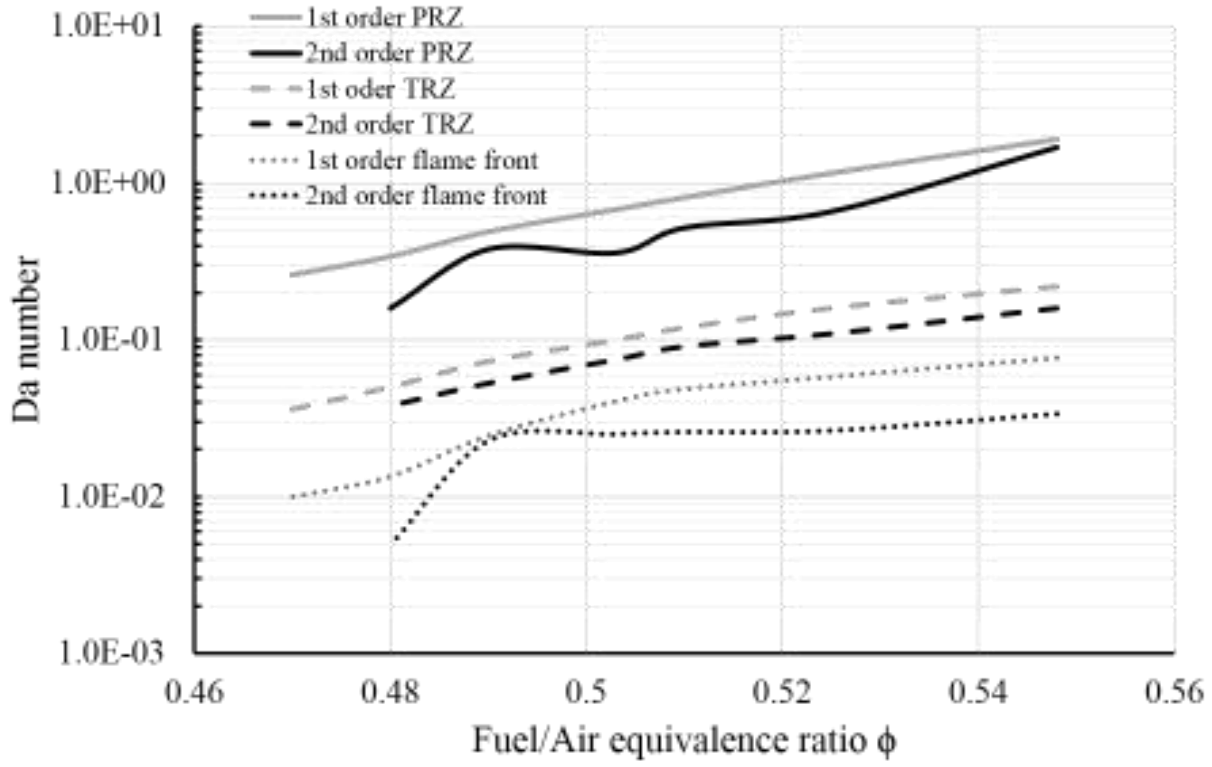

FIG 63: Maximum *Da* number vs. ϕ for the first and second order scheme in the PRZ and TRZ. The *Da* number decreases for leaner combustion; the *Da* number in TRZ is an order of magnitude lower, indicating that the PRZ provides a more stable flame structure. At LBO, Da_{PRZ} ~ 0.2-0.3, Da_{TRZ} ~0.03- 0.04, Da_{flame} ~0.005-0.01.

CONCLUSIONS

Atmospheric-pressure TJSR is studied using 3D CFD; the computational domain includes a two-jet sector (out of 48) with periodic boundary conditions to capture the jet-jet interaction. The solutions for first and second order steady-state numerical schemes over a range of ϕ from 0.55 to LBO are compared with the experimental data. Compared to the previous studies, this study employs higher order convergence schemes; the heat transfer model accounts for convective and radiative mechanisms and conduction through the reactor wall. The quadratic stress-strain relations with the RSM turbulence closure and EDC model with a skeletal mechanism are used. The modeling gains insight into the LBO mechanism of the TJSR and allows for some generalizations of the flow behavior in aerodynamically stabilized reactors. The conclusions of this work are as follows:

The steady-state numerical solution shows the formation of a strong poloidal recirculation and weak toroidal recirculation zones. The interaction between the two (initially counter-rotating)

vortices results in the formation of the local stagnation region (in the poloidal plane) in one of the vortices, breaking down its coherent structure and leading to a loss of the vorticity in the poloidal plane. The toroidal reactor is not well-stirred as suggested in the previous literature, large temperature and species gradient exist for all investigated condition.

Due to the penetration of the strong PRZ flow into the weak vorticity region, the entrainment from the TRZ is limited; flame stabilization depends on gas entrainment from the PRZ. The ability to model the high swirling flow in the flame stabilizing recirculation region is critical for the analysis of the LBO mechanism.

The first order solution shows more defined PRZ with a higher concentration of free radical species for the same ϕ. The presence of this region in the steady-state simulation (which does not consider the jet instability) leads to combustion stabilization at a lower overall ϕ. The second order scheme does not sustain this well-defined vortex yielding more uniform temperature and species distribution in the reactor.

Maximum concentrations of the major free radicals in the PRZ at the incipient blowout are: OH – 0.07 kg_{OH}/kg_{total}, O-atom - 0.037 kg_{O}/kg_{total}, and H-atom – 0.0006 kg_{H}/kg_{total}; the maximum temperature is 1510 K. Although the shape of the flame and the recirculation zone and the interaction between flow structures may be different, the threshold level of free radicals for sustained combustion is found to be independent of the numerical scheme.

The *Da* number in the stabilization zone can be considered as the critical blowout parameter. At the LBO conditions the maximum $Da_{PRZ} \sim 0.2\text{-}0.3$, $Da_{flame} \sim 0.005$, $Da_{TRZ} \sim 0.04$. We conclude that unassisted fuel-air jet or TRZ cannot sustain combustion by itself resulting in local flame extinction, which agrees with the experimental results of Barat who reported that the local blowout events were observed before the global blowout. The local blowout events are likely to be accompanied by the flame movement and negative feedback on the stability of the PRZ vortex, leading to reactor blowout at a higher fuel equivalence ratio than predicted by the CFD.

Though the validity of the turbulence and combustion models used in the study may be sources for discrepancies between numerical prediction and experiments, and needs further investigation; the flow field analysis for both schemes suggests that the use of the local parameters for LBO prediction is a promising approach.

Some general conclusions can be made based on the CFD simulations and experimental observations of the TJSR. For aerodynamically stabilized combustors with opposing recirculation zones, a dominant flow structure with faster mixing and faster overall combustion chemistry may develop. Poor mixing and slower chemistry in the weak recirculation zone lead to incomplete combustion, high UHC and CO emissions, and poor carbon conversion efficiency. Due to high numerical viscosity, low order numerical simulations are not well-suited for studies of the blowout due to their inability to capture mixing behavior in the shear layer between the jet and stabilizing vortex. While the critical *Da* number may be a good indicator for assessing proximity to the blowout, a high *Da* number non-uniformity in the combustor may result in local flame blowouts, flame instability leading to global LBO before the critical *Da* number is reached.

Nomenclature for Appendix D

CFD	Computational fluid dynamics
Cp	Specific heat
Da	Damkohler number
EBU	Eddy breakup model
EDC	Eddy dissipation concept
k	Turbulent kinetic energy
LBO	Lean blowout
PRZ	Poloidal recirculation zone
P-V	Pressure-Velocity
TJSR	Toroidal jet-stirred reactor
RANS	Reynolds averaged Navier-Stokes
RSM	Reynolds stress model
TRZ	Toroidal recirculation zone
Φ	Fuel-air equivalence ratio

τ	Characteristic time scale
ρ	Mean density

BIBLIOGRAPHY

1 Yang, F. *et al.* in *XIIIth International Symposium on High Voltage Engineering.*

2 Jewell-Larsen, N., Zhang, P., Hsu, C.-P., Krichtafovitch, I. & Mamishev, A. in *9th AIAA/ASME Joint Thermophysics and Heat Transfer Conference.* 3607 (AIAA).

3 Seyed-Yagoobi, J. & Owsenesk, B. Theoretical and experimental study of electrohydrodynamic heat transfer enhancement through wire-plate corona discharge. *Journal of Heat Transfer* **119**, 604-610 (1997).

4 Go, D. B., Maturana, R. A., Fisher, T. S. & Garimella, S. V. Enhancement of external forced convection by ionic wind. *International Journal of Heat and Mass Transfer* **51**, 6047-6053 (2008).

5 Jewell-Larsen, N. *et al.* CFD analysis of electrostatic fluid accelerators for forced convection cooling. *IEEE Transactions on Dielectrics and Electrical Insulation* **15** (2008).

6 Schmatloch, V. & Rauch, S. Design and characterisation of an electrostatic precipitator for small heating appliances. *Journal of electrostatics* **63**, 85-100 (2005).

7 Stuetzer, O. M. Ion drag pressure generation. *Journal of Applied Physics* **30**, 984-994 (1959).

8 Krichtafovitch, I., Gorobets, V., Karpov, S. & Mamishev, A. in *Annual Meeting of the Electrostatics Society of America.* 1-13.

9 Jewell-Larsen, N., Parker, D., Krichtafovitch, I. & Mamishev, A. in *Electrical Insulation and Dielectric Phenomena, 2004. CEIDP'04. 2004 Annual Report Conference on.* 106-109 (IEEE).

10 Wen, T.-Y., Shen, T.-T., Wang, H.-C. & Mamishev, A. in *Electronic Components and Technology Conference (ECTC), 2013 IEEE 63rd.* 240-246 (IEEE).

11 Ju, Y. & Sun, W. Plasma assisted combustion: Dynamics and chemistry. *Progress in Energy and Combustion Science* **48**, 21-83 (2015).

12 Moreau, E. Airflow control by non-thermal plasma actuators. *Journal of physics D: applied physics* **40**, 605 (2007).

13 Roth, J. R. Aerodynamic flow acceleration using paraelectric and peristaltic electrohydrodynamic effects of a one atmosphere uniform glow discharge plasma. *Physics of plasmas* **10**, 2117-2126 (2003).

14 Choi, K.-S., Jukes, T. & Whalley, R. Turbulent boundary-layer control with plasma actuators. *Philosophical Transactions of the Royal Society of London A: Mathematical, Physical and Engineering Sciences* **369**, 1443-1458 (2011).

15 Kunhardt, E. E. & Luessen, L. H. Electrical Breakdown and Discharges in Gases-Part B, Macroscopic Processes and Discharges. *Eds. EE Kunhardt and LH Luessen, Plenum, NY* (1981).

16 Mukkavilli, S., Lee, C., Varghese, K. & Tavlarides, L. Modeling of the electrostatic corona discharge reactor. *IEEE transactions on plasma science* **16**, 652-660 (1988).

17 Chang, J.-S., Lawless, P. A. & Yamamoto, T. Corona discharge processes. *IEEE Transactions on plasma science* **19**, 1152-1166 (1991).

18 Townsend, J. S. XI. The potentials required to maintain currents between coaxial cylinders. *The London, Edinburgh, and Dublin Philosophical Magazine and Journal of Science* **28**, 83-90 (1914).

19 Townsend, J. S. *Electricity in gases*. (Рипол Классик, 1915).

20 Sigmond, R. Simple approximate treatment of unipolar space‐charge‐dominated coronas: The Warburg law and the saturation current. *Journal of Applied Physics* **53**, 891-898 (1982).

21 Yamada, K. An empirical formula for negative corona discharge current in point-grid electrode geometry. *Journal of applied physics* **96**, 2472-2475 (2004).

22 Wais, S. I. & Giliyana, D. D. Sphere-to-plane electrodes configuration of positive and negative plasma corona discharge. *Am J Mod Phys* **2**, 46-52 (2013).

23 Mikropoulos, P. & Zagkanas, V. in *Proceeding of the 16 th International Symposium on High Voltage Engineering. Paper B-10.*

24 Zheng, Y., Zhang, B. & He, J. Current-voltage characteristics of dc corona discharges in air between coaxial cylinders. *Physics of Plasmas* **22**, 023501 (2015).

25 Martins, A. A. Simulation of a wire-cylinder-plate positive corona discharge in nitrogen gas at atmospheric pressure. *Physics of Plasmas* **19**, 063502 (2012).

26 Giubbilini, P. The current‐voltage characteristics of point‐to‐ring corona. *Journal of applied physics* **64**, 3730-3732 (1988).

27 Giubbilini, P. Mobility measurement of large ions in air from a point-to-ring corona source. *Journal of applied physics* **81**, 2101-2104 (1997).

28 Zhang, Y., Liu, L., Chen, Y. & Ouyang, J. Characteristics of ionic wind in needle-to-ring corona discharge. *Journal of Electrostatics* **74**, 15-20 (2015).

29 Dau, V. T. *et al.* Corona based air-flow using parallel discharge electrodes. *Experimental Thermal and Fluid Science* **79**, 52-56 (2016).

30 Johnson, M. J., Tirumala, R. & Go, D. B. Analysis of geometric scaling of miniature, multi-electrode assisted corona discharges for ionic wind generation. *Journal of Electrostatics* **74**, 8-14 (2015).

31 Tirumala, R. & Go, D. B. Comparative study of corona discharge simulation techniques for electrode configurations inducing non-uniform electric fields. *Journal of Electrostatics* **72**, 99-106 (2014).

32 Guan, Y., Vaddi, R. S., Aliseda, A. & Novosselov, I. Analytical model of electro-hydrodynamic flow in corona discharge. *Physics of plasmas* **25**, 083507 (2018).

33 Sigmond, R. & Goldman, M. Electrical Breakdown and Discharges in Gases-Part B, Macroscopic Processes and Discharges. *Eds. EE Kunhardt and LH Luessen, Plenum, NY* (1981).

34 Meng, X., Zhang, H. & Zhu, J. A general empirical formula of current–voltage characteristics for point-to-plane geometry corona discharges. *Journal of Physics D: Applied Physics* **41**, 065209 (2008).
35 Yanallah, K. & Pontiga, F. A semi-analytical stationary model of a point-to-plane corona discharge. *Plasma Sources Science and Technology* **21**, 045007 (2012).
36 Chen, S., Nobelen, J. & Nijdam, S. A self-consistent model of ionic wind generation by negative corona discharges in air with experimental validation. *Plasma Sources Science and Technology* **26**, 095005 (2017).
37 Yanallah, K., Pontiga, F., Meslem, Y. & Castellanos, A. An analytical approach to wire-to-cylinder corona discharge. *Journal of Electrostatics* **70**, 374-383 (2012).
38 Bouazza, M., Yanallah, K., Pontiga, F. & Chen, J. A simplified formulation of wire-plate corona discharge in air: Application to the ion wind simulation. *Journal of Electrostatics* **92**, 54-65 (2018).
39 Moreau, E., Benard, N., Lan-Sun-Luk, J.-D. & Chabriat, J.-P. Electrohydrodynamic force produced by a wire-to-cylinder dc corona discharge in air at atmospheric pressure. *Journal of Physics D: Applied Physics* **46**, 475204 (2013).
40 Robinson, M. Movement of air in the electric wind of the corona discharge. *Transactions of the American Institute of Electrical Engineers, Part I: Communication and Electronics* **80**, 143-150 (1961).
41 Belhadj, C., Shwehdi, M. & Farag, A. in *Electrical Insulation and Dielectric Phenomena, 1998. Annual Report. Conference on.* 489-492 (IEEE).
42 Li, L., Lee, S. J., Kim, W. & Kim, D. An empirical model for ionic wind generation by a needle-to-cylinder dc corona discharge. *Journal of Electrostatics* **73**, 125-130 (2015).
43 Adamiak, K. & Atten, P. Simulation of corona discharge in point–plane configuration. *Journal of electrostatics* **61**, 85-98 (2004).
44 Zhao, L. & Adamiak, K. EHD flow in air produced by electric corona discharge in pin–plate configuration. *Journal of electrostatics* **63**, 337-350 (2005).
45 Zhao, L. & Adamiak, K. Numerical simulation of the effect of EHD flow on corona discharge in compressed air. *IEEE Transactions on Industry Applications* **49**, 298-304 (2013).
46 Lawless, P. & Sparks, L. Interactive computer model for calculating VI curves in ESPs (electrostatic precipitators): Version 1. 0. Report for July 1984-July 1986. (Research Triangle Inst., Durham, NC (USA), 1986).
47 Cristina, S., Dinelli, G. & Feliziani, M. Numerical computation of corona space charge and VI characteristic in DC electrostatic precipitators. *IEEE Transactions on industry applications* **27**, 147-153 (1991).
48 Yamamoto, T., Okuda, M. & Okubo, M. Three-dimensional ionic wind and electrohydrodynamics of tuft/point corona electrostatic precipitator. *IEEE Transactions on Industry Applications* **39**, 1602-1607 (2003).
49 Adamiak, K. Numerical models in simulating wire-plate electrostatic precipitators: A review. *Journal of Electrostatics* **71**, 673-680, doi:10.1016/j.elstat.2013.03.001 (2013).
50 Go, D. B., Garimella, S. V. & Fisher, T. S. in *Thermal and Thermomechanical Phenomena in Electronics Systems, 2006. ITHERM'06. The Tenth Intersociety Conference on.* 45-53 (IEEE).
51 Go, D. B., Garimella, S. V., Fisher, T. S. & Mongia, R. K. Ionic winds for locally enhanced cooling. *Journal of Applied Physics* **102**, 053302 (2007).
52 Kaptsov, N. A. (Gostehizdat, Moscow, 1950).
53 Peek, F. The law of corona and the dielectric strength of air. *Proceedings of the American Institute of Electrical Engineers* **30**, 1485-1561 (1911).
54 Moralev, I., Sherbakova, V., Selivonin, I., Bityurin, V. & Ustinov, M. Effect of the discharge constriction in DBD plasma actuator on the laminar boundary layer. *International Journal of Heat and Mass Transfer* **116**, 1326-1340 (2018).
55 Gan, T. *et al.* Shock wave boundary layer interaction controlled by surface arc plasma actuators. *Physics of Fluids* **30**, 055107 (2018).
56 Zhang, X. *et al.* Turbulent boundary layer separation control using plasma actuator at Reynolds number 2000000. *Chinese Journal of Aeronautics* **29**, 1237-1246 (2016).
57 Dörr, P. & Kloker, M. Transition control in a three-dimensional boundary layer by direct attenuation of nonlinear crossflow vortices using plasma actuators. *International Journal of Heat and Fluid Flow* **61**, 449-465 (2016).
58 Zheng, J., Li, J., Zhao, Z., Cui, Y. & Khoo, B. Numerical Study of Nanosecond Pulsed Plasma Actuator in Laminar Flat Plate Boundary Layer. *Communications in Computational Physics* **20**, 1424-1442 (2016).
59 Ginzburg, I. Prediction of the moments in advection-diffusion lattice Boltzmann method. II. Attenuation of the boundary layers via double-Λ bounce-back flux scheme. *Physical Review E* **95**, 013305 (2017).
60 Pescini, E., Marra, F., De Giorgi, M., Francioso, L. & Ficarella, A. Investigation of the boundary layer characteristics for assessing the DBD plasma actuator control of the separated flow at low Reynolds numbers. *Experimental Thermal and Fluid Science* **81**, 482-498 (2017).
61 Sontag, J. M., Gordeyev, S., Duong, A., Thomas, F. O. & Corke, T. C. in *AIAA Scitech 2019 Forum.* 0468.
62 Ketcham, J. & Velkoff, H. R. Effect of an electrostatic field on boundary- layer transition. *AIAA Journal* **6**, 1381-1383, doi:10.2514/3.4756 (1968).
63 Hussaini, M. Y., Malik, M. R. & Weinstein, L. M. (1983).
64 Soetomo, F., Colver, G. M. & Forouraghi, K. Micro-force measurement of drag on a small flat plate in the presence of a corona discharge. *Journal of Electrostatics* **64**, 525-530, doi:10.1016/j.elstat.2005.10.006 (2006).
65 Roth, J., Sherman, D. & Wilkinson, S. in *36th AIAA Aerospace Sciences Meeting and Exhibit.* 328.
66 Léger, L., Moreau, E., Artana, G. & Touchard, G. Influence of a DC corona discharge on the airflow along an inclined flat plate. *Journal of Electrostatics* **51**, 300-306, doi:10.1016/S0304-3886(01)00089-4 (2001).
67 Léger, L., Moreau, E. & Touchard, G. <xocs:firstpage xmlns:xocs=""/> (2002).
68 Moreau, E., Léger, L. & Touchard, G. Effect of a DC surface-corona discharge on a flat plate boundary layer for air flow velocity up to 25 m/s. *Journal of electrostatics* **64**, 215-225 (2006).
69 Blasius, H. *Grenzschichten in Flüssigkeiten mit kleiner Reibung*. (Druck von BG Teubner, 1907).
70 Cousteix, T. C. J. (Springer, 2005).
71 Schlichting, H. & Gersten, K. *Boundary-layer theory*. (Springer, 2016).
72 Malraison, B. & Atten, P. Chaotic behavior of instability due to unipolar ion injection in a dielectric liquid. *Physical Review Letters* **49**, 723 (1982).

73 Castellanos, A. & Atten, P. Numerical modeling of finite amplitude convection of liquids subjected to unipolar injection. *IEEE transactions on industry applications*, 825-830 (1987).
74 Traoré, P. & Pérez, A. Two-dimensional numerical analysis of electroconvection in a dielectric liquid subjected to strong unipolar injection. *Physics of Fluids* **24**, 037102 (2012).
75 Kwak, R., Pham, V. S., Lim, K. M. & Han, J. Shear flow of an electrically charged fluid by ion concentration polarization: scaling laws for electroconvective vortices. *Physical review letters* **110**, 114501 (2013).
76 Traoré, P. & Wu, J. On the limitation of imposed velocity field strategy for Coulomb-driven electroconvection flow simulations. *Journal of Fluid Mechanics* **727** (2013).
77 Wu, J., Traoré, P., Vázquez, P. A. & Pérez, A. T. Onset of convection in a finite two-dimensional container due to unipolar injection of ions. *Physical Review E* **88**, 053018 (2013).
78 Davidson, S. M., Andersen, M. B. & Mani, A. Chaotic induced-charge electro-osmosis. *Physical review letters* **112**, 128302 (2014).
79 Pérez, A., Vázquez, P., Wu, J. & Traoré, P. Electrohydrodynamic linear stability analysis of dielectric liquids subjected to unipolar injection in a rectangular enclosure with rigid sidewalls. *Journal of Fluid Mechanics* **758**, 586-602 (2014).
80 Rubinstein, I. & Zaltzman, B. Equilibrium electroconvective instability. *Physical review letters* **114**, 114502 (2015).
81 Zhang, M., Martinelli, F., Wu, J., Schmid, P. J. & Quadrio, M. Modal and non-modal stability analysis of electrohydrodynamic flow with and without cross-flow. *Journal of Fluid Mechanics* **770**, 319-349 (2015).
82 Traore, P., Wu, J., Louste, C., Vazquez, P. A. & Perez, A. T. Numerical study of a plane poiseuille channel flow of a dielectric liquid subjected to unipolar injection. *IEEE Transactions on Dielectrics and Electrical Insulation* **22**, 2779-2785 (2015).
83 Wu, J. & Traoré, P. A finite-volume method for electro-thermoconvective phenomena in a plane layer of dielectric liquid. *Numerical Heat Transfer, Part A: Applications* **68**, 471-500 (2015).
84 Wu, J., Perez, A. T., Traore, P. & Vazquez, P. A. Complex flow patterns at the onset of annular electroconvection in a dielectric liquid subjected to an arbitrary unipolar injection. *IEEE Transactions on Dielectrics and Electrical Insulation* **22**, 2637-2645 (2015).
85 Wu, J., Traoré, P., Pérez, A. T. & Vázquez, P. A. On two-dimensional finite amplitude electro-convection in a dielectric liquid induced by a strong unipolar injection. *Journal of Electrostatics* **74**, 85-95 (2015).
86 Zhang, M. Weakly nonlinear stability analysis of subcritical electrohydrodynamic flow subject to strong unipolar injection. *Journal of Fluid Mechanics* **792**, 328-363 (2016).
87 Luo, K., Wu, J., Yi, H.-L. & Tan, H.-P. Lattice Boltzmann model for Coulomb-driven flows in dielectric liquids. *Physical Review E* **93**, 023309 (2016).
88 Luo, K., Wu, J., Yi, H.-L. & Tan, H.-P. Three-dimensional finite amplitude electroconvection in dielectric liquids. *Physics of Fluids* **30**, 023602 (2018).
89 Luo, K., Wu, J., Yi, H.-L., Liu, L.-H. & Tan, H.-P. Hexagonal convection patterns and their evolutionary scenarios in electroconvection induced by a strong unipolar injection. *Physical Review Fluids* **3**, 053702 (2018).
90 Luo, K., Li, T.-F., Wu, J., Yi, H.-L. & Tan, H.-P. Mesoscopic simulation of electrohydrodynamic effects on laminar natural convection of a dielectric liquid in a cubic cavity. *Physics of Fluids* **30**, 103601 (2018).
91 Chandrasekhar, S. *Hydrodynamic and hydromagnetic stability*. (Courier Corporation, 2013).
92 Drazin, P. G. & Reid, W. H. *Hydrodynamic stability*. (Cambridge university press, 2004).
93 Koschmieder, E. L. *Bénard cells and Taylor vortices*. (Cambridge University Press, 1993).
94 Bergé, P. & Dubois, M. Rayleigh-bénard convection. *Contemporary Physics* **25**, 535-582 (1984).
95 Krishnan, M., Ugaz, V. M. & Burns, M. A. PCR in a Rayleigh-Benard convection cell. *Science* **298**, 793-793 (2002).
96 Getling, A. V. *Rayleigh-B nard Convection: Structures and Dynamics*. Vol. 11 (World Scientific, 1998).
97 Marangoni, C. *Sull'espansione delle goccie d'un liquido galleggianti sulla superfice di altro liquido*. (1865).
98 Gibbs, J. W. On the equilibrium of heterogeneous substances. (1879).
99 Velarde, M. G. & Zeytounian, R. K. *Interfacial phenomena and the Marangoni effect*. (Springer, 2002).
100 Hu, H. & Larson, R. G. Marangoni effect reverses coffee-ring depositions. *The Journal of Physical Chemistry B* **110**, 7090-7094 (2006).
101 Girard, F., Antoni, M. & Sefiane, K. On the effect of Marangoni flow on evaporation rates of heated water drops. *Langmuir* **24**, 9207-9210 (2008).
102 Proctor, M. & Weiss, N. Magnetoconvection. *Reports on Progress in Physics* **45**, 1317 (1982).
103 Vögler, A. Effects of non-grey radiative transfer on 3D simulations of solar magneto-convection. *Astronomy & Astrophysics* **421**, 755-762 (2004).
104 Shelyag, S., Schüssler, M., Solanki, S. K. & Vögler, A. Stokes diagnostics of simulated solar magneto-convection. *Astronomy & Astrophysics* **469**, 731-747 (2007).
105 Borrero, J., Jafarzadeh, S., Schüssler, M. & Solanki, S. Solar magnetoconvection and small-scale dynamo. *Space Science Reviews* **210**, 275-316 (2017).
106 Cossette, J.-F., Charbonneau, P., Smolarkiewicz, P. K. & Rast, M. P. Magnetically modulated heat transport in a global simulation of solar magneto-convection. *The Astrophysical Journal* **841**, 65 (2017).
107 Khomenko, E., Vitas, N., Collados, M. & de Vicente, A. Three-dimensional simulations of solar magneto-convection including effects of partial ionization. *Astronomy & Astrophysics* **618**, A87 (2018).
108 Gelfgat, A. Y. & Zikanov, O. Computational modeling of magnetoconvection: effects of discretization method, grid refinement and grid stretching. *Computers & Fluids* **175**, 66-82 (2018).
109 Alam, M. S., Mollah, M. S. H., Alim, M. A. & Uddin, M. N. in *AIP Conference Proceedings*. 050013 (AIP Publishing).
110 Zhang, J. & Zhang, M. On the infinite Prandtl number limit in two-dimensional magneto-convection. *Nonlinear Analysis: Real World Applications* **46**, 313-334 (2019).
111 Riley, N. Magnetohydrodynamic free convection. *Journal of Fluid Mechanics* **18**, 577-586 (1964).
112 Pradhan, K. & Guha, A. CFD solutions for magnetohydrodynamic natural convection over horizontal and vertical surfaces. *Journal of Molecular Liquids* **236**, 465-476 (2017).
113 Shankar, B. & Shivakumara, I. Magnetohydrodynamic stability of pressure-driven flow in an anisotropic porous channel: Accurate solution. *Applied Mathematics and Computation* **321**, 752-767 (2018).
114 Kuang, W. & Bloxham, J. Numerical modeling of magnetohydrodynamic convection in a rapidly rotating spherical shell: weak and strong field dynamo action. *Journal of Computational Physics* **153**, 51-81 (1999).

115 Mahmud, S. & Fraser, R. A. Magnetohydrodynamic free convection and entropy generation in a square porous cavity. *International Journal of Heat and Mass Transfer* **47**, 3245-3256 (2004).
116 Sheikholeslami, M. & Ganji, D. D. Ferrohydrodynamic and magnetohydrodynamic effects on ferrofluid flow and convective heat transfer. *Energy* **75**, 400-410 (2014).
117 Waqas, M. *et al*. Magnetohydrodynamic (MHD) mixed convection flow of micropolar liquid due to nonlinear stretched sheet with convective condition. *International Journal of Heat and Mass Transfer* **102**, 766-772 (2016).
118 Sheikholeslami, M. & Shehzad, S. Magnetohydrodynamic nanofluid convection in a porous enclosure considering heat flux boundary condition. *International Journal of Heat and Mass Transfer* **106**, 1261-1269 (2017).
119 Taylor, P. Analytical methods in planetary boundary-layer modelling. *Boundary-Layer Meteorology* **8**, 125-125 (1975).
120 Etling, D. & Brown, R. Roll vortices in the planetary boundary layer: A review. *Boundary-Layer Meteorology* **65**, 215-248 (1993).
121 Kuo, H. Perturbations of plane Couette flow in stratified fluid and origin of cloud streets. *The Physics of Fluids* **6**, 195-211 (1963).
122 Müller, H., Lücke, M. & Kamps, M. Convective patterns in horizontal flow. *EPL (Europhysics Letters)* **10**, 451 (1989).
123 Müller, H., Lücke, M. & Kamps, M. Transversal convection patterns in horizontal shear flow. *Physical Review A* **45**, 3714 (1992).
124 Müller, H., Tveitereid, M. & Trainoff, S. Rayleigh-Bénard problem with imposed weak through-flow: two coupled Ginzburg-Landau equations. *Physical Review E* **48**, 263 (1993).
125 Tveitereid, M. & Müller, H. W. Pattern selection at the onset of Rayleigh-Bénard convection in a horizontal shear flow. *Physical Review E* **50**, 1219 (1994).
126 Mohamad, A. & Viskanta, R. Laminar flow and heat transfer in Rayleigh–Benard convection with shear. *Physics of Fluids A: Fluid Dynamics* **4**, 2131-2140 (1992).
127 Felici, N. Phénomenes hydro et aérodynamiques dans la conduction des diélectriques fluides. *Rev. Gén. Electr.* **78**, 717-734 (1969).
128 Felici, N. & Lacroix, J. Electroconvection in insulating liquids with special reference to uni-and bi-polar injection: a review of the research work at the CNRS Laboratory for Electrostatics, Grenoble 1969–1976. *Journal of Electrostatics* **5**, 135-144 (1978).
129 Schneider, J. & Watson, P. Electrohydrodynamic Stability of Space‐Charge‐Limited Currents in Dielectric Liquids. I. Theoretical Study. *The Physics of Fluids* **13**, 1948-1954 (1970).
130 Watson, P., Schneider, J. & Till, H. Electrohydrodynamic Stability of Space‐Charge‐Limited Currents in Dielectric Liquids. II. Experimental Study. *The Physics of Fluids* **13**, 1955-1961 (1970).
131 Atten, P. & Moreau, R. Stabilité électrohydrodynamique des liquides isolants soumis à une injection unipolaire. *J. Mécanique* **11**, 471-521 (1972).
132 Lacroix, J., Atten, P. & Hopfinger, E. Electro-convection in a dielectric liquid layer subjected to unipolar injection. *Journal of Fluid Mechanics* **69**, 539-563 (1975).
133 Atten, P. & Lacroix, J. Non-linear hydrodynamic stability of liquids subjected to unipolar injection. *Journal de Mécanique* **18**, 469-510 (1979).
134 Atten, P. Rôle de la diffusion dans le problème de la stabilité hydrodynamique d'un liquide dièlectrique soumis à une injection unipolaire forte. *CR Acad. Sci. Paris* **283**, 29-32 (1976).
135 Li, F., Wang, B.-F., Wan, Z.-H., Wu, J. & Zhang, M. Absolute and convective instabilities in electrohydrodynamic flow subjected to a Poiseuille flow: a linear analysis. *Journal of Fluid Mechanics* **862**, 816-844 (2019).
136 Nicolas, X., Mojtabi, A. & Platten, J. K. Two-dimensional numerical analysis of the Poiseuille–Bénard flow in a rectangular channel heated from below. *Physics of Fluids* **9**, 337-348 (1997).
137 Carriere, P. & Monkewitz, P. A. Convective versus absolute instability in mixed Rayleigh–Bénard–Poiseuille convection. *Journal of Fluid Mechanics* **384**, 243-262 (1999).
138 Kato, Y. & Fujimura, K. Prediction of pattern selection due to an interaction between longitudinal rolls and transverse modes in a flow through a rectangular channel heated from below. *Physical Review E* **62**, 601 (2000).
139 Zhang, H., Huang, X., Li, H. & Chua, L. Flow patterns and heat transfer enhancement in low-Reynolds–Rayleigh-number channel flow. *Applied thermal engineering* **22**, 1277-1288 (2002).
140 Chicón, R., Castellanos, A. & Martin, E. Numerical modelling of Coulomb-driven convection in insulating liquids. *Journal of Fluid Mechanics* **344**, 43-66 (1997).
141 Vazquez, P., Georghiou, G. & Castellanos, A. Characterization of injection instabilities in electrohydrodynamics by numerical modelling: comparison of particle in cell and flux corrected transport methods for electroconvection between two plates. *Journal of Physics D: Applied Physics* **39**, 2754 (2006).
142 Guan, Y. & Novosselov, I. Two Relaxation Time Lattice Boltzmann Method Coupled to Fast Fourier Transform Poisson Solver: Application to Electroconvective Flow. *arXiv preprint arXiv:1812.05711* (2018).
143 Guan, Y. & Novosselov, I. Numerical Analysis of Electroconvection Phenomena in Cross-flow. *arXiv preprint arXiv:1812.10899* (2018).
144 Lorenz, E. N. Deterministic nonperiodic flow. *Journal of the atmospheric sciences* **20**, 130-141 (1963).
145 Saltzman, B. Finite amplitude free convection as an initial value problem—I. *Journal of the Atmospheric Sciences* **19**, 329-341 (1962).
146 Bhattacharjee, J. K. *Convection and chaos in fluids*. (World Scientific, 1987).
147 Atten, P., McCluskey, F. & Perez, A. Electroconvection and its effect on heat transfer. *IEEE Transactions on Electrical Insulation* **23**, 659-667 (1988).
148 Traoré, P., Pérez, A., Koulova, D. & Romat, H. Numerical modelling of finite-amplitude electro-thermo-convection in a dielectric liquid layer subjected to both unipolar injection and temperature gradient. *Journal of Fluid Mechanics* **658**, 279-293 (2010).
149 Feng, Y. & Seyed-Yagoobi, J. Mechanism of annular two-phase flow heat transfer enhancement and pressure drop penalty in the presence of a radial electric field—turbulence analysis. *Journal of heat transfer* **125**, 478-486 (2003).
150 Grassi, W., Testi, D. & Saputelli, M. EHD enhanced heat transfer in a vertical annulus. *International communications in heat and mass transfer* **32**, 748-757 (2005).
151 Grassi, W. & Testi, D. Heat transfer enhancement by electric fields in several heat exchange regimes. *Annals of the New York Academy of Sciences* **1077**, 527-569 (2006).
152 Grassi, W. & Testi, D. Heat transfer augmentation by ion injection in an annular duct. *Journal of heat transfer* **128**, 283-289 (2006).
153 Wu, J., Traoré, P., Zhang, M., Pérez, A. T. & Vázquez, P. A. Charge injection enhanced natural convection heat transfer in horizontal concentric annuli filled with a dielectric liquid. *International Journal of Heat and Mass Transfer* **92**, 139-148 (2016).
154 Lee, Y.-K., Deval, J., Tabeling, P. & Ho, C.-M. in *Microreaction Technology* 185-191 (Springer, 2001).

155 Chang, C. & Yang, R.-J. Computational analysis of electrokinetically driven flow mixing in microchannels with patterned blocks. *Journal of Micromechanics and Microengineering* **14**, 550 (2004).
156 Chang, C.-C. & Yang, R.-J. Electrokinetic mixing in microfluidic systems. *Microfluidics and Nanofluidics* **3**, 501-525 (2007).
157 Cho, C.-C. Electrokinetically driven flow mixing utilizing chaotic electric fields. *Microfluidics and nanofluidics* **5**, 785-793 (2008).
158 Zambrini, R., San Miguel, M., Durniak, C. & Taki, M. Convection-induced nonlinear symmetry breaking in wave mixing. *Physical Review E* **72**, 025603 (2005).
159 Gleeson, J. Truly random number generator based on turbulent electroconvection. *Applied physics letters* **81**, 1949-1951 (2002).
160 Atten, P., Lacroix, J. & Malraison, B. Chaotic motion in a Coulomb force driven instability: large aspect ratio experiments. *Physics Letters A* **79**, 255-258 (1980).
161 Pérez, A. & Castellanos, A. Laminar chaotic transport of charge in finite-amplitude electroconvection. *Physical Review A* **44**, 6659 (1991).
162 Dennin, M., Ahlers, G. & Cannell, D. S. Spatiotemporal chaos in electroconvection. *Science* **272**, 388-390 (1996).
163 Dennin, M., Ahlers, G. & Cannell, D. S. Chaotic localized states near the onset of electroconvection. *Physical review letters* **77**, 2475 (1996).
164 Tsai, P., Daya, Z. A. & Morris, S. W. Aspect-ratio dependence of charge transport in turbulent electroconvection. *Physical review letters* **92**, 084503 (2004).
165 Tsai, P., Daya, Z. A. & Morris, S. W. Charge transport scaling in turbulent electroconvection. *Physical Review E* **72**, 046311 (2005).
166 Zhou, S.-Q. & Ahlers, G. Spatiotemporal chaos in electroconvection of a homeotropically aligned nematic liquid crystal. *Physical Review E* **74**, 046212 (2006).
167 Buka, Á., Éber, N., Pesch, W. & Kramer, L. Isotropic and anisotropic electroconvection. *Physics reports* **448**, 115-132 (2007).
168 Takeuchi, K. A. & Sano, M. Universal fluctuations of growing interfaces: evidence in turbulent liquid crystals. *Physical review letters* **104**, 230601 (2010).
169 Castellanos, A., Pérez, A. & Chicon, R. Chaotic electroconvection in a layer of dielectric liquid subjected to unipolar injection: Maximal Lyapunov exponents. *International Journal of Bifurcation and Chaos* **12**, 2523-2534 (2002).
170 Demekhin, E., Nikitin, N. & Shelistov, V. Direct numerical simulation of electrokinetic instability and transition to chaotic motion. *Physics of Fluids* **25**, 122001 (2013).
171 Demekhin, E., Nikitin, N. & Shelistov, V. Three-dimensional coherent structures of electrokinetic instability. *Physical Review E* **90**, 013031 (2014).
172 Shelistov, V., Nikitin, N., Kiriy, V. & Demekhin, E. in *Doklady Physics.* 166-169 (Pleiades Publishing).
173 Seimandi, P., Dufour, G. & Rogier, F. An asymptotic model for steady wire-to-wire corona discharges. *Mathematical and Computer Modelling* **50**, 574-583 (2009).
174 Guan, Y., Vaddi, R. S., Aliseda, A. & Novosselov, I. Experimental and Numerical Investigation of Electro-Hydrodynamic Flow in a Point-to-Ring Corona Discharge *Physical Review Fluids* **3**, 14 (2018).
175 Durbin, P. A. Asymptotic analysis of corona discharge from thin electrodes. (1986).
176 Chen, J. & Davidson, J. H. Model of the negative DC corona plasma: comparison to the positive DC corona plasma. *Plasma chemistry and plasma processing* **23**, 83-102 (2003).
177 Boyd, J. P. *Chebyshev and Fourier spectral methods*. (Courier Corporation, 2001).
178 Trefethen, L. N. *Approximation theory and approximation practice*. Vol. 128 (Siam, 2013).
179 Trefethen, L. N. *Spectral methods in MATLAB*. Vol. 10 (Siam, 2000).
180 Trefethen, L. N. & team, t. C. d. (2011).
181 Cheng, Y.-s., Yeh, H.-C. & Kanapilly, G. M. Collection efficiencies of a point-to-plane electrostatic precipitator. *The American Industrial Hygiene Association Journal* **42**, 605-610 (1981).
182 Stainback, P. & Nagabushana, K. Review of hot-wire anemometry techniques and the range of their applicability for various flows. *Electronic Journal of Fluids Engineering* **1**, 4 (1993).
183 Kim, C., Park, D., Noh, K. & Hwang, J. Velocity and energy conversion efficiency characteristics of ionic wind generator in a multistage configuration. *Journal of Electrostatics* **68**, 36-41 (2010).
184 Hector, L. & Schultz, H. The dielectric constant of air at radiofrequencies. *Physics* **7**, 133-136 (1936).
185 LeVeque, R. J. *Finite volume methods for hyperbolic problems*. Vol. 31 (Cambridge university press, 2002).
186 Cagnoni, D. *et al.* Multiphysics simulation of corona discharge induced ionic wind. *Journal of Applied Physics* **114**, 233301 (2013).
187 Versteeg, H. K. & Malalasekera, W. *An introduction to computational fluid dynamics: the finite volume method*. (Pearson Education, 2007).
188 Guan, Y., Vaddi, R. S., Aliseda, A. & Novosselov, I. Supplemental information for Experimental and Numerical Investigation of Electro-Hydrodynamic Flow in a Point-to-Ring Corona Discharge *Physical Review Fluids* (2017).
189 Landau, L. D., Lifshitz, E. M., Sykes, J. B. & Reid, W. H. *Fluid Mechanics*. (Pergamon press inc, 1959).
190 McNaughton, K. & Sinclair, C. Submerged jets in short cylindrical flow vessels. *Journal of Fluid Mechanics* **25**, 367-375 (1966).
191 Kundu, P. K., Cohen, I. M. & Dowling, D. *Fluid Mechanics 4th*. (ELSEVIER, Oxford, 2008).
192 Chang, J.-S., Kelly, A. J. & Crowley, J. M. *Handbook of electrostatic processes*. (CRC Press, 1995).
193 IEEE-DEIS-EHD-Technical-Committee. Recommended international standard for dimensionless parameters used in electrohydrodynamics. *IEEE Transactions on Dielectrics and Electrical Insulation* **10**, 3-6 (2003).
194 Cotton, J., Robinson, A., Shoukri, M. & Chang, J. A two-phase flow pattern map for annular channels under a DC applied voltage and the application to electrohydrodynamic convective boiling analysis. *International Journal of Heat and Mass Transfer* **48**, 5563-5579 (2005).
195 Chorin, A. J. The numerical solution of the Navier-Stokes equations for an incompressible fluid. *Bulletin of the American Mathematical Society* **73**, 928-931 (1967).
196 Chorin, A. J. Numerical solution of the Navier-Stokes equations. *Mathematics of computation* **22**, 745-762 (1968).
197 Chorin, A. J., Marsden, J. E. & Marsden, J. E. *A mathematical introduction to fluid mechanics*. Vol. 3 (Springer, 1990).
198 LeVeque, R. J. *Finite difference methods for ordinary and partial differential equations: steady-state and time-dependent problems*. Vol. 98 (Siam, 2007).
199 Hirsch, C. *Numerical computation of internal and external flows: The fundamentals of computational fluid dynamics*. (Butterworth-Heinemann, 2007).

200 Runge, C. Über die numerische Auflösung von Differentialgleichungen. *Mathematische Annalen* **46**, 167-178 (1895).
201 Kutta, W. Beitrag zur näherungweisen Integration totaler Differentialgleichungen. (1901).
202 HSL. A collection of Fortran codes for large-scale scientific computation. *See http://www. hsl. rl. ac. uk* (2007).
203 Harlow, F. H. & Welch, J. E. Numerical calculation of time‐dependent viscous incompressible flow of fluid with free surface. *The physics of fluids* **8**, 2182-2189 (1965).
204 Patankar, S. *Numerical heat transfer and fluid flow*. (CRC press, 1980).
205 Steinberg, S. *Fundamentals of grid generation*. (CRC press, 1993).
206 Thompson, J. F., Soni, B. K. & Weatherill, N. P. *Handbook of grid generation*. (CRC press, 1998).
207 Ginzburg, I., Verhaeghe, F. & d'Humieres, D. Two-relaxation-time lattice Boltzmann scheme: About parametrization, velocity, pressure and mixed boundary conditions. *Communications in computational physics* **3**, 427-478 (2008).
208 Ginzburg, I., Verhaeghe, F. & d'Humieres, D. Study of simple hydrodynamic solutions with the two-relaxation-times lattice Boltzmann scheme. *Communications in computational physics* **3**, 519-581 (2008).
209 d'Humières, D. Viscosity independent numerical errors for Lattice Boltzmann models: From recurrence equations to "magic" collision numbers. *Comput. Math. Appl.* **58**, 823 (2009).
210 Ginzburg, I., d'Humières, D. & Kuzmin, A. Optimal stability of advection-diffusion lattice Boltzmann models with two relaxation times for positive/negative equilibrium. *Journal of Statistical Physics* **139**, 1090-1143 (2010).
211 Kuzmin, A., Ginzburg, I. & Mohamad, A. The role of the kinetic parameter in the stability of two-relaxation-time advection–diffusion lattice Boltzmann schemes. *Computers & Mathematics with Applications* **61**, 3417-3442 (2011).
212 Ginzburg, I. Truncation errors, exact and heuristic stability analysis of two-relaxation-times lattice Boltzmann schemes for anisotropic advection-diffusion equation. *Communications in Computational Physics* **11**, 1439-1502 (2012).
213 Khirevich, S., Ginzburg, I. & Tallarek, U. Coarse-and fine-grid numerical behavior of MRT/TRT lattice-Boltzmann schemes in regular and random sphere packings. *Journal of Computational Physics* **281**, 708-742 (2015).
214 Ginzburg, I. & Roux, L. Truncation effect on Taylor–Aris dispersion in lattice Boltzmann schemes: Accuracy towards stability. *Journal of Computational Physics* **299**, 974-1003 (2015).
215 Ginzburg, I., Roux, L. & Silva, G. Local boundary reflections in lattice Boltzmann schemes: Spurious boundary layers and their impact on the velocity, diffusion and dispersion. *Comptes Rendus Mécanique* **343**, 518-532 (2015).
216 Ku, H. C., Hirsh, R. S. & Taylor, T. D. A pseudospectral method for solution of the three-dimensional incompressible Navier-Stokes equations. *Journal of Computational Physics* **70**, 439-462 (1987).
217 Fornberg, B. *A practical guide to pseudospectral methods*. Vol. 1 (Cambridge university press, 1998).
218 Kutz, J. N., Brunton, S. L., Brunton, B. W. & Proctor, J. L. *Dynamic mode decomposition: data-driven modeling of complex systems*. Vol. 149 (SIAM, 2016).
219 Schmid, P. J. Dynamic mode decomposition of numerical and experimental data. *Journal of fluid mechanics* **656**, 5-28 (2010).
220 Schmid, P. J., Li, L., Juniper, M. P. & Pust, O. Applications of the dynamic mode decomposition. *Theoretical and Computational Fluid Dynamics* **25**, 249-259 (2011).
221 Schmid, P. J., Meyer, K. E. & Pust, O. in *8th International Symposium on Particle Image Velocimetry*. 25-28.
222 Bai, Z., Kaiser, E., Proctor, J. L., Kutz, J. N. & Brunton, S. L. Dynamic mode decomposition for compressive system identification. *AIAA Journal*, 1-14 (2019).
223 Jovanović, M. R., Schmid, P. J. & Nichols, J. W. Sparsity-promoting dynamic mode decomposition. *Physics of Fluids* **26**, 024103 (2014).
224 Proctor, J. L., Brunton, S. L. & Kutz, J. N. Dynamic mode decomposition with control. *SIAM Journal on Applied Dynamical Systems* **15**, 142-161 (2016).
225 Krüger, T. *et al. The Lattice Boltzmann Method*. (Springer, 2017).
226 Hayashi, K., Rojas, R., Seta, T. & Tomiyama, A. Immersed boundary-lattice Boltzmann method using two relaxation times. *The Journal of Computational Multiphase Flows* **4**, 193-209 (2012).
227 Seta, T., Rojas, R., Hayashi, K. & Tomiyama, A. Implicit-correction-based immersed boundary–lattice Boltzmann method with two relaxation times. *Physical Review E* **89**, 023307 (2014).
228 Ginzbourg, I. & Adler, P. Boundary flow condition analysis for the three-dimensional lattice Boltzmann model. *Journal de Physique II* **4**, 191-214 (1994).
229 Domaradzki, J. A. & Metcalfe, R. W. Direct numerical simulations of the effects of shear on turbulent Rayleigh-Bénard convection. *Journal of Fluid Mechanics* **193**, 499-531 (1988).
230 Vaddi, R. S., Guan, Y. & Novosselov, I. Particle Dynamics in Corona Induced Electro-hydrodynamic Flow. *arXiv preprint arXiv:1902.02986* (2019).
231 Fuchs, N. A. On the stationary charge distribution on aerosol particles in a bipolar ionic atmosphere. *Geofisica pura e applicata* **56**, 185-193, doi:10.1007/bf01993343 (1963).
232 Marlow, W. H. & Brock, J. R. Unipolar charging of small aerosol particles. *Journal of Colloid And Interface Science* **50**, 32-38, doi:10.1016/0021-9797(75)90250-7 (1975).
233 Lee, M. H. *et al.* Enhanced collection efficiency of nanoparticles by electrostatic precipitator with needle-cylinder configuration. *Journal of Nanoscience and Nanotechnology* **16**, 6884-6888, doi:10.1166/jnn.2016.11322 (2016).
234 Zhuang, Y., Jin Kim, Y., Gyu Lee, T. & Biswas, P. Experimental and theoretical studies of ultra-fine particle behavior in electrostatic precipitators. *Journal of Electrostatics* **48**, 245-260, doi:10.1016/S0304-3886(99)00072-8 (2000).
235 Ravi, L. & Girshick, S. L. Coagulation of nanoparticles in a plasma. *Physical review. E, Statistical, nonlinear, and soft matter physics* **79**, 026408, doi:10.1103/PhysRevE.79.026408 (2009).
236 Pelletier, J. Dusty plasmas: physics, chemistry and technological impacts in plasma processing. *Plasma Physics and Controlled Fusion* **42**, 227-227, doi:10.1088/0741-3335/42/2/701 (2000).
237 Huang, S.-H. & Chen, C.-C. Ultrafine aerosol penetration through electrostatic precipitators. *Environmental Science & Technology* **36**, 4625-4632, doi:10.1021/es011157+ (2002).
238 Ju, Y. & Sun, W. Plasma assisted combustion: Progress, challenges, and opportunities. *Combustion and Flame* **162**, 529-532, doi:10.1016/j.combustflame.2015.01.017 (2015).
239 Starikovskii, A. Y. *et al.* Vol. 78 1265-1298 (2006).
240 Go, D. B., Garimella, S. V. & Fisher, T. S. 45-53 (USA, 2006).

241 Go, D. B., Garimella, S. V., Fisher, T. S. & Mongia, R. K. Ionic winds for locally enhanced cooling. *Journal of Applied Physics* **102**, doi:10.1063/1.2776164 (2007).
242 Jewell-Larsen, N. E. *et al.* CFD analysis of electrostatic fluid accelerators for forced convection cooling. *Dielectrics and Electrical Insulation, IEEE Transactions on* **15**, doi:10.1109/TDEI.2008.4712680 (2008).
243 Touchard, G. Plasma actuators for aeronautics applications-State of art review. *IJ PEST* **2**, 1-25 (2008).
244 Drew, D. S. & Pister, K. S. J. 1-5 (2017).
245 Drew, D., Contreras, D. S. & Pister, K. S. J. 346-349 (2017).
246 Xu, H. *et al.* Flight of an aeroplane with solid-state propulsion. *Nature* **563**, 532, doi:10.1038/s41586-018-0707-9 (2018).
247 Townsend, J. S. The potentials requires to maintain currents between coaxial cylinders. *The London, Edinburgh and Dublin philosophical magazine and journal of science* **28**, 8 (1914).
248 Sigmond, R. S. Simple approximate treatment of unipolar space‐charge‐dominated coronas: The Warburg law and the saturation current. *Journal of Applied Physics* **53**, 891-898, doi:10.1063/1.330557 (1982).
249 An interactive computer model for calculating V-I curves in ESPs (EPA, Particulate Technology Branch, Research Triangle Park, North Carolina, 1986).
250 Cristina, S., Dinelli, G. & Feliziani, M. Numerical computation of corona space charge and V-I characteristic in DC electrostatic precipitators. *Industry Applications, IEEE Transactions on* **27**, 147-153, doi:10.1109/28.67546 (1991).
251 Yamamoto, T., Okuda, M. & Okubo, M. Vol. 2 1397-1403 (2002).
252 Peek, F. W. in *the 28th Annual Convention of the American Institute of Electrical Engineers* (Chicago, 1911).
253 Yamada, K. An empirical formula for negative corona discharge current in point-grid electrode geometry. *Journal of Applied Physics* **96** (`2004).
254 Giubbilini, P. The current-voltage characteristics of point-to-ring corona. *Journal of Applied Physics* **64** (1988).
255 Jewell-Larsen, N. E., Zhang, P. Q., Hsu, C. P., Krichtafovitch, I. A. & Mamishev, A. V. Vol. 3 2038-2047 (2006).
256 Yu Zhang, L. L., Yang Chen, Jiting Ouyang. Characteristics of ionic wind in needle-to-ring corona discharge. *Journal of Electrostatics* **74**, 6 (2015).
257 Landau, L. D. *Fluid mechanics*. (London : Pergamon Press ; Reading, Mass. : Addison-Wesley Pub. Co., 1959).
258 Glauert, M. The wall jet. *Journal of Fluid Mechanics* **1**, 625-643 (1956).
259 George, W. K. *et al.* A similarity theory for the turbulent plane wall jet without external stream. *Journal of Fluid Mechanics* **425**, 367-411 (2000).
260 Fillingham, P. & Novosselov, I. Similarity of the Wall Jet Resulting from Planar Underexpanded Impinging Jets. *arXiv preprint arXiv:1812.11220* (2018).
261 Guan, Y. & Novosselov, I. EVALUATION OF LEAN BLOW-OUT MECHANISM IN TOROIDAL JET STIRRED REACTOR. *Journal of Engineering for Gas Turbines and Power*.
262 Herbinet, O. & Dayma, G. in *Cleaner combustion* 183-210 (Springer, 2013).
263 Sturgess, G. J., Sloan, D. G., Lesmerises, A. L., Heneghan, S. P. & Ballal, D. R. Design and development of a research combustor for lean blowout studies. *Journal of Engineering for Gas Turbines and Power* **114**, 13-19 (1992).
264 Malte, P. C. & Pratt, D. The role of energy-releasing kinetics in NOx formation: fuel-lean, jet-stirred CO-air combustion. *Combustion Science and Technology* **9**, 221-231 (1974).
265 Rutar, T. & Malte, P. C. NOx Formation in High-Pressure Jet-Stirred Reactors with Significance to Lean-Premixed Combustion Turbines. *ASME Journal of Engineering for Gas Turbines and Power* **124**, 776-783 (2002).
266 Longwell, J. P., Frost, E. E. & Weiss, M. A. Flame stability in bluff body recirculation zones. *Industrial and Engineering Chemistry* **45**, 1629-1633 (1953).
267 Plee, S. L. & Mellor, A. M. Characteristic time correlation for lean blowoff of bluff-body-stabilized flames. *Combustion and Flame* **35**, 61-80 (1979).
268 Zukoski, E. FE Marble Proceedings of the Gas Dynamics Symposium on Aerothermochemistry. *Northwestern University, Evanston, Illinois*, 205 (1956).
269 Glassman, I. & Yetter, R. A. *Combustion 4th edition*. (Academic Press, 2008).
270 Turns, S. R. *An introduction to combustion: concepts and applications, 3rd edition*. (McGraw Hill Education, 2012).
271 DePappe, P., Novossolov, I. V. & Malte, P. C. Chemical Reactor Network for Real-Time Monitoring and Analysis of Combustor Performance. *Combustion Science and Technology* (2017).
272 Schefer, R. W. Hydrogen enrichment for improved lean flame stability. *International Journal of Hydrogen Energy* **28**, 1131-1141 (2003).
273 Burbano, H. J., Pareja, J. & Amell, A. A. Laminar burning velocities and flame stability analysis of H2/CO/air mixtures with dilution of N2 and CO2. *International Journal of Hydrogen Energy* **36**, 3232-3242 (2011).
274 Muruganandam, T. *et al.* Active control of lean blowout for turbine engine combustors. *Journal of Propulsion and Power* **21**, 807-814 (2005).
275 Prathap, C., Ray, A. & Ravi, M. R. Effects of dilution with carbon dioxide on the laminar burning velocity and flame stability of H2-CO mixtures at atmospheric condition. *Combustion and Flame* **159**, 482-492 (2012).
276 Amato, A. *et al.* Methane Oxycombustion for low CO2 cycles: blowoff measurements and analysis. *Journal of Engineering for Gas Turbines and Power* **133**, 1-9 (2011).
277 Fackler, K. B. *et al.* NOx behavior for lean-premixed combustion of alternative gaseous fuels. *Journal of Engineering for Gas Turbines and Power* **138**, 1-11 (2016).
278 Stohr, M., Boxx, I., Carter, C. & Meier, W. Dynamics of lean blowout of a swirl-stabilized flame in a gas turbine model combustor. *Proceedings of the Combustion Institute* **33**, 2953-2960 (2011).
279 Hu, B., Huang, Y. & Xu, J. A hybrid semi-empirical model for lean blow-out limit predictions of aero-engine combustors. *Journal of Engineering for Gas Turbines and Power* **137**, 1-10 (2014).
280 Radhakrishnan, K., Heywood, J. B. & Tabaczynski, R. J. Premixed turbulent flame blowoff velocity correlation based on coherent structures in turbulent flows. *Combustion and Flame* **42**, 19-33 (1981).
281 Kim, W.-W. *et al.* Towards modeling lean blow out in gas turbine flameholder applications. *Journal of engineering for Gas Turbines and Power* **128**, 40-48 (2004).

282 Novosselov, I. V., Malte, P. C., Yuan, S., Srinivasan, R. & Lee, J. C. Y. in *ASME Turbo Expo 2006: Power for Land, Sea, and Air* 221-235 (Barcelona, Spain, 2006).
283 Nanduri, J. R., Parsons, D. R., Yilmaz, S. L., Celik, I. B. & Strakey, P. A. Assessment of RANS-based turbulent combustion models for prediction of emissions from lean premixed combustion of methane. *Combustion Science and Technology* **182**, 794-821 (2010).
284 Walters, D. K., Bhushan, S., Alam, M. F. & Thompson, D. S. Investigation of a dynamic hybrid RANS/LES modelling methodology for finite-volume CFD simulations. *Flow Turbulence and Combustion* **91**, 643-667 (2013).
285 Fureby, C. A comparative study of flamelet and finite rate chemistry LES for a swirl stabilized flame. *Journal of Engineering for Gas Turbines and Power* **134**, 1-13 (2012).
286 Hanjalic, K. & Launder, B. E. A Reynolds stress model of turbulence and its application to thin shear flows. *Journal of Fluid Mechanics* **52**, 609-638 (1972).
287 Launder, B. E., Reece, G. J. & Rodi, W. Progress in the development of a Reynolds-stress turbulence closure. *Journal of Fluid Mechanics* **68**, 537-566 (1975).
288 Durbin, P. A. A Reynolds stress model for near-wall turbulence. *Journal of Fluid Mechanics* **249**, 465-498 (1993).
289 Wallin, S. & Johansson, A. V. An explicit algebraic Reynolds stress model for incompressible and compressible turbulent flows. *Journal of Fluid Mechanics* **403**, 89-133 (2000).
290 Yang, S. L., Siow, Y. K., Peschke, B. D. & Tacina, R. R. Numerical study of nonreacting gas turbine combustor swirl flow using Reynolds Stress Model. *Journal of Engineering for Gas Turbines and Power* **125**, 804-811 (2003).
291 Yang, S. L. *et al.* Numerical study of lean-direct injection combustor with discrete-jet swirlers using Reynolds Stress Model. *Journal of Engineering for Gas Turbines and Power* **125**, 1059-1065 (2003).
292 Magnussen, B. F. in *19th American Institute of Aeronautics and Astronautics Aerospace Science Meeting* (St. Louis, Missouri, USA, 1981).
293 Ertesvag, I. S. & Magnussen, B. F. The eddy dissipation turbulence energy cascade model. *Combustion science and Technology* **159**, 213-235 (2000).
294 Magnussen, B. F. in *ECCOMAS Thematic Conference on Computational Combustion* (Lisbon, 2005).
295 Karalus, M. F., Fackler, K. B., Novosselov, I. V., Kramlich, J. C. & Malte, P. C. in *ASME Turbo Expo 2013: Turbine Technical Conference and Exposition* 1-10 (ASME, San Antonio, Texas, USA, 2013).
296 Ayed, A. H. *et al.* Experimental and numerical investigations of the dry-low-NOx hydrogen micromix combustion chamber of an industrial gas turbine. *Propulsion and Power Research* **4**, 123-131 (2015).
297 Karalus, M. F., Fackler, K. B., Novosselov, I. V., Kramlich, J. C. & Malte, P. C. in *Turbine Technical Conference and Exposition* 21-30 (ASME Turbo Expo, Copenhagen, Denmark, 2012).
298 Nenniger, J. E., Kridiotis, A., Chomiak, J., Longwell, J. P. & Sarofim, A. F. Characterization of a toroidal well stirred reactor. *20th Symposium (International) on Combustion/ The Combustion Institute*, 473-479 (1984).
299 Clarke, A. E., Harrison, A. J. & Odgers, J. Combustion stability in a spherical combustor. *Symposium (International) on Combustion* **7**, 664-673 (1958).
300 Clarke, A. E., Odgers, J. & Ryan, P. Further studies of combustion phenomena in a spherical combustor. *Symposium (International) on Combustion* **8**, 982-994 (1961).
301 Clarke, A. E., Odgers, J., Stringer, F. W. & Harrison, A. J. Combustion processes in a spherical combustor. *Symposium (International) on Combustion* **10**, 1151-1166 (1965).
302 Odgers, J. & Carrier, C. Modelling of gas turbine combustors; considerations of combustion efficiency and stability. *Journal of Engineering for Power* **95**, 105-113 (1973).
303 Longwell, J. P. & Bar-Ziv, E. Modeling of inhomogeneities in the toroidal jet-stirred reactor. *Combustion and Flame* **78**, 99-119 (1989).
304 Barat, R. B. Jet-stirred combustor behavior near blowout: observations and implications. *Combustion Science and Technology* **84**, 187-197 (1992).
305 Vijlee, S. Z., Kramlich, J. C., Mescher, A. M., Stouffer, S. D. & O'Neil-Abels, A. R. in *ASME Turbo Expo 2013: Turbine Technical Conference and Exposition.* 1-8 (American Society of Mechanical Engineers).
306 Vijlee, S. Z., Novosselov, I. V. & Kramlich, J. C. in *ASME Turbo Expo 2015: Turbine Technical Conference and Exposition.* 1-12 (American Society of Mechanical Engineers).
307 Briones, A., Sekar, B., Zelina, J., Pawlik, R. & Stouffer, S. in *44th AIAA/ASME/SAE/ASEE Joint Propulsion Conference & Exhibit* 1-19 (Hartford, CT, 2008).
308 Baratta, M., Catania, A. E. & d'Ambrosio, S. Nonlinear versus linear stress-strain relations in engine turbulence modeling under swirl and squish flow conditions. *Journal of Engineering for Gas Turbines and Power* **130**, 1-11 (2008).
309 Kalitzin, G., Medic, G., Laccarino, G. & Durbin, P. Near-wall behavior of RANS turbulence models and implications for wall functions. *Journal of Computational Physics* **204**, 265-291 (2005).
310 Auerkari, P. *Mechanical and physical properties of engineering alumina ceramics*. (Technical Research Centre of Finland Finland, 1996).
311 Mills, A. F. *Basic heat and mass transfer*. (Pearson College Div, 1999).
312 Vijlee, S. Z. *Effects of Fuel Composition on Combustion Stability and NOX Emissions for Traditional and Alternative Jet Fuels* Doctor of Philosophy thesis, University of Washington, (2014).
313 ANSYS FLUENT (2017).
314 Novosselov, I. V. & Malte, P. C. Development and application of an eight-step global mechanism for CFD and CRN simulations of lean-premixed combustors. *Journal of Engineering for Gas Turbines and Power* **130**, 1-9 (2008).
315 Pope, S. B. (IOP Publishing, 2001).
316 Cherdron, W., Durst, F. & Whitelaw, J. H. Asymmetric flows and instabilities in symmetric ducts with sudden expansions. *Journal of Fluid Mechanics* **84**, 13-29 (1978).
317 Lai, C. Y., Rajagopal, K. R. & Szeri, A. Z. Asymmetric flow between parallel rotating disks. *Journal of Fluid Mechanics* **146**, 203-225 (1984).
318 Zaman, K. B. M. Q. Axis switching and spreading of an asymmetric jet: the role of coherent structure dynamics. *Journal of Fluid Mechanics* **316**, 1-27 (1996).

319 DePape, P. & Novosselov, I. Model-Based Approach for Combustion Monitoring Using Real-Time Chemical Reactor Network. *Journal of Combustion* **2018** (2018).
320 Vagelopoulos, C. M. & Egolfopoulos, F. N. Laminar flame speeds and extinction strain rates of mixtures of carbon monoxide with hydrogen, methane, and air. *20th Symposium (International) on Combustion/ The Combustion Institute* **25**, 1317-1323 (1994).
321 Dirrenberger, P. *et al.* Measurements of laminar flame velocity for components of natural gas. *Energy & Fuels* **29**, 3875-3884 (2011).
322 Koutmos, P. A Damkohler number description of local extinction in turbulent methane jet diffusion flames. *Fuel* **78**, 623-626 (1999).
323 Oberlack, M., Arlitt, R. & Peters, N. On stochastic Damkohler number variations in a homogeneous flow reactor. *Combustion Theory and Modelling* **4**, 495-510 (2000).